AD-A239 460

REPORT DOCUMENTATION PAGE

Public reporting burden for this collection of information is estimated to average 1 hour per response, including the time for reviewing instructions, searching existing data sources, gathering and maintaining the data needed, and completing and reviewing the collection of information. Send comments regarding this burden estimate or any other aspect of this collection of information, including suggestions for reducing this burden, to Washington Headquarters Services, Directorate for Information Operations and Reports, 1215 Jefferson Davis Highway, Suite 1204, Arlington, VA 22202-4302, and to the Office of Management and Budget, Paperwork Reduction Project (0704-0188), Washington, DC 20503

1. AGENCY USE ONLY (Leave blank)	2. REPORT DATE	3. REPORT TYPE AND DATES COVERED
		THESIS/~~DISSERTATION~~

4. TITLE AND SUBTITLE
Application of Multivariable Control System Design Methodologies to Robust Beam Control of a Space-Based Laser

5. FUNDING NUMBERS

6. AUTHOR(S)
Kelly D. Hammett, First Lieutenant

7. PERFORMING ORGANIZATION NAME(S) AND ADDRESS(ES)

AFIT Student Attending: Massachusetts Institute of Technology

8. PERFORMING ORGANIZATION REPORT NUMBER

AFIT/CI/CIA- 91-058

9. SPONSORING/MONITORING AGENCY NAME(S) AND ADDRESS(ES)

AFIT/CI
Wright-Patterson AFB OH 45433-6583

10. SPONSORING/MONITORING AGENCY REPORT NUMBER

11. SUPPLEMENTARY NOTES

12a. DISTRIBUTION/AVAILABILITY STATEMENT
Approved for Public Release IAW 190-1
Distributed Unlimited
ERNEST A. HAYGOOD, 1st Lt, USAF
Executive Officer

12b. DISTRIBUTION CODE

13. ABSTRACT (Maximum 200 words)

This document has been approved
for public release and sale; its
distribution is unlimited.

DTIC
ELECTE
AUG 0 3 1991
S D

91-07269

14. SUBJECT TERMS			15. NUMBER OF PAGES
			177
			16. PRICE CODE

17. SECURITY CLASSIFICATION OF REPORT	18. SECURITY CLASSIFICATION OF THIS PAGE	19. SECURITY CLASSIFICATION OF ABSTRACT	20. LIMITATION OF ABSTRACT

91 8 07 095

CSDL-T-1078

APPLICATION OF MULTIVARIABLE CONTROL SYSTEM DESIGN METHODOLOGIES TO ROBUST BEAM CONTROL OF A SPACE-BASED LASER

by
Kelly Douglas Hammett

June 1991

LABORATORY

Application of Multivariable Control System Design Methodologies to Robust Beam Control of a Space-Based Laser

by

Kelly Douglas Hammett

B.S., Aerospace Engineering
University of Oklahoma
(1988)

SUBMITTED TO THE DEPARTMENT OF AERONAUTICS AND
ASTRONAUTICS IN PARTIAL FULFILLMENT OF THE
REQUIREMENTS FOR THE DEGREE OF

MASTER OF SCIENCE
at the
MASSACHUSETTS INSTITUTE OF TECHNOLOGY
June 1991
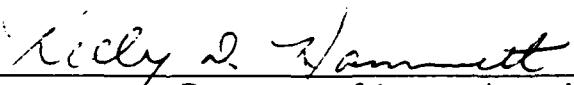
Signature of Author_____
Department of Aeronautics and Astronautics
May 10, 1991
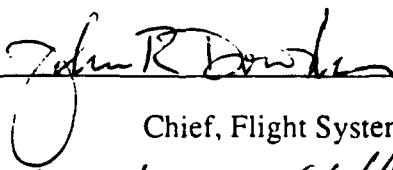
Certified by_____
Dr. John R. Dowdle
Chief, Flight Systems Section, C.S. Draper Lab
Technical Supervisor
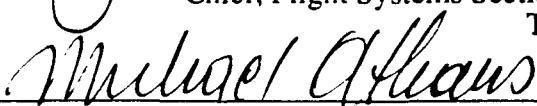
Certified by_____
Michael Athans
Professor of Electrical Engineering
Thesis Supervisor
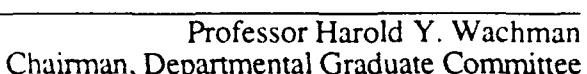
Accepted by_____
Professor Harold Y. Wachman
Chairman, Departmental Graduate Committee

1

Application of Multivariable Control System Design Methodologies to Robust Beam Control of a Space-Based Laser

by

Kelly Douglas Hammett

Submitted to the Department of Aeronautics and Astronautics
on May 10, 1991, in partial fulfillment of the requirements
for the degree of Master of Science in Aeronautics and Astronautics

Abstract

The complexity of large-scale dynamic systems provides a challenging proving ground for modern control system analysis and design techniques. High plant dimensionality inherent in large-scale systems can lead to breakdowns in numerics of state-space algorithms or intolerably long computational times, necessitating use of model reduction techniques. Reducing plant order consequently introduces unmodeled dynamics into the system, which must then be accounted for via stability and performance robustness considerations. A design framework is adopted herein which allows stability robustness to be guaranteed via unstructured uncertainty representation and the Small Gain Theorem, and performance robustness to be independently verified. The applicability of modern multivariable controller design techniques to large-scale systems is demonstrated by synthesis of robustly stable H_2 optimal, H_∞ optimal, and H_2/H_∞ loop-shaped compensators for a space-based laser forebody using reduced order models. Performance goals are expressed in terms of both allowable 2-norms and root-mean-square values of line-of-sight and segment phasing errors, and an evolutionary process leads to a final controller design. First, ideally performing but non-robust unconstrained bandwidth H_2 and H_∞ designs are presented which illustrate the danger of ignoring unmodeled high-frequency dynamics. Then robustly stable but poorly performing reduced bandwidth H_2 and H_∞ designs are derived, achieved via constant penalizing of the system control at all frequencies. Next, frequency-dependent penalty of the errors/controls leads to H_2/H_∞ loop-shaping designs, which yield superior closed-loop performance and stability robustness. Issues relating to digital implementation of continuous-time controllers are addressed, a study of reduced-order compensators is performed, and the final design is validated via time domain simulation and steady-state covariance analysis. Finally, performance robustness issues and effects of parametric uncertainty on open-loop system model natural frequencies are addressed.

Thesis Supervisor: Professor Michael Athans
Title: Professor of Electrical Engineering, M.I.T.

Technical Supervisor: Dr. John R. Dowdle
Title: Chief, Flight Systems Section
Charles Stark Draper Laboratory, Inc.

Acknowledgements

I would like to express my appreciation to the Charles Stark Draper Laboratory and the United States Air Force for providing me the opportunity to pursue graduate level education at the Massachusetts Institute of Technology. Over the course of my two years at MIT, both the financial and personal support from these two organizations have proven to be tremendous. Several individuals played key roles in helping me to even get here, most notably Dr. Dave Burke from CSDL and Major David Alkove, USAF.

I would also like to acknowledge a strong sense of gratitude and respect for Dr. John R. Dowdle for both the depth and breadth of his technical expertise, and for the extreme and patient willingness with which he shared that expertise. His personal concern and sense of humor made my stint as a graduate student at MIT and CSDL enjoyable as well as intellectually rewarding. I simply could not have asked for a better supervisor.

My MIT thesis advisor, Professor Michael Athans, constantly pushed me toward a better physical understanding of the issues involved in this thesis and in multivariable control in general, and for this furthering of my education I owe a debt of appreciation.

My thanks also to Dr. Brent Appleby, Dr. Karl Flueckiger, Mr. Tim Henderson, Mr. Robert Regan, and Mr. Duncan McCallum all of CSDL for assisting me through a number of problematic technical challenges encountered along the way.

I would like to thank my parents for providing a fundamental base upon which my education could be built, and for their assistance in helping me complete my undergraduate education which enabled me to reach the point where I am now.

Finally, and most importantly, I would like to thank my wife, Kellie, for leaving behind all that she knew to join me on this voyage of higher learning and cultural adjustment. Her patience while I devoted the bulk of my time to my studies has been

greatly appreciated, and her sacrifices have provided constant incentive to make the most out of my educational opportunities at MIT. I therefore dedicate this thesis to her.

Contents

List of Figures

9

11

List of Tables

13

Notation and Abbreviations

r	complex-valued vector
C^n	vector space of complex-valued vectors with n elements
$r(t)$	real-valued vector signal
R	complex-valued matrix
r^T, R^T	transpose of the vector r, matrix R
r^H, R^H	Hermitian (complex-conjugate transpose) of the vector r, matrix R
$tr(R)$	trace of the matrix R
R^{-1}	inverse of the matrix R
$R > 0$	the matrix R is positive definite
$R \geq 0$	the matrix R is positive semi-definite
$\lambda_i(R)$	i^{th} eigenvalue of the matrix R
ω_n	undamped natural frequency associated with the ith eigenvalue
ζ	damping ratio of the ith eigenvalue
$\sigma_i(R)$	i^{th} singular value of the matrix R
$\sigma_1(R)$	maximum singular value of the matrix R
$G(s)$	open-loop transfer function
$T(s)$	closed-loop transfer function
$K(s)$	compensator transfer function
$\Delta(s)$	uncertainty block transfer function
$\Delta_M(s)$	multiplicative error uncertainty block transfer function

$S_o(s)$	output sensitivity transfer function
$C_o(s)$	output complementary sensitivity transfer function
x	vector of system state variables
z	input vector to the uncertainty block
w	output vector to the uncertainty block
d	input vector containing all exogenous disturbances signals (disturbances, sensor noises, and reference inputs)
e	performance or error vector (to be kept small)
u	control input vector
y	measured output.vector
d_T	disturbance torque vector
$\tilde{u}$	vector of combined disturbance torques and control inputs
θ	additive sensor (measurement) noise vector
σ_r, σ_r^2	root-mean-square value, variance of stochastic vector signal r
$\|r\|_p$	p^{th}-norm of the vector r
$\|G(s)\|_p$	p^{th}-norm of the transfer function G(s)
H_2	the subspace of complex-valued functions analytic and with bounded 2-norms in the complex right-half plane
H_∞	the subspace of complex-valued functions analytic and with bounded infinity-norms in the complex right-half plane
γ	upper bound on gamma-iteration infinity-norm achievable performance
ρ	scalar control weight
Σ_r	steady-state covariance matrix of stochastic vector signal r
Φ_r	power spectral density of stochastic vector signal r
SBL	space-based laser
HEL	high-energy laser

BEA	beam expander assembly
LQG	Linear Quadratic Gaussian
DPM	Design Plant Model
LOS	line-of-sight
RTZ	radial-tangential-longitudinal
RMS	root-mean-square
GEP	generalized eigenvalue problem
LTI	linear time-invariant
SISO	single-input, single-output
MIMO	multi-input, multi-output
BIBO	bounded-input, bounded-output
SVD	singular value decomposition
FOM	full-order model
ROM	reduced-order model
B&T	balance and truncate (model reduction algorithm)
MT	modal truncation (model reduction algorithm)
HSV	Hankel singular value
SGT	Small Gain Theorem
dB	decibel
C-T	continuous-time
D-T	discrete-time

CHAPTER 1

Introduction

1.1 Background

Following President Ronald Reagan's launching of the Strategic Defense Initiative (SDI) in 1983, great interest was generated in the United States' research and development community toward viable system concepts for protecting this country from the threat of weapons delivered through outer space. The prime motivation for developing such a defense system lay in the large stockpile of nuclear warheads amassed by the Soviet Union in the 1970s, and the arsenal of intercontinental ballistic missiles (ICBMs) maintained to deliver them. The purpose of SDI was to research and develop systems that could somehow render ICBMs harmless before they struck their ground targets, preferably while the warheads were still outside the earth's atmosphere. During the course of the mid and late 1980s, several widely different concepts to meet this purpose were considered, and one that generated great interest and enthusiasm was that of the space-based laser (SBL). At the time of SDI's inception however, a number of critical technologies required for implementation of the space-based laser concept were lacking. These undeveloped technologies included mirror manufacturing techniques, power generation methods, and signal processing/control system algorithms and hardware, to name but a few. The widespread and intense research effort of the mid and late 1980s led to progress in many of these areas, but realizable and effective control system design for space-based lasers remains a topic of current research. It is this topic that is pursued in this thesis.

1.2 SBL System Concept

Before proceeding further, a brief and somewhat general description of an SBL physical system concept and relevant terminology is presented to facilitate discussion. For purposes of this study, the space-based laser can be visualized as consisting of two parts, the forebody and the aftbody. The aftbody consists of the satellite platform, and contains all necessary equipment for orbital station-keeping and satellite attitude control. In addition, the SBL aftbody contains the mechanisms required for generation of the high-energy laser (HEL) beam, and adequate optical components for transfer of the beam to the SBL forebody. The forebody of the SBL houses the beam expander assembly (BEA), which consists of a large, deformable primary mirror attached to a rigid bulkhead support, a much smaller and stiffer secondary mirror, a metering truss to maintain relative positions of the two mirrors, and all necessary sensors and actuators for accomplishing required control functions. The BEA points, magnifies, and focuses the HEL beam generated in the aftbody as necessary to meet various mission requirements. Figure 1.1 below shows the SBL forebody. Further details concerning the SBL are provided along with the description of the system model in Chapter 2.
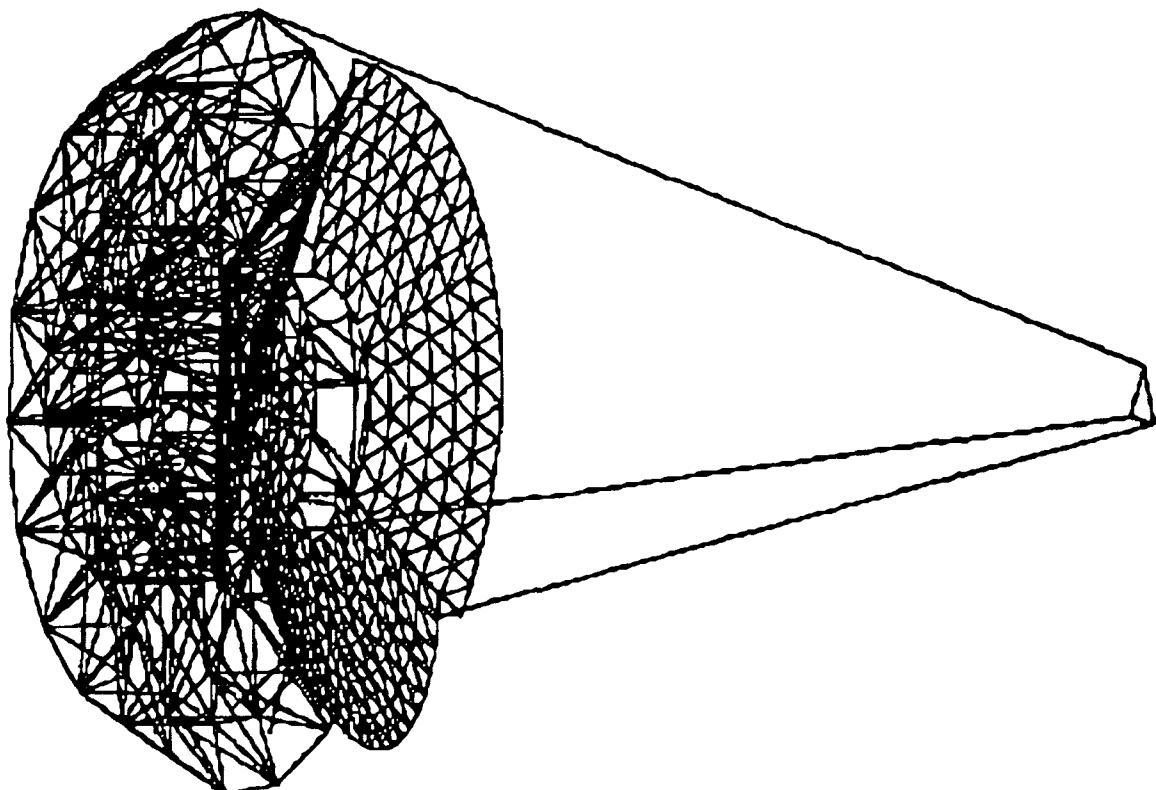
Figure 1.1 SBL Forebody.

18

1.3 Problem Description

Simply stated, the objective of the space-based laser is to place sufficient energy on a distant, rapidly moving target for a long enough duration to accomplish one of several envisioned tasks, all having to do with negation of the threat posed by the target. The control aspects of the SBL problem are numerous and formidable. They encompass several tasks, including high-energy laser beam generation and propagation, satellite platform orbital and attitude control, and acquisition, tracking, and pointing (ATP) functions.

One of the most challenging areas of the SBL control problem is that of beam control. Beam control consists of two main functions: beam pointing and wavefront control, both of which involve steerable and/or deformable optical components. Beam pointing involves placing and maintaining the HEL beam on a desired aimpoint, while wavefront control deals with maintaining a spatially coherent and in phase sequence of light waves.

Wavefront control is the most difficult of the two functions, for it involves extremely precise shape control of the entire SBL primary mirror, which is envisioned as having a diameter of ten meters or more. Due to the large size of this primary mirror, current manufacturing and deployment scenarios call for the primary mirror to be composed of several mirror segments or petals. Longitudinal misalignments of the mirror segment edges result in differences in optical path length for various parts of the laser beam, thereby inducing wavefront phasing errors and potentially destructive interference (see Figure 1.2). Preventing degradation of laser beam quality due to these separations is referred to as the segment phasing aspect of the wavefront control problem [1].
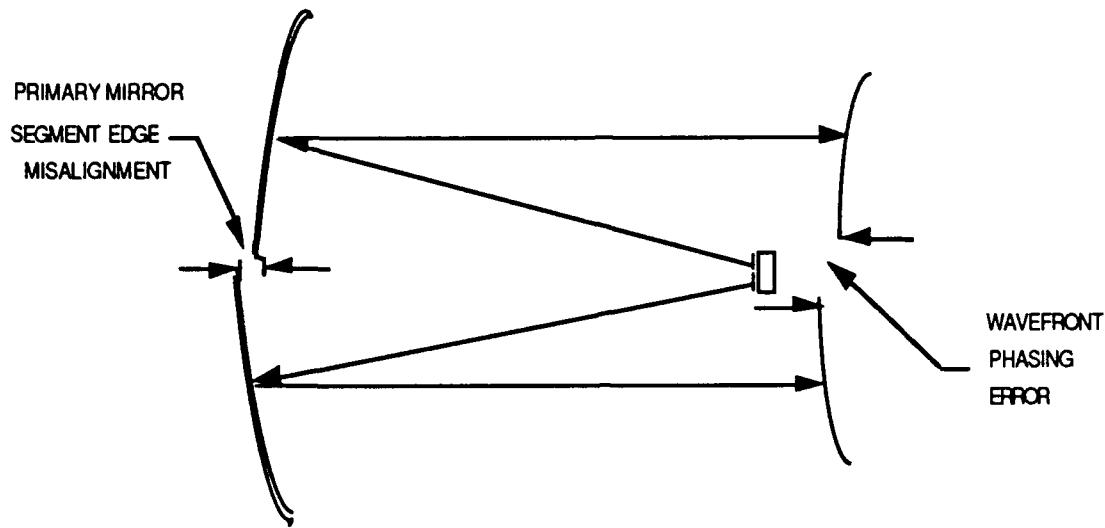
Figure 1.2 Primary Mirror Misalignment and Segment Phasing Error.

Beam pointing is also a complex control task, involving boresight measurements, autoalignment, and beam jitter control functions [2]. Roughly speaking, boresighting involves placing the laser beam on a selected aimpoint, and jitter control involves keeping it there in the presence of disturbances, such as vibrations transmitted through the SBL bulkhead. Autoalignment refers to the static coordination of the various laser beam steering components on the fore and aftbodies of the SBL in order to assure smooth transfer of the HEL beam.

This thesis addresses the problem of simultaneously maintaining tight beam jitter control and minimizing the effects of destructive interference induced via segment phasing. The control algorithms considered are all of a centralized nature, meaning that all sensory data is processed and control authority will be generated from one central computer. Shape control of the primary mirror for the purpose of wavefront control is not addressed, nor are station-keeping and attitude control issues considered. These three control functions will fall under the jurisdiction of actuators different from those used for the beam jitter and segment phasing problems.

1.4   Discussion

Control system synthesis for "large-scale" uncertain systems such as the SBL forebody described above poses many challenges to the control engineer. Typical large-scale systems, such as flexible space structures, often possess very little damping, placing the open-loop poles of such systems close to the s-plane imaginary axis, and thus close to open-loop instability. The presence of a large number of open-loop poles near the instability boundary can lead to difficulties in obtaining closed-loop stability and/or stability robustness. Also, structural models of large-scale systems typically possess dynamics encompassing a large range of open-loop natural frequencies. Large magnitude differences between open-loop poles leads to ill-conditioned system model matrices, making certain numerical computations difficult. Truncation of high frequency dynamics and/or construction of slow/fast control loops may therefore be required.

The size and complexity of large scale systems pose additional problems for the designer. State-space models of large-scale systems are typified by matrices of very large dimensions, hence the categorization as "large-scale". The sheer bulk of such models can cause difficulties with the numerics of solution algorithms, in addition to requiring excessive amounts of valuable computational time and resources. Also, model-based control system design methodologies prescribe high-order compensators for high-order plants. Compensators of such large order are cumbersome to implement due to excessive data processing time requirements, and model reduction methods must therefore be used to obtain simpler realizations.

Approximating the plant with reduced-order models introduces errors into the system, which must then be considered in the design process. Of course, as is necessary for all realistic design problems, the control system design engineer must deal with unpredictable disturbances acting on the system and with unintentional modelling errors or uncertainties, such as parametric uncertainty (uncertainty in knowledge of plant parameters). These considerations lead to robustness of stability and performance issues which the designer must address.

Finally, implementation issues must be examined to assess the practicality of the design being considered. Centralized versus decentralized control authority, determination of allowable order of the compensator and methods of implementation, and software or hardware limitations are just some of the issues to be examined.

Fortunately for the control system engineer, a variety of procedures (pole-placement, LQG/LTR, H_2, H_∞, μ-synthesis, L1, etc.) [3] are currently available to help the designer meet specified performance goals. However, not all of these methods are applicable to any given problem. The control system designer must select the method which yields the best results for the given problem and design objectives. This, then, suggests the need to apply the applicable algorithms to the given problem and compare results to identify the "best" controller for the stated performance goals. For typical large-scale system examples, once an appropriately sized reduced-order model is obtained, the synthesis procedures can be applied to design the various controllers, and closed-loop performance and robustness can be evaluated.

1.5 Thesis Contributions and Outline

Past efforts related to the mirror control problem have employed both single input, single output (SISO) [4,5] and modern multivariable design techniques [1,6]. SISO approaches attempt to model the system dynamics as a series of independent SISO systems, and ignore the potentially significant effects of dynamic coupling between various input-output pairs. Multivariable approaches, on the other hand, allow coupling between inputs and outputs to be fully represented in system models, and therefore yield more accurate results. Since typical large-scale systems are represented by high-order models with multiple sensors and actuators that inevitably possess some degree of dynamic coupling, multivariable design methods are clearly more appropriate for this type of problem. In [1] the LQG/LTR approach was applied to the segment phasing problem, demonstrating the applicability of this multivariable design method to the problem, but failing to achieve desired performance results. In [6] a preliminary analysis addressing the applicability of the μ-synthesis design procedure to the beam jitter disturbance rejection problem was considered.

This thesis carries out a comprehensive multivariable feedback controller synthesis procedure for the combined SBL BEA segment phasing and beam jitter control problems. Details and results of application of H_2 optimal, H_∞ optimal, and H_2/H_∞ loop-shaping design methodologies [7] are presented, and the trade-offs resulting from use of the various design techniques are thoroughly illustrated. The use of model reduction techniques to

22

obtain an appropriately sized design model, in conjunction with use of the Small Gain Theorem to guarantee stability robustness to the truncated dynamics, is also shown. Additionally, a technique for requirements analysis via H_∞ optimization is introduced.

Following compensator design, numerous practical implementation issues are addressed, including digital implementation of continuous-time compensators, reduction of compensator order, design validation via simulation and covariance analysis, and effects of open-loop natural frequency parametric uncertainty. Finally, performance robustness of the final design selected to unmodeled dynamics is verified.

Following this introductory chapter, this thesis is organized as follows:

Chapter 2 provides a concise statement of the problem considered in this thesis. The SBL physical system concept is discussed in detail, coordinate systems are introduced, the SBL mathematical model is derived, and system performance goals are identified.

Chapter 3 discusses results of various analysis methods for the open-loop system, to include nominal system stability, multivariable poles and transmission zeros, and the singular value frequency response and its importance to multivariable control system design.

In Chapter 4 system controllability/observability issues are discussed, and these topics lead directly to an examination of model reduction techniques, which are surveyed and then applied to the SBL BEA model.

Chapter 5 presents a methodology for modern multivariable robust control system design. Various analysis and design techniques are addressed, and all necessary conditions and equations for compensator synthesis and stability robustness analysis are presented.

The topic of Chapter 6 is the Design Plant Model (DPM). Disturbance levels are determined, and application of design techniques to reduced-order system models for the purpose of measurements requirements analysis is performed. The chapter concludes with modeling and augmentation of plant uncertainty so as to complete formulation of the plant model in order that compensator design may proceed.

Chapter 7 provides an in-depth examination of unconstrained bandwidth, robustly

23

stable, and loop-shaped compensator designs. Evaluation of closed-loop performance and stability robustness is performed, compensator singular values are examined, and bandwidth issues are addressed. The various designs are compared, and a single "best" design is selected based on specified performance objectives.

Implementation/validation issues for the selected design are discussed in Chapter 8, including digital implementation issues and sampling requirements, reduced-order compensator studies, transient responses and steady-state covariance analysis, and effects of parametric uncertainty cn open-loop natural frequencies. Verification of performance robustness is also addressed.

Chapter 9 concludes the thesis with a summary of results and conclusions, and some recommendations for further research.

CHAPTER 2

Problem Statement

2.1 Problem Summary

This thesis describes the methods used and procedural steps taken in carrying out a robust controller design procedure for beam control of a space-based laser (SBL) example using three modern methodologies: H_2, H_∞, and H_2/H_∞ loop-shaping techniques. All of these methodologies are applicable to the output feedback problem considered, although the performance objectives of each can be interpreted as being somewhat different. As mentioned previously, the main design objectives are to robustly control the laser beam line-of-sight (LOS) through primary mirror actuation (jitter control), while simultaneously minimizing degradation of beam quality due to misalignments of the mirror segment edges (segment phasing).

2.2 The SBL Model

2.2.1 Physical System Description

Due to its importance with regard to beam jitter and segment phasing control issues, the system model used for this study is limited to the beam expander assembly of the SBL, a

schematic of which appears in Figure 2.1[1]. The aftbody of the SBL is modeled as being dynamically decoupled from the BEA, although an imperfect gimbal isolation subsystem connection allows the aftbody to impart two broadband vibrational torque disturbances to the primary mirror bulkhead support of the forebody. Indeed, these torque disturbances are the primary reason why an active feedback control system is required.
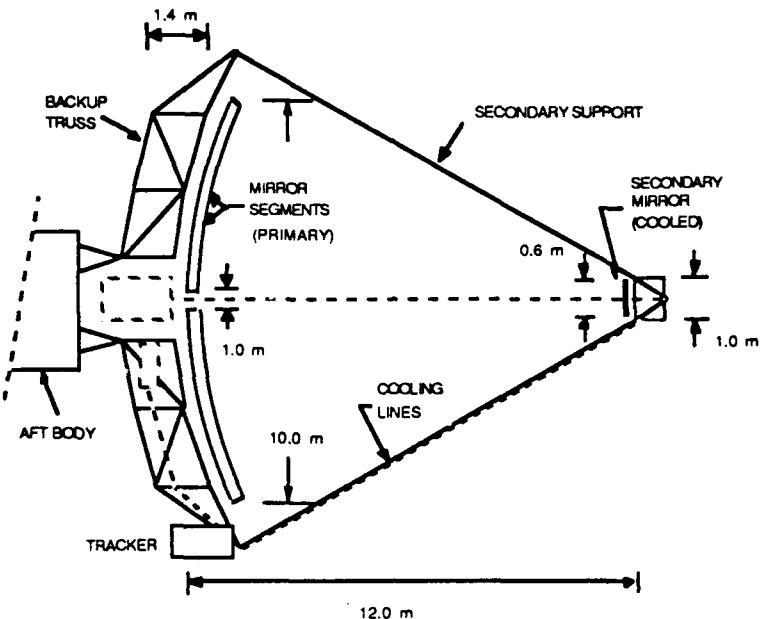
Figure 2.1 SBL Beam Expander Assembly.

In simplified form, the BEA consists of the primary and secondary mirrors, structural supports, 120 surface figure actuators, 24 rigid body push-pull mirror segment reaction structure force actuators (6 per segment), a line-of-sight/jitter error sensing subsystem, and 27 mirror segment edge translation sensors. The optical design of the beam expander consists of a 10-m diameter paraboloidal primary mirror with a 12-m focal length, and a confocal secondary mirror with a 0.8-m focal length and a 0.67-m diameter. Due to deployment and manufacturing limitations imposed by its large size, the primary mirror is made up of four flexible mirror segments (1 center and 3 outer segments), the shapes of which are controlled by surface figure actuators connecting the mirror segments to rigid reaction plate structures. The four primary mirror segment reaction structures are in turn

---

[1] The SBL model, developed under Independent Research and Development funding at the C.S. Draper Laboratory, possesses generic characteristics typical of SBL conceptual designs.

kinematically mounted to a rigid bulkhead support, placed so that the mirror segments nominally form a parabola when aligned. The center segment is shaped like a parabolic annulus, and the outer segments simply extend the parabola. The one meter diameter circular hole through the middle of the center segment allows the high-energy laser beam to pass forward from the aftbody to the secondary mirror, which is held in place by a graphite-epoxy tripod metering truss. The secondary mirror reflects the HEL beam back to the primary mirror, which then focuses the magnified beam downrange on a target.

Fine pointing of the beam is accomplished via the six segment piston actuators connecting each segment reaction structure to the bulkhead support. These six actuators are arranged in three pairs, with each pair located at the vertex of an imaginary equilateral triangle (see Figure 2.2). Each actuator pair has one in-plane and one out-of-plane piston. The direction of motion of each in-plane piston is tangent to the circle connecting the vertices of the imaginary equilateral triangle, while the out-of-plane pistons move through the vertices in a plane perpendicular to the triangle (in and out of the plane of Figure 2.2). Thus arranged, each actuator pair triad represents a redundant 3-dimensional orthogonal basis, allowing for six independent actuation degrees-of-freedom per petal. These degrees-of-freedom can be used to completely control the three dimensional translation and rotation of each petal, within the range of motion allowed by the piston actuators.
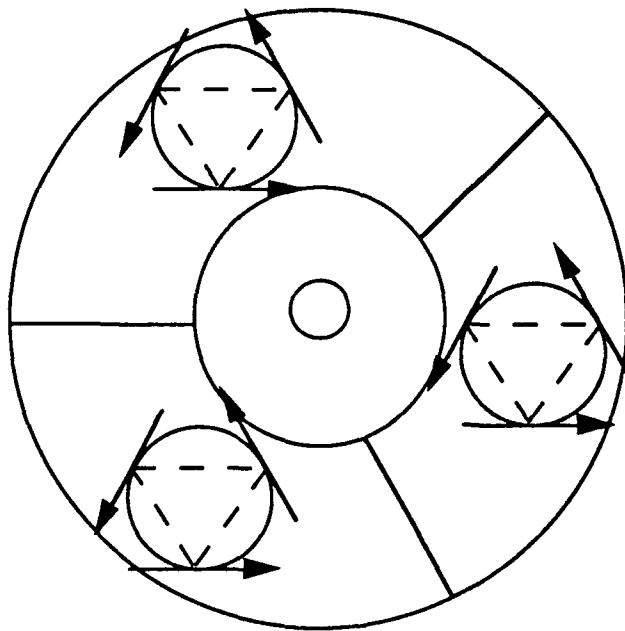
Figure 2.2 Outer Segment Position Actuator Configuration.

For purposes of discussion of the sensors, it is convenient to define a local orthogonal coordinate system, *RTZ*, for each nodal point on the BEA finite element grid (see Figure 2.3). The coordinate frame is determined by the nodal point, the point located at the middle of the center segment, and the point corresponding to the centroid of the secondary mirror. The point located at the middle of the center segment is defined as the origin for all these axis systems, with lines connecting the origin and the other two points mentioned above determining axis directions. The line from the origin through the centroid of the secondary mirror determines the *Z* direction (the nominal beam pointing direction), while the line from the origin to any point on the BEA determines the radial or *R* direction. Finally, the tangential or *T* direction is determined from the tangent to the circle about the origin that passes through the given nodal point. It is also convenient to define an orthogonal axis system, *XYZ* (see Figure 2.4), with origin and *Z* direction the same as for the *RTZ* axis systems, *Y* direction pointing toward the "top" of the BEA, and *X* direction defined to yield a right-handed coordinate system .
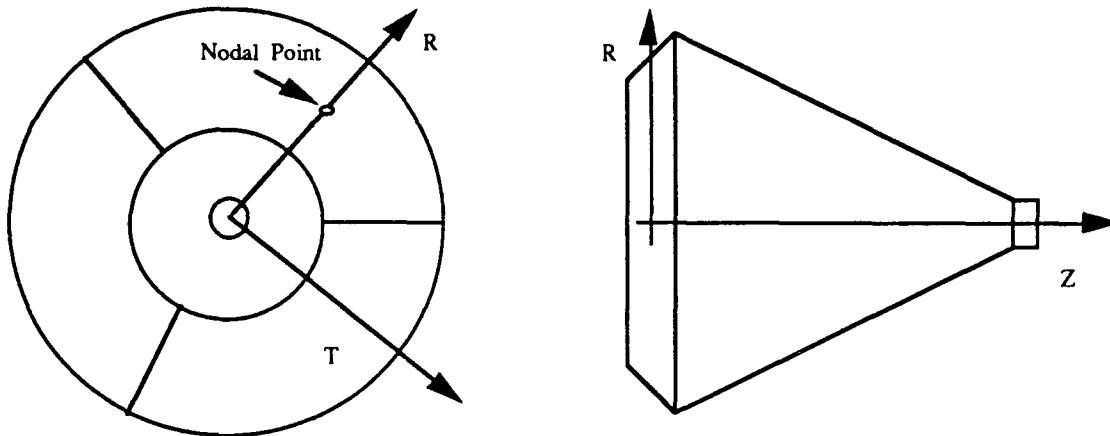
Figure 2.3 BEA RTZ Coordinate Axis System.

28
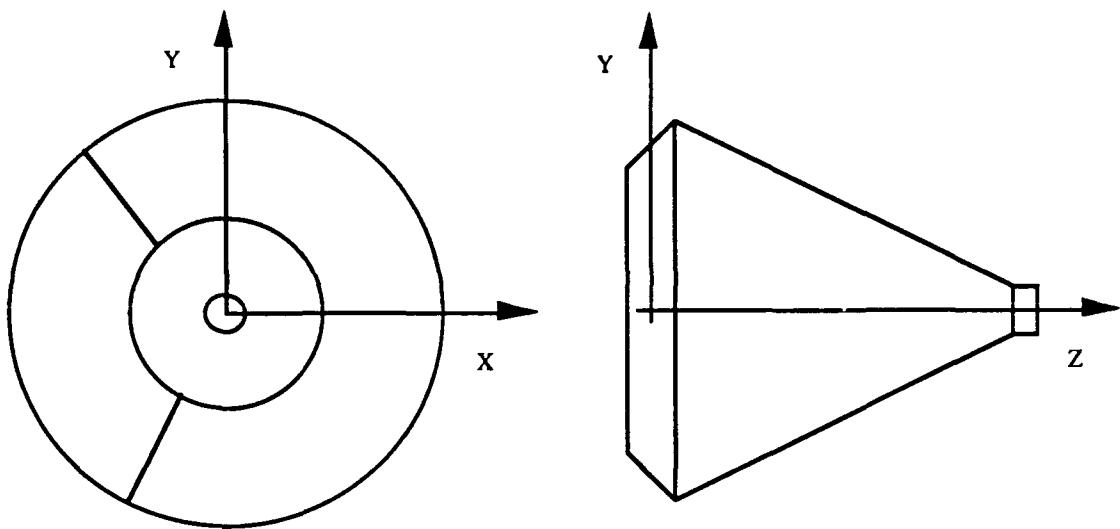
Figure 2.4 BEA XYZ Coordinate Axis System.

An outgoing wavefront sensor, colocated with the secondary mirror, is equipped with sensors for detecting line-of-sight/jitter errors in a plane perpendicular to the line-of-sight. These measurements come in the form of angular deviations of the HEL beam wavefront normal from the LOS about both the X and Y coordinate axes. At 21 points along the primary mirror segment edges, edge gap sensors provide information on the size of separations between the plate edges resolved in RTZ coordinates, as depicted in Figure 2.5. At points 1, 5, and 9, three measurements are available to provide relative misalignment data between the three petals that meet at those points, while the 18 other individually located sensors yield one measure each, totaling 27 segment phasing measurements available. Combined with the wavefront sensor, these edge gap sensors provide the necessary measurements for beam jitter and segment phasing control designs.
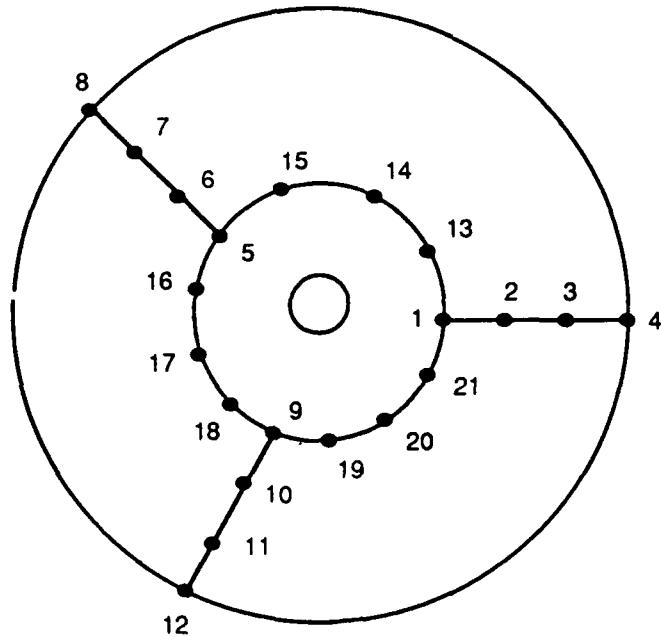
Figure 2.5 Segment Phasing Sensor Locations.

In addition to the wavefront and segment phasing sensors, a wide-field-of view infrared tracker attached to the primary mirror bulkhead support provides information for determining the LOS to the target.

2.2.2 Mathematical Model

In Chapter 5, a framework for robust control system synthesis is discussed which assumes that the system to be controlled, as modeled by the transfer function G(s), can be depicted as in the block diagram of Figure 2.6. In the figure, K(s) represents a dynamic output-feedback compensator, Δ(s) represents any uncertainties present in the open-loop plant, z and w are the respective input and output to the uncertainty block, d includes all exogenous signals acting on the plant (disturbances, sensor noises, and reference inputs), e is the performance or error variable (to be kept small), u is the control input, and y is the measured output.
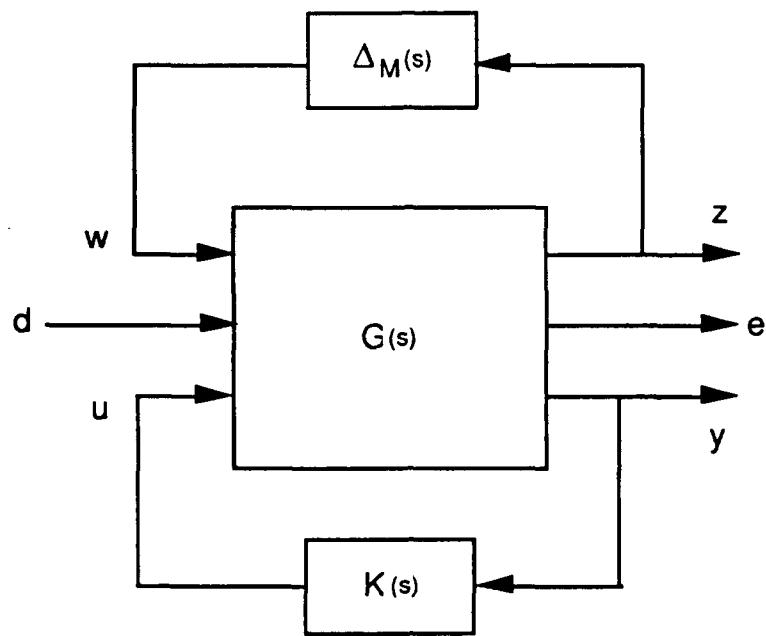
Figure 2.6 Block Diagram Representation of Open-Loop Plant
(3-Block Form).

It is further assumed that the dynamics of the open-loop plant can be represented mathematically by a set of first-order, linear differential and matrix algebraic equations of the form

$$\dot{x}(t) = A\,x(t) + B_1\,w(t) + B_2\,d(t) + B_3\,u(t)$$

$$z(t) = C_1\,x(t) + D_{11}\,w(t) + D_{12}\,d(t) + D_{13}\,u(t)$$

$$e(t) = C_2\,x(t) + D_{21}\,w(t) + D_{22}\,d(t) + D_{23}\,u(t)$$

$$y(t) = C_3\,x(t) + D_{31}\,w(t) + D_{32}\,d(t) + D_{33}\,u(t) \tag{2.1}$$

where $x(t)$ represents a vector consisting of the "state variables" of the system. In contrast to the 3-block representation used for control system design, however, the linear systems analysis and model reduction of Chapters 3 and 4 require that the open-loop plant be represented by a single block transfer function, as shown in Figure 2.7. A one-block system model of the BEA segment phasing/jitter control system for use in Chapters 3 and 4

is now derived. In the course of this derivation, intermediate equations consistent with the 3-block system representation used in Chapter 5 are presented. These intermediate equations are revisited in Section 5.3, when formulation of the complete 3-block system model is addressed.
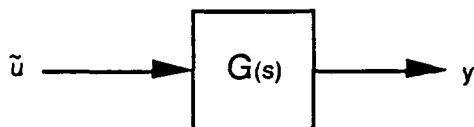
Figure 2.7 Block Diagram Representation of Open-Loop Plant
(1-Block Form).

In order to obtain a mathematical model of the SBL forebody for analysis and control system design purposes, a NASTRAN finite element program was employed. Although the BEA is theoretically a distributed parameter system with an infinite number of modes, the primary mirror can be represented to sufficient accuracy by modeling the system as consisting of a finite number of masses lumped at convenient node points. The motion of these lumped masses is then assumed to fully represent the structure's dynamics. Since the secondary mirror is much smaller and stiffer than the primary mirror, it is modeled as a rigid body kinematically mounted to the metering truss. The primary mirror bulkhead support and the metering truss are modeled using beam bending elements, and additional lumped masses are included to account for nonstructural masses, such as the mirror cooling system and electronics, and the target tracker. Since the segment position actuators are high-speed force actuators, they are modeled as linear springs with time constants much faster than the system dynamics.

Finite element theory and Newton's 2nd Law of Motion is used to derive the second order matrix differential equation that represents the system dynamics

$$M \ddot{z}(t) + K z(t) = B_D d_T(t) + B_A u(t) \tag{2.2}$$

where M and K respectively represent mass and stiffness matrices, z represents the nodal displacement vector, d_T represents the two element torque disturbance vector in Newton-meters (N-m), B_D is the disturbance influence matrix, u represents the 24 element actuator control vector in Newtons (N), and B_A is the control influence matrix.

A matrix Φ whose columns are the normalized mode shapes is found such that

$$\Phi^T M \Phi = I$$

and

$$\Phi^T K \Phi = \Omega^2$$

where I is the appropriately dimensioned identity matrix, and Ω represents a diagonal matrix of natural frequencies associated with each mode of the system.

A transformation to modal coordinates is performed by letting

$$z(t) = \Phi \, \eta(t)$$

and premultiplying (2.2) by Φ^T to yield

$$\Phi^T M \Phi \ddot{\eta}(t) + \Phi^T K \Phi \eta(t) = \Phi^T B_D \, d_T(t) + \Phi^T B_A \, u(t) \qquad (2.3)$$

or

$$\ddot{\eta}(t) + \Omega^2 \eta(t) = \Phi^T B_D \, d_T(t) + \Phi^T B_A \, u(t) \qquad (2.4)$$

Finally, a small, uniform damping term is augmented to (2.4) to represent the lightly damped nature of the large-scale flexible structure

$$\ddot{\eta}(t) + 2 \zeta \Omega \dot{\eta}(t) + \Omega^2 \eta(t) = \Phi^T B_D \, d_T(t) + \Phi^T B_A \, u(t) \qquad (2.5)$$

where the damping factor ζ is taken to be 0.005 for all structural modes.

Of the more than 1000 modes generated by the finite element model, only the first 195 mode-pairs were retained, corresponding to natural frequencies between 10^{-5} and 10^3 radians per second. Modes at frequencies higher than 10^3 radians per second were considered both unreliable from a modeling standpoint and well beyond the bandwidth of interest for controller design.

33

By letting the modal variables, $\eta(t)$, be the first 195 elements of the state vector $x(t)$, and taking the second 195 elements to correspond to their derivatives

$$x(t) = \begin{bmatrix} \eta(t) \\ \dot{\eta}(t) \end{bmatrix}$$

(2.5) can be converted to the linear state-space form

$$\dot{x}(t) = \begin{bmatrix} 0 & I \\ -\Omega^2 & -2\zeta\Omega \end{bmatrix} x(t) + \begin{bmatrix} 0 \\ \Phi^T B_D \end{bmatrix} d_T(t) + \begin{bmatrix} 0 \\ \Phi^T B_A \end{bmatrix} u(t) \tag{2.6}$$

or

$$\dot{x}(t) = A\,x(t) + B_{21}\,d_T(t) + B_3\,u(t) \tag{2.7}$$

Finally, combining both input terms into a single vector, $\widetilde{u}(t)$

$$\widetilde{u}(t) = \begin{bmatrix} u(t) \\ d_T(t) \end{bmatrix}$$

yields

$$\dot{x}(t) = A\,x(t) + \begin{bmatrix} B_3 & B_{21} \end{bmatrix} \widetilde{u}(t) \tag{2.8}$$

or

$$\dot{x}(t) = A\,x(t) + B\,\widetilde{u}(t) \tag{2.9}$$

The observation or measurement equation for the BEA feedback problem is

$$y(t) = C\,x(t) + \theta(t) \tag{2.10}$$

where $y(t)$ consists of both LOS and segment phasing measurements in radians and meters respectively, corrupted by an assumed broadband noise term $\theta(t)$. Equations (2.9) and

34

(2.10) provide an open-loop system model in a form suitable for the linear multivariable systems analysis and model reduction of Chapters 3 and 4.

2.3 Performance Specifications

Performance objectives for the SBL beam control problem considered consist of maintaining an overall level of "beam quality", as determined by contributions from beam LOS jitter and segment phasing effects. In [8] methods are developed for computing the far-field beam complex amplitude and intensity distributions for a laser beam propagating from a circular aperture using Fresnel and Fraunhofer diffraction theory. Beam jitter and segment phasing effects are then accounted for in terms of the degradations they induce in the far-field intensity distribution.

In [2] it is shown that the far-field intensity distribution for a beam propagating from a circular aperture closely resembles a Gaussian distribution. If the far-field intensity distribution is assumed Gaussian, and the effects of beam jitter are also modeled as a bivariate Gaussian probability density function with independent, identically distributed components, a closed-form solution for the far-field intensity distribution under the influence of jitter effects is obtainable. The equations resulting from these assumptions indicate that beam jitter tends to spread the far-field energy distribution out over a greater area, while simultaneously reducing the peak intensity of the distribution. Thus, beam jitter tends to lessen the ability of the laser to concentrate maximum energy on a small target area, which it must do in order to damage or destroy its target. The key figure-of-merit chosen for beam jitter effects in this study is the peak intensity attenuation or loss factor, which in [2] is shown to be

$$L = (1 + 4\sigma_0^2)^{-1} \qquad (2.11)$$

where σ_0 is the root-mean-square (RMS) angular LOS jitter error in microradians.

The attenuation of peak far-field intensity due to phase aberrations is given by a quantity called the Strehl ratio, S, [8] which can be approximated by the relatively simple algebraic formula

$$S \cong (1 - 0.5\,\sigma_\phi^2)^2 \tag{2.12}$$

by defining σ_ϕ as the RMS phase error in the sense of a spatial average over the assumed circular aperture of the primary mirror [2]. The phase error can in turn be related to changes in optical path length via

$$\sigma_\phi = \frac{2\pi}{\lambda}\,\sigma_{\Delta l} \tag{2.13}$$

where $\sigma_{\Delta l}$ represents the RMS longitudinal or Z direction separations (segment phasing errors) between primary mirror segment edges.

The total attenuation of peak intensity can then be approximated as the product of the two loss factors L and S:

$$LT = \frac{\left(1 - 2\dfrac{\pi^2}{\lambda^2}\,\sigma_{\Delta l}^2\right)^2}{\left(1 + 4\,\sigma_o^2\right)} \tag{2.14}$$

Figure 2.8 depicts level curves of total peak intensity attenuation due to both beam jitter effects and segment phasing wavefront aberration, as determined from (2.14).
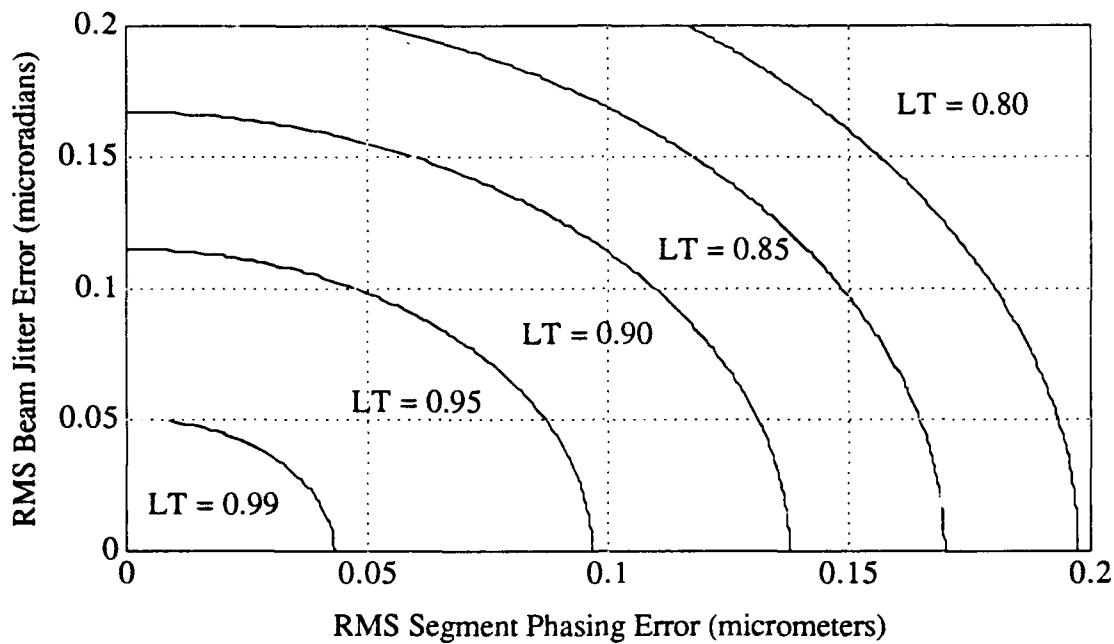
Figure 2.8 Equal Peak Intensity Attenuation Contours.

The total loss factor defined by (2.14) is the primary system performance measure. Arbitrarily, a performance specification total loss factor of no less than 0.85 was chosen for the BEA control system From Figure 2.8 it can be seen that this performance specification will be met as long as RMS beam jitter error (σ_0) does not exceed 0.1 microradians, and the RMS segment phasing error $(\sigma_{\Delta l})$ does not exceed 0.15 micrometers. These figures represent upper bounds on allowable system errors, which the feedback controller must maintain.

By identifying linear combinations of the state variables that yield LOS and segment phasing measures and incorporating scaling that reflects the performance specifications derived above, an error (performance) vector for use in (2.1) can be defined

$$\bar{e}(t) = \bar{C}_2 \, x(t) \qquad (2.15)$$

such that if $\sigma_e < 1$, then performance goals are met. Equations (2.8) and (2.15) also provide a one-block system representation that is used for analysis in Chapters 3 and 4.

37

To this point, all error variables have been assumed to be random with Gaussian probability density functions. This corresponds to an assumption that the torque and measurement noise disturbances are also stochastic, and can be represented as random Gaussian variables. However, since space-based lasers have not yet been constructed and tested, the precise nature and/or spectral properties of the disturbances acting on the system are not well known. Therefore, we will alternatively assume that system performance specifications can be interpreted in a deterministic manner, by replacing the RMS value of a vector quantity or signal with its 2-norm, where the 2-norm of the vector signal e(t) is defined by

$$\| e(t) \|_2^2 \;=\; \int_0^\infty e(t)^T e(t)\, dt \;=\; \frac{1}{2\pi} \int_{-\infty}^\infty e(j\omega)^H e(j\omega)\, d\omega$$

(2.15)

Under deterministic assumptions, the disturbances can be thought of as broadband noise with unspecified spectral content, but bounded energy (2-norm). The equivalence of the stochastic and deterministic optimal control problems implied by assumptions concerning the nature of the disturbances is demonstrated in Section 3.4.2.

CHAPTER 3

Open-Loop System Analysis

3.1 Introduction

In this chapter, the properties of the open-loop BEA system model derived in Chapter 2 are investigated. In Section 3.2, nominal system stability is motivated in terms of bounded-input, bounded-output arguments, and stability of the BEA model is examined. Section 3.3 provides a definition of multivariable transmission zeros, and discusses results of application of a generalized eigenvalue problem (GEP) computation algorithm to the BEA model. The singular value frequency response and its "principal gain" interpretation are the main topics of Section 3.4, which concludes the chapter.

3.2 Nominal Stability

As shown in Chapter 2, the input-output time behavior of the open-loop BEA model can be characterized by a set of first order, constant-coefficient linear differential and matrix algebraic equations of the form

$$\dot{x}(t) = A\,x(t) + B\,u(t)$$

$$y(t) = C\,x(t) \tag{3.1}$$

which are known to have the solution [9]

$$y(t) = C e^{At} x(0) + C \int_0^t e^{A(t-\tau)} B u(\tau) d\tau$$

$$(3.2)$$

where the first term on the right-hand-side of (3.2) is called the initial condition response, the second term is labeled the forced response, and the initial time (t_0) has been assumed to be zero for simplicity.

Nominal stability for a linear time-invariant (LTI) system described by (3.1) is commonly defined in terms of bounded input-bounded output (BIBO) stability. That is, given a bounded input function u(t), the system of (3.1) is said to be nominally stable if the output y(t) remains bounded for all time after t_0. Here, a function f is said to be bounded as long as there exists a finite number p such that the norm of the function evaluated at t, f_t, is less than or equal to p for all t after t_0 [10] (i.e. the function f is bounded as long as

$$\| f_t \|_* \leq p \quad \text{for all } t > t_0$$

$$(3.3)$$

for a given norm defined over the linear space of which f_t is a member). As is discussed in Section 3.4.2, a commonly employed norm used to bound vector inputs and outputs of multivariable, continuous time systems is the Euclidean or vector 2-norm defined for the vector f_t as

$$\| f_t \|_2 = \sqrt{f_t^H f_t}$$

where the superscript H indicates the Hermitian (complex-conjugate transpose) of a vector.

As can be seen from (3.2), if u_t remains bounded for all t after t_0, then the time behavior of y(t) is governed by the matrix exponential term e^{At}. If we assume that all of the eigenvalues, λ_i, and right eigenvectors, v_i, of the n x n matrix A are distinct, i.e.

$$A v_i = \lambda_i v_i$$

can be solved for all i = 1 to n, then the matrix exponential can be rewritten

$$e^{At} = V e^{\Lambda t} V^{-1}$$

$$(3.4)$$

40

by letting

$$V = \begin{bmatrix} | & | & | & | \\ v_1 & v_2 & \cdots & v_n \\ | & | & | & | \end{bmatrix}$$

and

$$e^{\Lambda t} = \text{diag}\left(e^{\lambda_1 t}, e^{\lambda_2 t}, \ldots e^{\lambda_n t}\right) \tag{3.5}$$

If λ_i is expressed as a complex number,

$$\lambda_i = \sigma + j\,\omega_d$$

$$= \omega_n \zeta + j\,\omega_n \sqrt{1 - \zeta^2} \tag{3.6}$$

where

σ = the real part of λ_i

ω_d = the imaginary part of λ_i
   = the damped natural frequency associated with the ith state

$j = \sqrt{-1}$

ω_n = the undamped natural frequency associated with the ith eigenvalue

ζ = the damping ratio of the ith eigenvalue

then (3.2)-(3.6) mandate that the eigenvalues of the A matrix have negative real parts in order for the matrix exponential to decay with time and yield a bounded system output.

Since the eigenvalues of the system A matrix are also the poles of the open-loop transfer function

41

$$G(s) = C(sI - A)^{-1} B \qquad (3.7)$$

the system of (3.1) is said to possess BIBO stability, if and only if all the system poles have negative real parts.

One useful way of presenting system stability characteristics graphically, called an open-loop pole plot, results from plotting the system eigenvalues in the complex plane. Any unstable poles immediately show up in the right half plane of such a figure. The further left of the imaginary (or $j\omega$-) axis stable system poles are, the faster the exponential of (3.4) decays, and the "more stable" such poles are said to be. System poles lying directly on the $j\omega$-axis are said to be marginally stable, producing a response that neither grows nor decays with time. Also, since the distance from any pole to the origin is

$$|\lambda_i| = \sqrt{\sigma^2 + \omega_d^2}$$

$$= \sqrt{\omega_n^2 \zeta^2 + \omega_n^2 (1 - \zeta^2)} = \omega_n$$

and since the sine of the angle, β, made between a straight line connecting the origin and any pole and the $j\omega$-axis is

$$\sin(\beta) = \frac{\omega_n \zeta}{\omega_n} = \zeta$$

the undamped natural frequency and the damping ratio of any pole is easily determined from the pole plot.

An open-loop pole plot for the BEA system model derived in Chapter 2 appears in Figure 3.1. As can be seen from the figure, the open-loop BEA model is nominally stable since all its poles lie to the left of the imaginary axis. Also evident from Figure 3.1 is the uniform damping assigned to all structural modes, which produces the straight-line pattern of poles extending away from the origin at a constant angle of 0.005 radians (0.286 degrees) from the $j\omega$-axis. Note the unequal scaling on the real and imaginary axes, which makes the open-loop poles appear farther left of the $j\omega$-axis than they actually are.
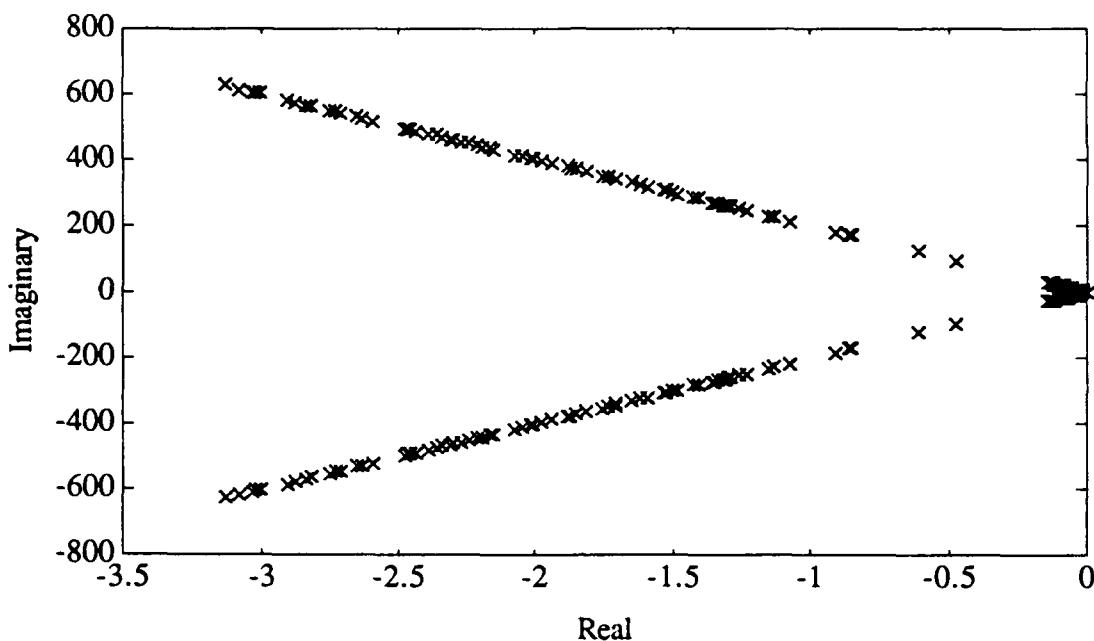
Figure 3.1 Open-Loop Pole Plot (Note Scale Differences).

3.3 Multivariable Transmission Zeros

In a single-input, single-output (SISO) setting, transfer function zeros are defined as frequencies at which a non-zero input produces an identically zero system output. This concept of an "input-absorbing frequency" [3] is generally maintained when defining a system zero in a multi-input, multi-output (MIMO) setting. The system of (3.1) is said to possess a multivariable transmission zero at the frequency, z_k, if there exists an initial condition, x_0, and a control vector, u_k, not both zero, such that if

$$u(t) = u_k \, e^{z_k t}$$

then

$$y(t) = 0 \quad \text{for all } t > 0$$

A consequence of this definition is that the open-loop transfer function G(s) loses rank

43

when evaluated at z_k, and, therefore, so does the Rosenbrock system matrix [7] given by

$$R(s) = \begin{bmatrix} sI - A & -B \\ -C & 0 \end{bmatrix} \tag{3.8}$$

Thus, as long as the state-space realization of the system (3.1) is minimal[2] and square (has the same number of inputs and outputs), then the multivariable transmission zeros of the system can be located by solving the generalized eigenvalue problem (GEP)

$$M v = z_k N v \tag{3.9}$$

where

$$M = \begin{bmatrix} A & B \\ C & 0 \end{bmatrix}$$

and

$$N = \begin{bmatrix} I & 0 \\ 0 & 0 \end{bmatrix}$$

Note that if the open-loop transfer function has a non-zero feedthrough term, D, then this matrix would replace the zero 2-2 elements of R(s) and M above. If the system being considered is not minimal, it must be made so before this approach may be applied. Also, this algorithm may be applied to non-square systems by augmenting the system matrices with sufficient rows or columns containing random entries to "square-up" the system, iterating the GEP, and identifying the invariant zeros [11].

The presence of multivariable transmission zeros in the open-loop system is important to detect, for three main reasons. The first reason is that zeros at the same locations as open-loop poles may result in pole-zero cancellations, creating an uncontrollable or

---

[2] The term minimal is used to describe a state-space realization that is both completely controllable and completely observable (See Section 4.2 for definitions of these terms). The Rosenbrock system matrix of a non-minimal realization loses rank when evaluated at frequencies corresponding to uncontrollable/unobservable poles, as well as when evaluated at zero frequencies. Uncontrollable/unobservable poles must therefore first be removed before the generalized eigenvalue problem test can be said to yield system zeros.

44

unobservable system model[3]. To motivate the second reason, consider Figure 3.2, which shows the closed-loop transfer from u to y, with output disturbances (measurement noise) present. The closed-loop transfer function from θ to y (broken at the plant output) is called the output sensitivity function, $S_o(j\omega)$, and is given by the relation

$$S_o(j\omega) = \{I - G(j\omega) K(j\omega)\}^{-1} \tag{3.10}$$

The presence of an open-loop right-half plane (non-minimum phase) zero imposes certain limitations on achievable performance of a system under feedback, expressed as a weighted integral constraint on the logarithm of the maximum singular value of $S_o(j\omega)$ [12],

$$\int_0^\infty \log \sigma_1 [S_o(j\omega)] W(z,\omega) \, d\omega \geq 0 \tag{3.11}$$

where W is the weighting function

$$W(z,\omega) = \frac{x}{x^2 + (y - \omega)^2} + \frac{x}{x^2 + (y + \omega)^2}$$

for a complex zero at $z = x + jy$. In combination with the multivariable generalization of the well-known Bode integral constraint on system output sensitivity for open-loop stable systems [13],

$$\sum_{i=1}^n \int_0^\infty \log \sigma_i [S_o(j\omega)] \, d\omega = 0 \tag{3.12}$$

(3.11) and (3.12) indicate that designing to make $S_o(j\omega)$ "small" in certain frequency ranges forces $S_o(j\omega)$ to be "large" in other frequency bands. For open-loop stable systems with no right-half-plane zeros, the area under the log $S_o(j\omega)$ singular value curves indicating output disturbance attenuation equals the area under the log $S_o(j\omega)$ singular value curves indicating output disturbance amplification. For non-minimum phase systems, the area of output disturbance amplification may be greater than the area of output disturbance attenuation. These integral constraints on system output sensitivity provide useful insight

---

[3] Reference Section 4.2 for definitions of controllability/observability.

45

into what kind of limitations on achievable performance to expect prior to attempts at compensator synthesis. The third and final reason why it may be important to identify MIMO zeros is that the presence of non-minimum phase zeros may adversely affect the system transient response.
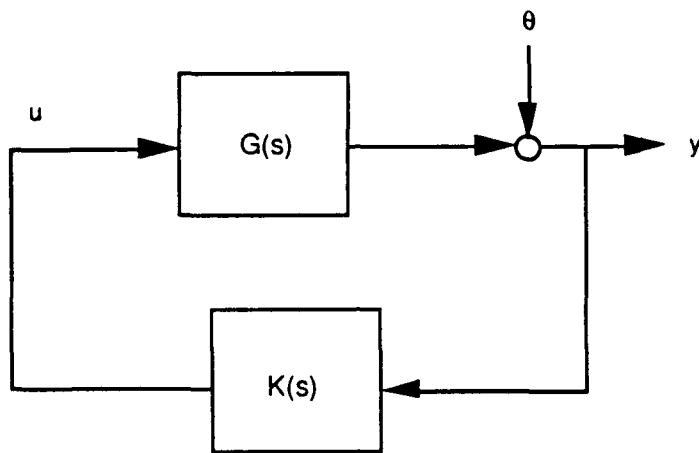
Figure 3.2 Closed-Loop Transfer from u to y
(with sensor noise present).

Although the open-loop system of (3.1) has 24 inputs and 29 outputs (27 segment phasing and 2 LOS), in Section 5.3.3 a requirements analysis process is carried out to reduce the number of measurements to 8 (6 segment phasing and 2 LOS). Since the 8 measurement model is the one actually used for design, this is the system in whose zeros we are interested; and, since this system's transfer function is non-square (8 x 24), the algorithm of augmenting 16 rows of random entries twice and iterating the GEP described above was attempted. This method failed to identify any MIMO transmission zeros. Therefore, the 16 rows of random entries were changed to rows of zero entries, yielding an open-loop system of the form

$$\begin{bmatrix} y \\ y_f \end{bmatrix} = \begin{bmatrix} C(sI - A)^{-1} B \\ 0(sI - A)^{-1} B \end{bmatrix} u$$

(3.13)

where y_f is a fictitious output identically equal to zero. The system of (3.13) is now square and loses rank only where the open-loop design model loses rank. The MIMO transmission zeros of (3.13) are therefore equal to the zeros of (3.1), and can now be

46

computed via solution of the GEP. The 96 multivariable transmission zeros obtained by solving the GEP for the system of (3.13) are plotted in Figures 3.3 and 3.4.
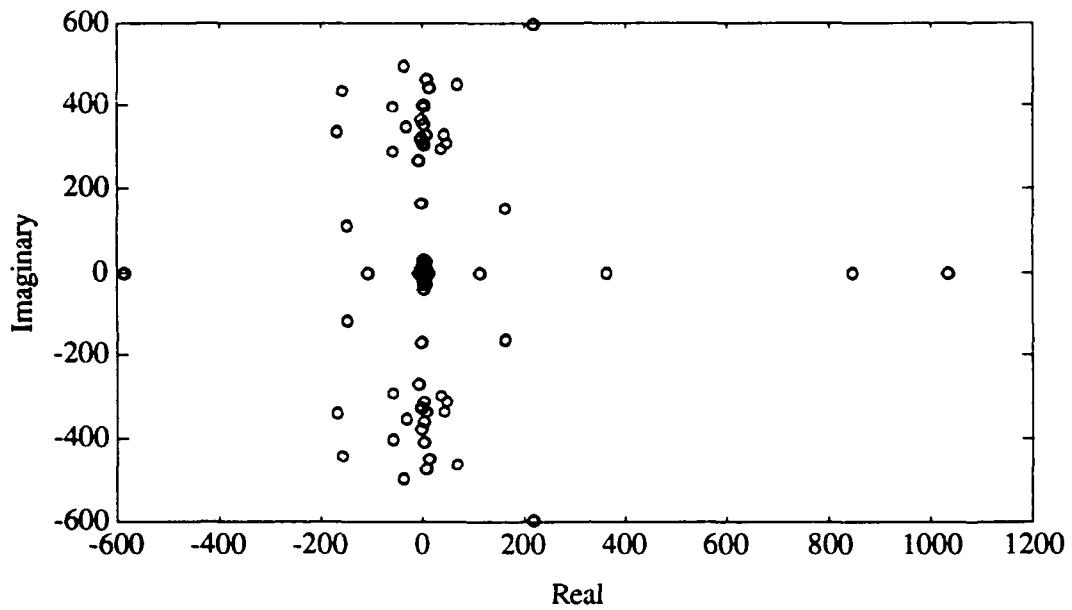
Figure 3.3 Open-Loop Multivariable Transmission Zeros.
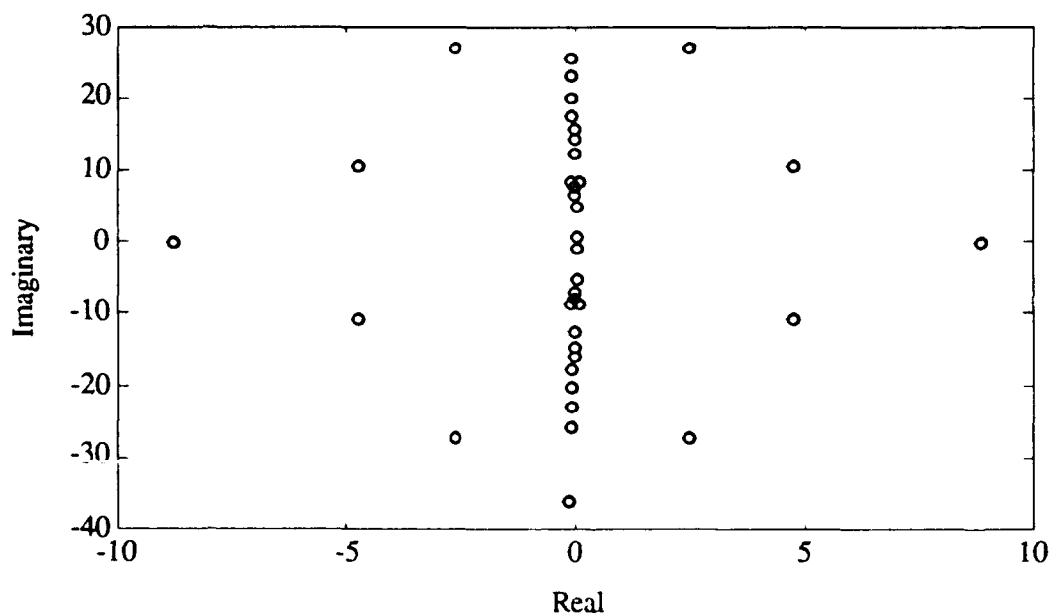
Figure 3.4 Open-Loop Multivariable Transmission Zeros
(Close-up About the Origin).

47

As can be seen from the figures (especially Figure 3.4), many of the MIMO transmission zeros are clustered along the jω-axis, creating the possibility of near pole-zero cancellations. A small number of zeros are located on the real axis, and the presence of right-half plane zeros in the design model is also obvious.

3.4 Singular Value Frequency Response

3.4.1 Definitions

As mentioned in Section 3.2, a finite-dimensional LTI system with state-space representation

$$\dot{x}(t) = A\,x(t) + B\,u(t)$$

$$y(t) = C\,x(t)$$

has an open-loop transfer function

$$G(s) = C\,(sI - A)^{-1}\,B$$

which, when evaluated at s = jω, yields the frequency dependent behavior of the system. In a SISO system, a single gain and phase at each frequency is sufficient to characterize the relation of input to output. In a multivariable setting, however, a single gain is not enough, and the singular value frequency response is required.

The singular value frequency response of a system is obtained by computing the singular value decomposition (SVD) of the complex matrix G(jω) over the frequency range of interest, where the SVD of the m x n matrix G of rank k is defined

$$G = U\,\Sigma\,V^H \tag{3.10}$$

and U is an m x m unitary matrix with columns corresponding to the left singular vectors of G, u_i; V is an n x n unitary matrix with columns corresponding to the right singular vectors of G, v_i; and Σ is an m x n diagonal matrix of the form

48

$$\Sigma = \begin{bmatrix} \sigma_1 & & & & \\ & \ddots & & & 0 \\ & & \sigma_k & & \\ & & & 0 & \\ 0 & & & & \ddots \\ & & & & & 0 \end{bmatrix}$$

where the σ_i are the strictly positive singular values of matrix G in order of decreasing magnitude. The elements of the singular value decomposition are given by

$$G^H G v_i = \lambda_i v_i$$

$$G G^H u_i = \lambda_i u_i$$

and

$$\sigma_i (G) = \sqrt{\lambda_i (G^H G)} = \sqrt{\lambda_i (GG^H)}$$

where superscript H again represents the Hermitian of a matrix, and i runs from 1 to k.

3.4.2 Importance of Singular Values to LTI Systems

The importance of the singular value decomposition to linear systems lies in its interpretation in the context of induced matrix norms. If $\|u\|_2$ denotes the Euclidean or vector 2-norm of a complex-valued vector u with n elements,

$$\| u \|_2 = \sqrt{u^H u} \tag{3.11}$$

then the induced matrix norm of G over the vector space spanned by all n element complex-valued vectors, C^n, is defined as

$$\| G \|_{i_2} = \sup_{u \neq 0} \frac{\| G u \|_2}{\| u \|_2} \tag{3.12}$$

49

where the notation sup is short for supremum, representing a least upper bound. By definition, the induced 2-norm of G over C^n equals the maximum vector 2-norm amplification or gain experienced by any n element vector acted upon by the matrix G.

If we restrict ourselves to input vectors with unity bounded vector 2-norms, $\| u \|_2 \leq 1$, then (3.11) becomes

$$\| G \|_{i_2} = \sup_{\| u \|_2 \leq 1} \| G u \|_2 \tag{3.13}$$

Utilizing (3.9), (3.13) can be written

$$\| G \|_{i_2} = \sup_{\| u \|_2 \leq 1} \| U \Sigma V^H u \|_2 \tag{3.14}$$

which is maximized by choosing u to equal the first right singular vector of matrix G, v_1, so that

$$\| G \|_{i_2} = \| U \Sigma \begin{bmatrix} 1 \\ 0 \\ \vdots \\ 0 \end{bmatrix} \|_2 \tag{3.15}$$

or

$$\| G \|_{i_2} = \| U \begin{bmatrix} \sigma_1 \\ 0 \\ \vdots \\ 0 \end{bmatrix} \|_2 = \| u_1 \sigma_1 \|_2 \tag{3.16}$$

Finally, invoking the definition of the vector 2-norm yields

$$\| G \|_{i_2} = \sqrt{(u_1 \sigma_1)^H (u_1 \sigma_1)} = \sqrt{\sigma_1^2 (u_1^H u_1)} = \sqrt{\sigma_1^2 (1)} = \sigma_1 \tag{3.17}$$

Thus, the maximum singular value of G, σ_1, (corresponding to the maximum eigenvalue of

50

$G^H G$ or GG^H) equals the induced matrix 2-norm of G over C^n, which is also equal to the largest possible 2-norm of y since y equals G times u.

Replacing sup in (3.12) with inf (short for infimum, denoting a largest lower bound) also allows the minimum gain of G to be expressed in terms of its minimum singular value, σ_k, (corresponding to the smallest eigenvalue of $G^H G$ or GG^H).

Thus, in a fashion analogous to SISO systems, the effects of a transfer function matrix acting on an input vector at a given frequency can be characterized by a range of "principal gains" [7], bounded above and below by the maximum and minimum singular values of the transfer function matrix, respectively. Furthermore, the right singular vectors of matrix G correspond to input "directions" (combinations of elements of the input vector, u) which are simultaneously amplified or attenuated (as dictated by the associated singular value) and mapped by G to output directions governed by the left singular vectors. By analyzing the SVD of the transfer function matrix at all frequencies, the principal gains induced by certain combinations of inputs, and the resulting outputs, can thus be discovered. Due to this property, the singular values of a matrix, and in particular its maximum singular value, are the dominant quantities of interest in the analysis and design of LTI feedback systems.

Indeed, the performance goals discussed in Chapter 2 can be conveniently stated in terms of an allowable upper bound on the maximum singular value of a certain matrix transfer function, due to this induced vector 2-norm property. In Chapter 2, performance objectives were stated as maintaining the RMS or 2-norm value of the scaled error vector below one, despite the presence of broadband vibrational disturbance torques and measurement noise. By combining the two disturbances into a single disturbance vector

$$ d = \begin{bmatrix} d_T \\ \theta \end{bmatrix} $$

and scaling so that $\|d\|_2 \leq 1$, performance goals can be achieved by requiring the closed-loop transfer function from d to e, $T_{ed}(s)$, to have maximum singular value less than one at all frequencies where the disturbances act, or more conservatively, at all frequencies. The infinity-norm of a transfer function is defined as the maximum singular value of that transfer function over all frequencies, i.e.,

51

$$\|T(s)\|_\infty = \sup_\omega \sigma_1[T(j\omega)] \qquad (3.18)$$

and, therefore, performance requirements for the SBL example considered reduce to ensuring

$$\|T_{ed}(s)\|_\infty \le 1 \qquad (3.19)$$

for the appropriately scaled system with deterministic, bounded energy disturbances.

As mentioned in Section 2.3, the infinity-norm performance criterion of (3.19) applies equally for the system with assumed zero-mean, stationary stochastic disturbance inputs of bounded variance (standard deviation). To see this, consider the definition of the 2-norm squared (variance) of a stochastic vector signal e

$$\| e \|_2^2 = \sigma_e^2 = E\left(\int_0^\infty e(t)^T e(t)\, dt \right) = E\left(\frac{1}{2\pi} \int_{-\infty}^\infty e(j\omega)^H e(j\omega)\, d\omega \right) \qquad (3.20)$$

which is the same as the definition of the 2-norm squared of a deterministic vector signal given in Section 2.3, except for the addition of the expectation operator, E. Making use of the properties of the matrix trace operator, abbreviated tr, and the linearity of the expectation operator, (3.20) becomes

$$\sigma_e^2 = \frac{1}{2\pi} E \int_{-\infty}^\infty \mathrm{tr}\left(e(j\omega)e(j\omega)^H\right) d\omega \qquad (3.21)$$

Using the fact that $e = T_{ed}\, d$ (and dropping the frequency dependent notation for convenience), (3.21) can be written

$$\sigma_e^2 = \frac{1}{2\pi} E \int_{-\infty}^\infty \mathrm{tr}\left(T_{ed}d\,(T_{ed}d)^H\right) d\omega = \frac{1}{2\pi} E \int_{-\infty}^\infty \mathrm{tr}\left(T_{ed}dd^H T_{ed}{}^H\right) d\omega \qquad (3.22)$$

And, since $\mathrm{tr}\,(AB) = \mathrm{tr}\,(BA)$,

$$\sigma_e^2 = \frac{1}{2\pi} E \int_{-\infty}^{\infty} \operatorname{tr}\left(T_{ed}{}^H T_{ed}\, dd^H\right) d\omega$$

(3.23)

The next step in the derivation involves the following lemma, which is first stated then proven.

Lemma: $\operatorname{tr}(AB) \leq \sigma_1(A)\operatorname{tr}(B)$, given $A = A^H$

Proof: Since $A = A^H$, $A = U\,\Sigma\,U^H$ (utilizing the SVD of A)

then $\operatorname{tr}(AB) = \operatorname{tr}(U\,\Sigma\,U^H B)$

$= \operatorname{tr}(\Sigma\,U^H B\,U)$

$\leq \sigma_1(A)\operatorname{tr}(U^H B\,U)$

$\leq \sigma_1(A)\operatorname{tr}(B\,U\,U^H)$

$\leq \sigma_1(A)\operatorname{tr}(B)$, Q.E.D.

Now, since $T_{ed}{}^H T_{ed} = (T_{ed}{}^H T_{ed})^H$, the above lemma applies to (3.23), and using the definition of the infinity-norm (3.18), (3.23) can be written

$$\sigma_e^2 \leq \frac{1}{2\pi} E \int_{-\infty}^{\infty} \| T_{ed} \|_\infty^2 \operatorname{tr}\left(dd^H\right) d\omega$$

(3.24)

or

$$\sigma_e^2 \leq \| T_{ed} \|_\infty^2 \frac{1}{2\pi} E \int_{-\infty}^{\infty} \operatorname{tr}\left(dd^H\right) d\omega = \| T_{ed} \|_\infty^2 \sigma_d^2$$

(3.25)

From (3.25), it is obvious that if the disturbance variance is unity bounded, then the error variance will be unity bounded only if

$$\| T_{ed} \|_\infty \leq 1 \qquad \qquad (3.26)$$

and the same may be said for the input and output RMS values. Thus, the deterministic and stochastic optimal control problems result in an equivalent performance constraint on the infinity-norm of the closed-loop transfer function, as long as the disturbance and error variables are appropriately scaled (or alternatively, as long as the scaling on the disturbance and error vectors is interpreted correctly).

3.4.3 Open-Loop Singular Value Frequency Responses

In this thesis, we shall be primarily interested in three open-loop singular value frequency response curves. The first describes the transfer of the nominal plant from the controls, u, to the measured outputs, y. This transfer function is important because it portrays how the system actuators affect the outputs, giving some indication of how much we can hope to improve performance through feedback. The second open-loop transfer function of interest is that which relates the combined input and disturbance vectors to the scaled LOS and segment phasing performance variables. This transfer function will provide the basis for the model reduction techniques considered in Chapter 4. The third frequency response of interest is the open-loop transfer from the disturbance torques to the scaled performance variables. The frequency response of this transfer function yields open-loop performance in terms of rejection of the torque disturbances, upon which we hope to improve via feedback control. Figures 3.5, 3.6, and 3.7 show the singular value frequency response of these three transfer functions.
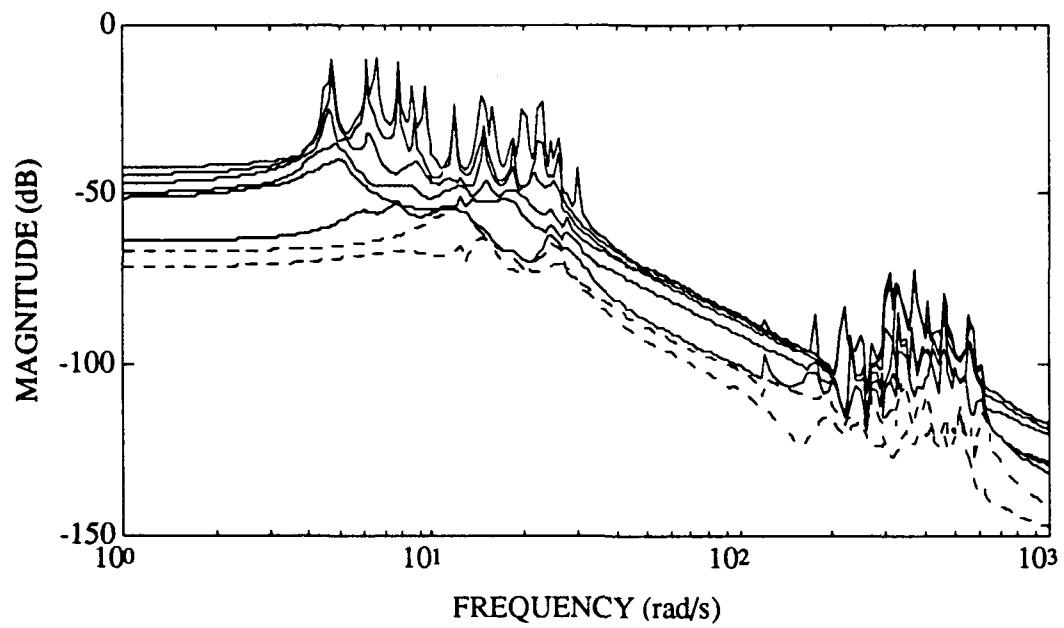
Figure 3.5 Open-Loop Singular Value Frequency Response from Controls to Outputs.
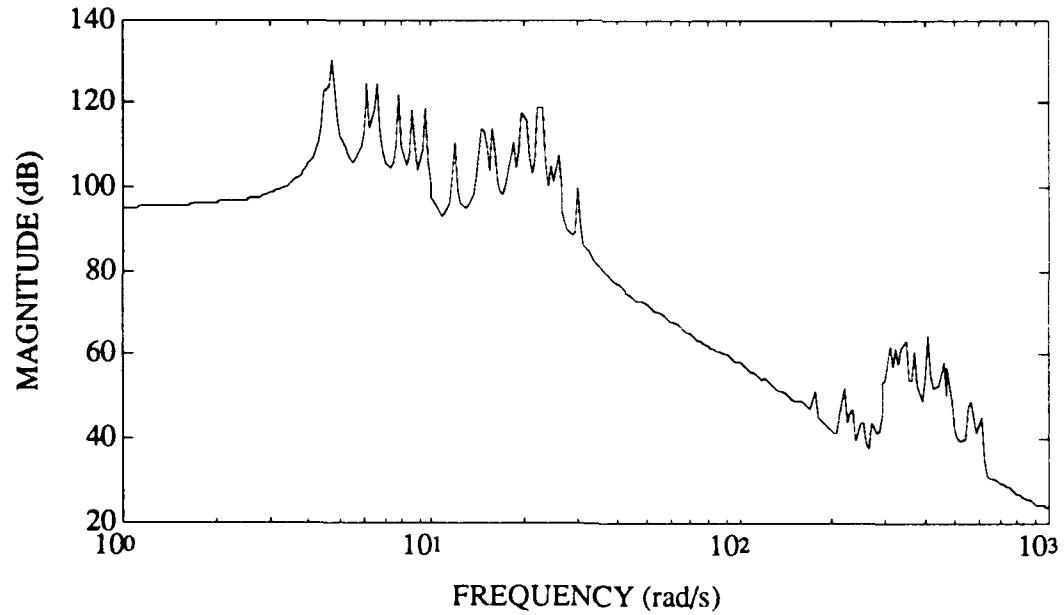
Figure 3.6 Open-Loop Max. Singular Value Frequency Response from
Combined Controls and Disturbance Torques to All Errors.
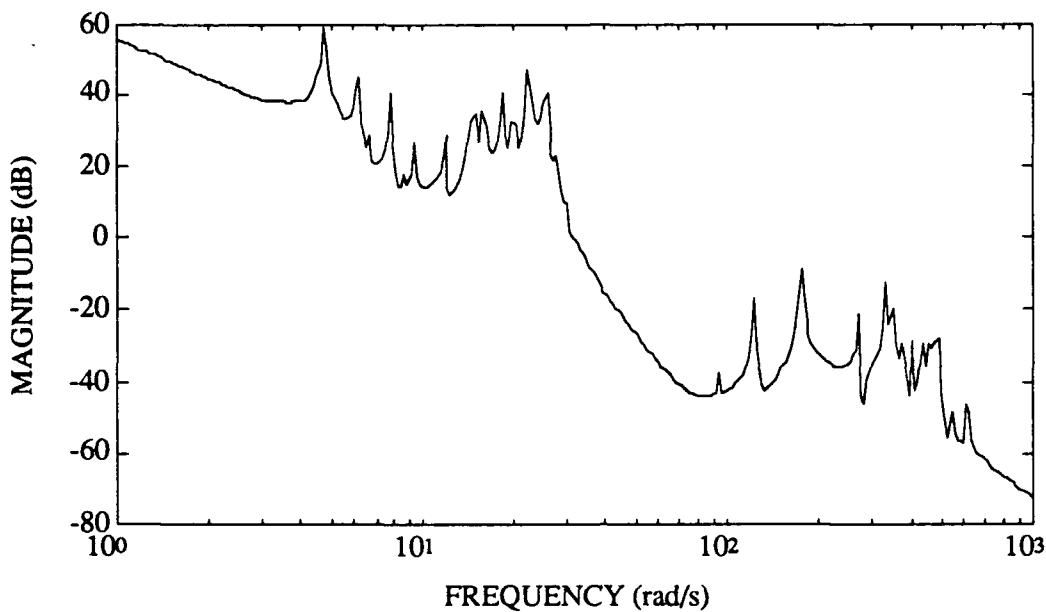
Figure 3.7 Open-Loop Max. Singular Value Frequency Response from
Disturbance Torques to All Errors.

The primary system characteristic displayed by the above plots is the separation of the open-loop dynamics into two groups of lightly-damped poles and zeros, as evidenced by the tightly grouped sequences of peaks and valleys seen in the figures. The first group, running from about 4.5 to 30 radians per second, corresponds to the structural dynamics of the primary mirror segment force reaction structures and the secondary mirror. The higher frequency second grouping, running from about 170 to 500 radians per second, represents the bending modes of the reaction structures and the graphite-epoxy support truss.

Two other features of the open-loop singular value frequency response plots are also noteworthy. Evident in the low-frequency region of Figure 3.7 is a 40 dB per decade roll-off induced by the rigid body modes of the entire BEA structure, while such a roll-off is clearly lacking in Figures 3.5 and 3.6. This suggests that the transfer from u to y and e is relatively unaffected by the rigid body modes, a fact that will be exploited later to simplify the design model. Also, from Figure 3.7 it can be seen that the open-loop performance transfer function displays disturbance amplification (maximum singular value greater than 0 dB) for all frequencies less than ~50 radians per second, and has a maximum singular value upper bound of 59.0 dB in the frequency range shown. To provide insight into how the

56

torque disturbances affect the segment phasing and LOS outputs individually, Figures 3.8 and 3.9 show the open-loop transfer maximum singular values from d_T to e_{sp} and e_{los}, respectively. The two groups of lightly damped poles and zeros are again displayed in the figures. Also, it can be seen that the open-loop transfer from the disturbance torques to the segment phasing errors is 10-15 dB greater than the transfer to the LOS errors.
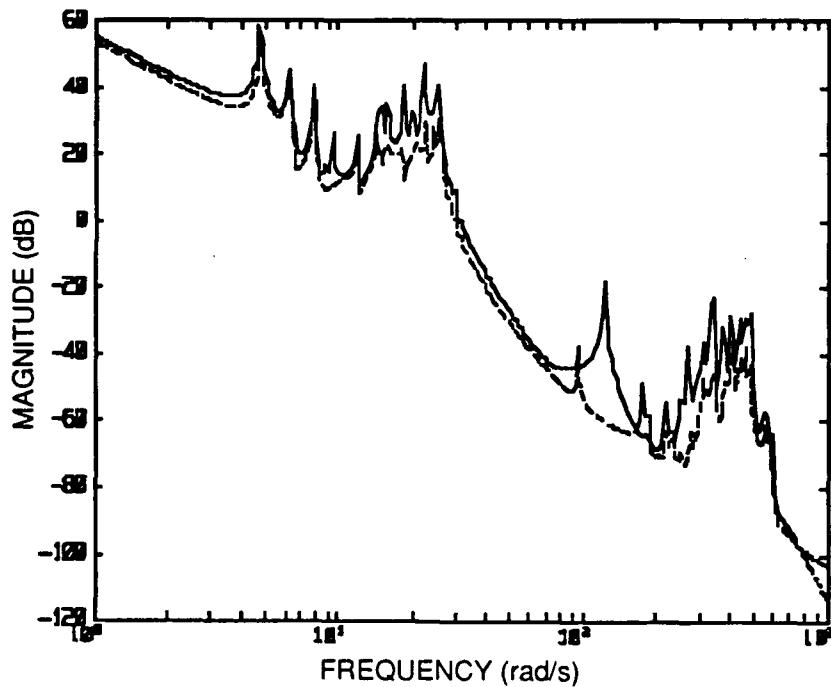
Figure 3.8 Open-Loop Transfer from Disturbance Torques to Segment Phasing Errors.
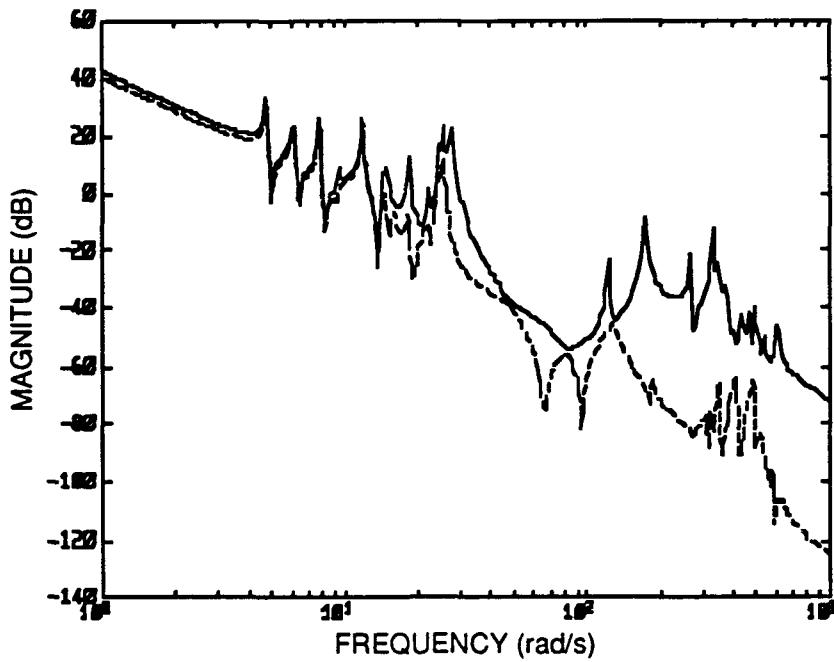
Figure 3.9 Open-Loop Transfer from Disturbance Torques to Line-of-Sight Errors.

In this section, several important characteristics of the open-loop model have been illustrated. The lightly damped nature of the system model, and the large number of near pole-zero cancellations so typical of large flexible structures has been observed. Additionally, Figures (3.7-3.9) illustrate the unsatisfactory nature of open-loop system performance, forming a baseline upon which the closed-loop system must improve. Figure 3.5 and the open-loop pole and zero plots provide insight into the complex nature and extreme dimensionality of the system model. Due to this high dimensionality, software and computation time limitations come into play, preventing compensator synthesis from proceeding directly. Instead, the open-loop system model must first be somehow reduced in size. This motivates the topic of model reduction, which is considered next in Chapter 4.

CHAPTER 4

Model Reduction

4.1 Introduction

As mentioned in Section 2.2, the full-order model (FOM) of the SBL BEA given by
(2.8), (2.9), and (2.14) is characterized by 390 states, 26 inputs (24 actuators and 2
disturbances), and 29 outputs (27 segment phasing and 2 LOS). Due to the numerical
difficulties and excessive computation times inherent in analysis and design with an FOM
of such large dimension, it is desirable to reduce the state-dimension of the system model,
while simultaneously preserving the relationships between inputs and outputs. Analysis
and design of feedback controllers can then be expediently carried out with the sufficiently
accurate reduced-order model (ROM), rather than with the cumbersome FOM.
Mathematical techniques for the reduction of model order are now considered. In Section
4.2, open-loop system controllability/observability issues are addressed via gramian-based
techniques. Coverage of this topic leads naturally to a survey of various model reduction
methods, which are discussed in Section 4.3. Finally, Section 4.4 illustrates application of
two selected model reduction techniques to the full-order BEA model, and presents
characteristics of the selected reduced-order open-loop system model.

4.2 Controllability/Observability Issues

The concepts of controllability and observability are of fundamental importance to
output feedback control of LTI systems like the BEA model of (3.1). A state-space
realization pair (A,B) like that of (3.1) is said to be completely controllable if and only if it
can be transferred from the zero state at any initial time t_0 to any terminal state $x(t_f) = x_f$

within a finite time $t_f - t_0$ [9]. It can be shown via linear systems theory [14] that for stable systems, an explicit test for system controllability is to verify that the controllability gramian, P, defined by

$$P = \int_{t_0}^{t_f} e^{At} B B^T e^{A^T t} dt$$

(4.1)

is non-singular.

Similarly, a state-space realization pair (A,C) like that of (3.1) is said to be completely observable if, given measurements at some time $y(t_f)$, the state of the system at $t_0 < t_f$ can be uniquely reconstructed [9]. Non-singularity of the observability gramian,

$$Q = \int_{t_0}^{t_f} e^{A^T t} C^T C e^{At} dt$$

(4.2)

is necessary and sufficient to guarantee system observability for stable systems [14].

A state-space realization of an LTI system that is both completely controllable and observable is said to be minimal. Minimality of the open-loop plant is required for the state-space control system design algorithms considered in Chapter 5, and was also necessary for the MIMO transmission zero identification algorithm discussed in Section 3.3. Furthermore, the degree of controllability/observability of an individual system state is directly proportional to the magnitude of that state's effect on system singular value frequency response. Quantifying the controllability/observability of individual system states provides an efficient basis for model reduction, as will be seen in the next section.

4.3 Survey of Model Reduction Techniques

A thorough and systematic treatment of reduced-order model development was published by Moore [15]. The technique proposed by Moore, which is often called balance and truncate (B&T), uses the state-space representation (A,B,C) of the plant that describes the relationship between the input, states, and measurements in which the steady-state controllability and observability gramians (note the particular choices for t_0 and t_f)

60

$$P = \int_0^\infty e^{At} B B^T e^{A^T t} dt$$

$$Q = \int_0^\infty e^{A^T t} C^T C e^{At} dt \tag{4.3}$$

are diagonal and equal. The diagonal elements of the gramians, referred to as the Hankel singular values (HSVs) [16], provide the basis for model reduction. Large HSVs correspond to states that are easily controlled and observed, while small HSVs define states that are difficult to control and observe. Thus, the state-space model can be partitioned into strongly and weakly controllable/observable states, and the subspace of weakly controllable/observable states may be deleted. Controllability and observability therefore play equal roles in determining which individual states will be retained in the B&T ROM, and as long as the HSV of the last state retained is nonzero, the B&T ROM is guaranteed to be both controllable and observable. Extensions of Moore's B&T method are made in [17], wherein computational methods independent of plant minimality are developed, and in [16] the approximation error is bounded in terms of the Hankel singular values.

A more formal approach to model reduction is taken in [16], wherein the optimal reduced-order model of fixed dimension is sought which minimizes the Hankel-norm (*i.e.,* the maximum HSV) of the approximation error. The solution to the Hankel-norm model reduction problem is significantly more complex than that of B&T; however, it may provide significantly superior results.

The two methods mentioned above allow characterization of the absolute modeling error bounds in the ROM. An alternative that provides a relative error bound is the so-called balanced stochastic truncation (BST) method discussed in [18]. The positive aspect of this technique is that it provides a more meaningful error criteria for model reduction. However, its weak point is that it is only applicable to square plants, and therefore, its use is somewhat limited.

All of the model reduction techniques discussed above are applicable to open-loop stable plants only. In [19] a generalization of B&T called the fractional balanced reduction (FBR) method is described that can be applied to open-loop unstable plants. Combining

this technique with the methods presented in [18] for addressing nonminimal plants offers the direct capability for performing model reduction on arbitrary plants.

Since the finite element model is originally derived in modal form, the technique of modal truncation (MT) can be applied directly to (2.4) to reduce the order of the system model prior to obtaining a state-space realization. This is accomplished by simply eliminating very high natural frequency modes from the system $\eta(t)$ vector, truncating corresponding columns and rows from the Ω matrix, and deleting corresponding rows of the $\Phi^T B$ matrix products. However, the reduced order model one obtains by doing this has no guaranteed properties with regard to controllability/observability.

Due to computational requirements, application of model reduction to the 26-input, 29-output, 390-state SBL model described in Section 2 requires a prudent choice of model reduction techniques. Since the SBL BEA model is open-loop stable due to the light damping of all structural modes, any of the above methods except BST may be used (since the open-loop plant is not square). However, FBR is not a wise choice, because the technique is a computationally costly generalization of B&T for unstable systems. B&T is attractive because infinity-norm error bounds for all ROM orders are computed by calculating the full-order plant's controllability and observability gramians once, and reduced-order models of any order are subsequently obtained by simple matrix multiplications of elements taken from the gramians' singular value decompositions. Although superior ROMs may be obtained by Hankel-norm minimization, the method is substantially more computationally intensive than B&T and requires all computations to be performed for each order ROM desired. Finally, the last technique discussed, modal truncation, is attractive due to its ease of application, but may not produce a minimal model.

4.4 Application of Model Reduction Techniques

In light of the above issues, a trade study using only the modal truncation and B&T techniques was conducted in order to obtain a suitable ROM for the jitter and segment phasing control system . In Figure 4.1, a plot of additive modeling error theoretical upper bounds versus ROM order, as measured by the infinity-norm, is given for the B&T method. A significant knee in this plot is seen at order 12 where all six rigid body modes (describing rotation and translation of the entire BEA) are included in the ROM, and another pronounced knee is found for a ROM of 34 modes (68 states).
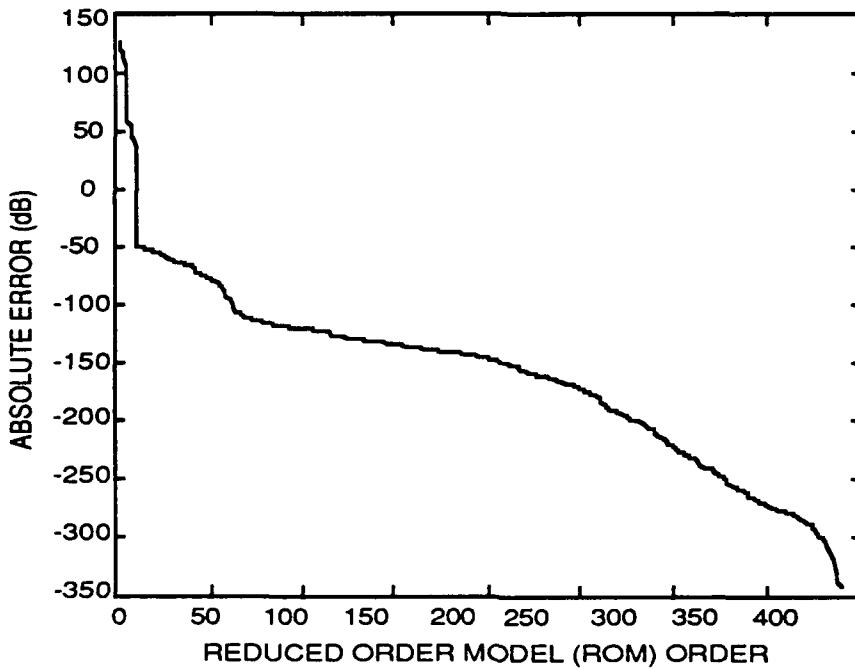
Figure 4.1 B&T ROM Additive Error.Upper Bounds.

In balancing the full-order (390-state) system model via Moore's algorithm, machine precision resulted in truncation of the state dimension to 120 states. Therefore, the 120-state B&T ROM was judged to be sufficiently accurate to represent the full-order model, and it was adopted as the "truth" model for the open-loop system. Based on this fact and the information in Figure 4.1, reduced-order models were derived for a finite number of ROM dimensions ranging from 56 to 100 using both B&T and MT methods, and the infinity-norm of the actual additive error due to model reduction

$$\| G - G_k \|_\infty = \overset{sup}{_\omega} \ C_e (j\omega I - A_e)^{-1} B_e$$

(4.4)

where

G = the open-loop plant truth (120-state B&T) model, represented by (A, B, C)

G_k = a kth order ROM approximation to G, represented by (A$_k$, B$_k$, C$_k$)

63

$$A_e = \begin{bmatrix} A & 0 \\ 0 & A_k \end{bmatrix}$$

$$B_e = \begin{bmatrix} B \\ B_k \end{bmatrix}$$

$$C_e = \begin{bmatrix} C & -C_k \end{bmatrix}$$

was then computed. A plot of these actual error infinity-norms versus ROM order is plotted in Figure 4.2, along with the bounding data from Figure 4.1.
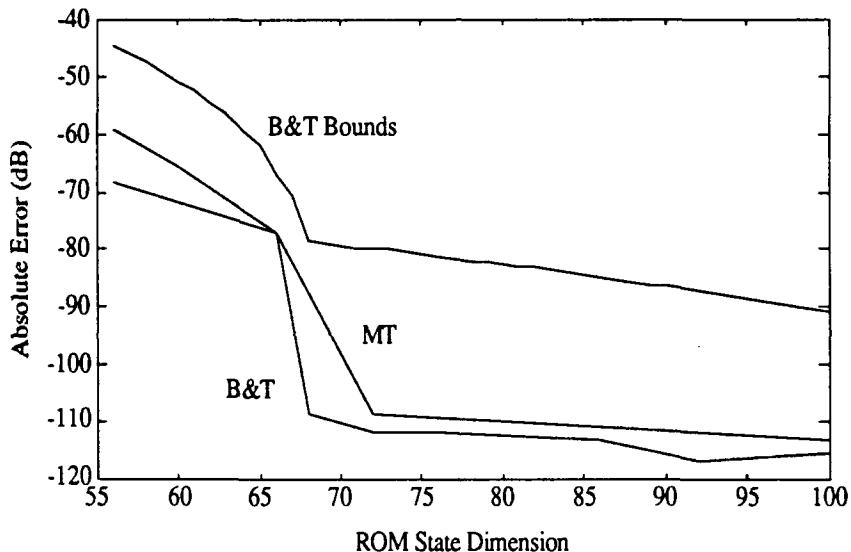
Figure 4.2 Infinity Norms of Computed Additive Errors vs ROM Order.

As can be seen from the figure, the B&T method produces consistently smaller additive error infinity-norms than the MT method. Also, since the B&T reduced-order model is guaranteed minimal (as long as the HSV of the last retained mode is greater than zero), the B&T technique produces the ROM of choice. Figure 4.2 indicates a significant decrease (35 dB) in additive error infinity-norm when going from a 66 to a 68-state ROM, while the error curve remains basically flat for ROM orders beyond that point. This suggests employing a 68-state ROM for analysis and design purposes. To ensure that the 68-state ROM is minimal, the HSVs of the FOM should be checked. A plot of Hankel Singular Values versus state dimension appears in Figure 4.3. As can be seen from the figure, the

64

HSVs remain fairly constant in magnitude up through the 68-state level, after which the HSV curve drops sharply off. This indicates that states beyond the 68th state are considerably less controllable/observable than the 68th state, and can be truncated without severely degrading the input/output properties of the ROM. Also, since the 68th state HSV is greater than zero, the 68-state ROM is guaranteed to be minimal as desired.
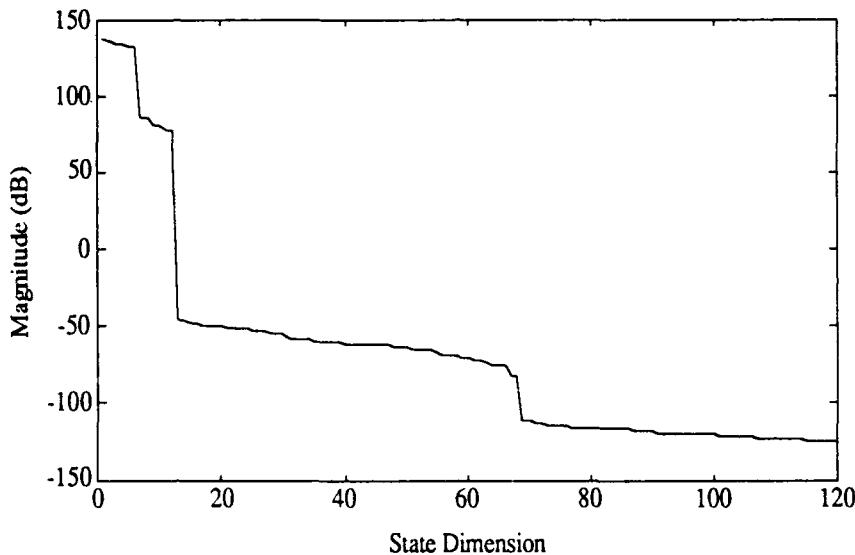
Figure 4.3 Hankel Singular Values vs BEA Model State Dimension.

Recalling that the input for this model reduction study consisted of the combined actuators and torque disturbances, it was believed prudent to check on the controllability properties of the 68-state ROM from each input separately. Also, since the HSVs combine the effects of controllability and observability, it was deemed of interest to investigate observability of the ROM separate of controllability. Examination of these individual steady state controllability and observability gramians reveals that while the six rigid body modes are very observable in the system outputs, they are almost totally uncontrollable from the system inputs (segment position actuators). They are, however, strongly excitable from the torque disturbances, and this combined with their high level of observability is enough to yield the large HSVs attributed to the rigid body modes in Figure 4.3. For purposes of control, though, the rigid body modes remain unaffectable by the segment position actuators. Since satellite attitude contro' and propulsion systems exist to regulate the rigid body motion of the BEA, uncontrollability from the system actuators does not present any problem, and the rigid body modes can be removed from the beam

65

jitter/segment phasing system model. Doing so results in a 56-state ROM of the SBL BEA for control system design purposes. The maximum singular value frequency response plots for the FOM (combined actuator and disturbance inputs) and ROM with the 12 rigid body states removed appears in Figure 4.4. As is evident, application of the B&T method gives a RCM that includes the important low frequency structural modes, while neglecting the much higher frequency bending mode dynamics. Also evident is the removal of the BEA rigid body modes, as there is not now 40 dB per decade roll-off in the low-frequency region (compare with Figures 3.7-3.9).
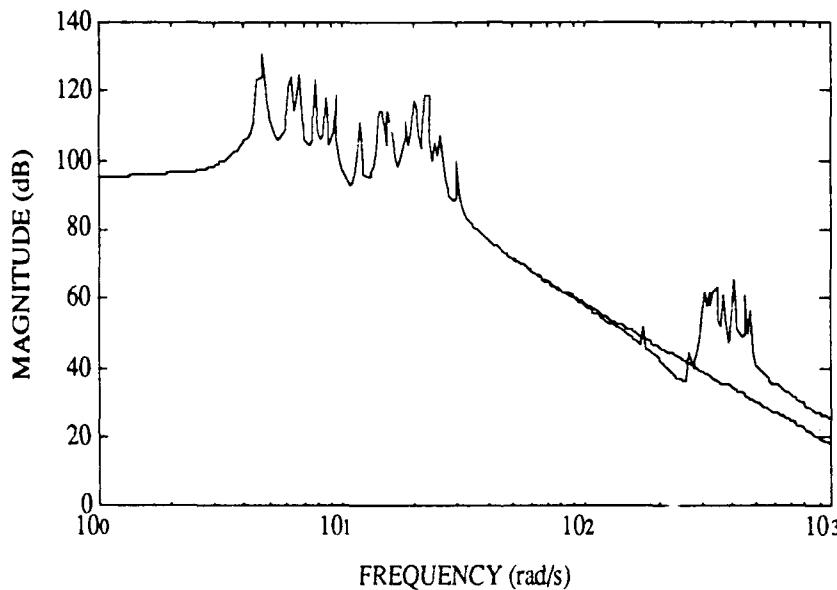
Figure 4.4 Full-Order and 56-State Reduced Order Model
Maximum Singular Values from $\tilde{u}$ to e
(Rigid Body Dynamics Removed).

Figures 4.5-4.7 below show complex plane plots of the open-loop poles and MIMO transmission zeros for the 56-state, 8-output BEA model that is used for control system design in Chapters 6 and 7. Figure 4.5 verifies that the high-frequency bending mode dynamics of the BEA have been truncated in the 56-state ROM, while the low-frequency structural modes have been preserved. Also note that the highest natural frequency retained in the 56-state design model is on the order of 30 radians per second. Figures 4.6 and 4.7 indicate that reducing the model order from 120 to 56 via the B&T method eliminates many

66

of the high-frequency zeros seen in Figure 3.3, but preserves the pattern of low-frequency zeros observed in the truth model.
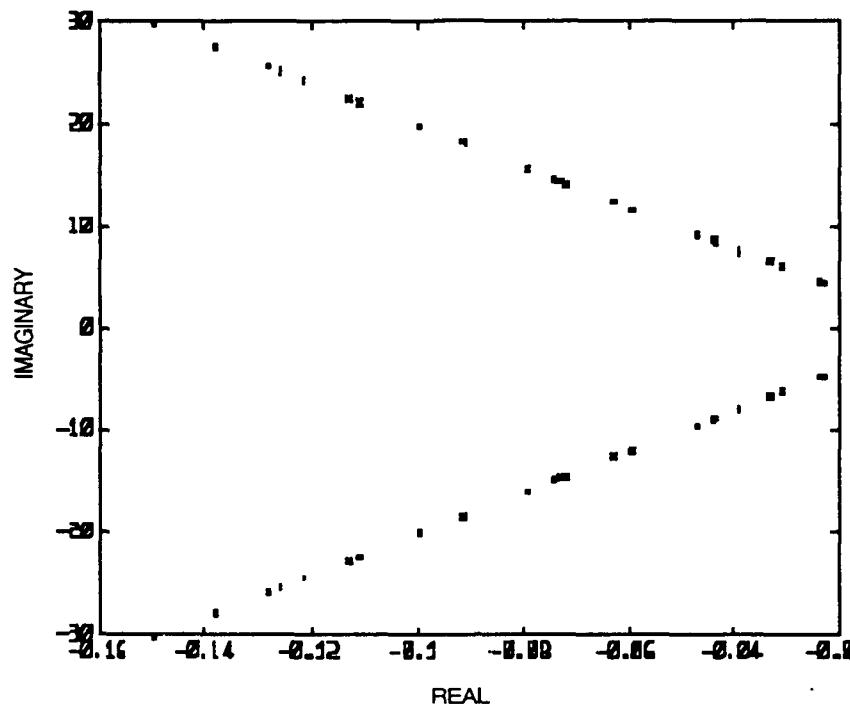
Figure 4.5 Open-Loop Pole Plot (56-State Model).

67
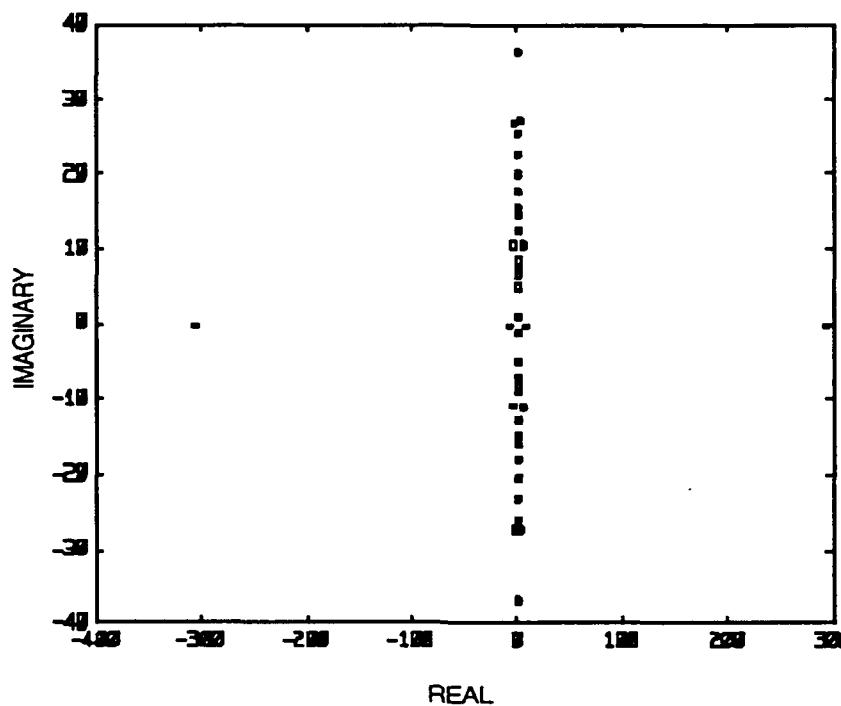
Figure 4.6 Open-Loop Multivariable Transmission Zeros (56-State Model).
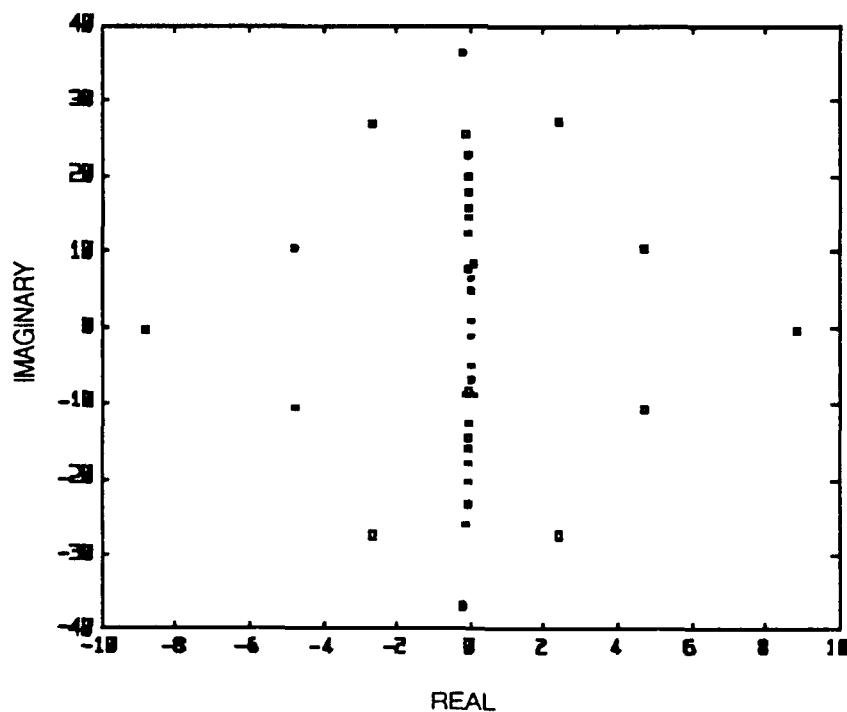
Figure 4.7 Open-Loop Multivariable Transmission Zeros
(56-State Model, Close-up About the Origin).

68

CHAPTER 5

A Methodology for Robust Control System Synthesis

5.1 Introduction

This chapter presents a methodology for robust control system design for the SBL BEA employing the reduced-order model of Chapter 4. Section 5.2 formulates a framework for robust control system design in which stability robustness constraints and performance objectives can be met by bounding the infinity-norms of two closed-loop transfer functions. The Small Gain Theorem is introduced as the tool for verifying stability robustness, while compensator design can be accomplished utilizing various methods. Section 5.3 addresses several candidate synthesis techniques: H_2 optimal control, H_∞ optimal control, and H_2/H_∞ loop-shaping design techniques, and all necessary conditions and equations for compensator design are presented.

5.2 Stability Robustness via the Small Gain Theorem

Model reduction introduces errors into the design process that must be accounted for in system stability and performance analysis, and, hence, robust control techniques that ensure both stability and performance in the presence of modeling errors are required. Analysis with the well-known Small Gain Theorem (SGT) [7] in combination with an appropriate controller design technique such as H_2 or H_∞ provides a framework for robust control design, by allowing both performance requirements and stability robustness

constraints to be simply posed in terms of bounds on infinity-norms of certain transfer functions. For the system depicted in Figure 5.1, the Small Gain Theorem states that the nominally stable plant M(s) is stable for all stable perturbations Δ(s) if $\|M(s)\|_\infty\|\Delta(s)\|_\infty \leq 1$ (i.e., the loop gain is small).
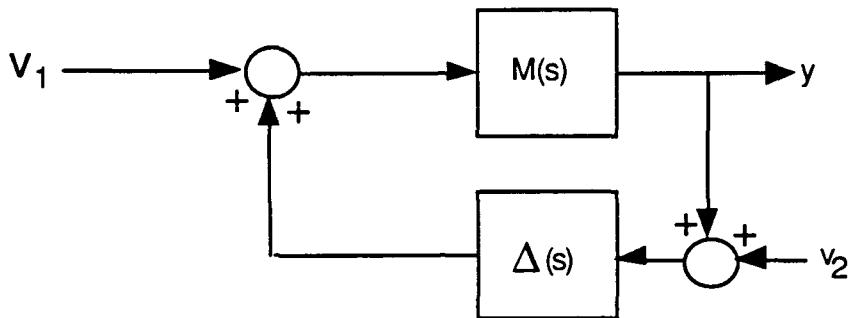
Figure 5.1 Topology for the Small Gain Theorem.

Note that the robustness criterion stated depends only on the magnitude of the closed-loop transfer, and not on any information related to system phase characteristics. Therefore, the Small Gain Theorem requires that system errors or uncertainties be bounded above in a magnitude sense only. This condition greatly simplifies modeling of system uncertainties, but it also creates conservatism in the assessment of system robustness.

Consider Figure 5.2, where G(s) represents the open-loop plant ROM transfer matrix, Δ_M(s) is the multiplicative error at the plant output due to model reduction, u represents the actuator commands, and y is the measured LOS and segment phasing error. Further, assume without loss of generality that $\|\Delta_M(s)\|_\infty \leq 1$.[4] The block diagram of Figure 5.2 can be augmented to include disturbance and performance signals, d and e respectively, as shown in Figure 5.3, where it is assumed that the disturbance is bounded by unity (i.e., $\|d\|_2 \leq 1$) and nominal performance specifications are met if $\|e\|_2 \leq 1$ (as discussed in Sections 2.3 and 3.4).

---

[4] Scaling of Δ_m is easily incorporated into the plant by augmenting frequency dependent weighting functions to the system matrices.

70
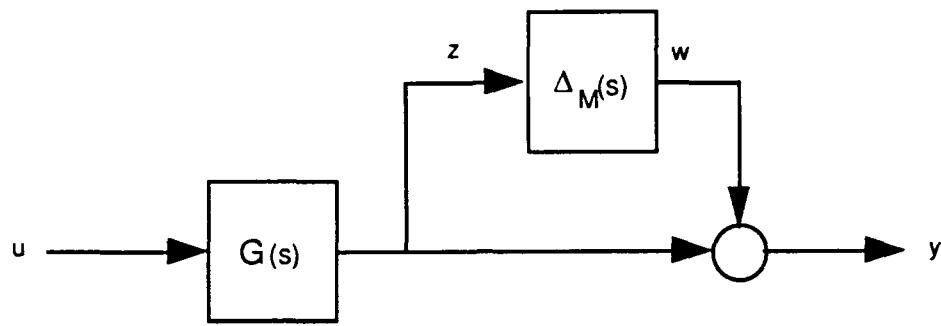
Figure 5.2 ROM with Multiplicative Modeling Error.
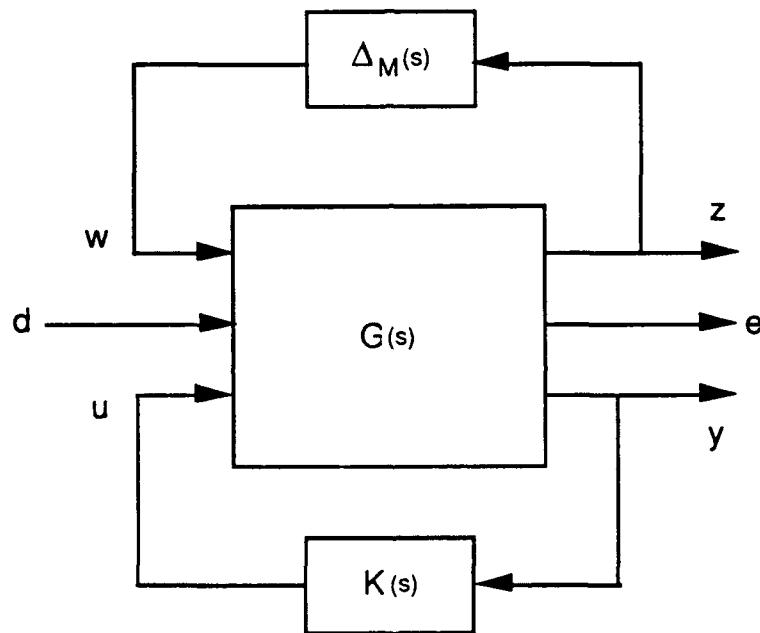
Figure 5.3 Augmented Plant (3-Block Form).

The nominal 3-block open-loop system of Figure 5.3, G(s), can then be represented by the state-space realization

$$\dot{x}(t) = A\,x(t) + B_1\,w(t) + B_2\,d(t) + B_3\,u(t)$$

$$z(t) = C_1\,x(t) + D_{11}\,w(t) + D_{12}\,d(t) + D_{13}\,u(t)$$

$$e(t) = C_2\,x(t) + D_{21}\,w(t) + D_{22}\,d(t) + D_{23}\,u(t)$$

71

$$y(t) = C_3\,x(t) + D_{31}\,w(t) + D_{32}\,d(t) + D_{33}\,u(t) \tag{5.1}$$

or, more compactly,

$$G(s) = \left[\begin{array}{c|ccc} A & B_1 & B_2 & B_3 \\ \hline C_1 & D_{11} & D_{12} & D_{13} \\ C_2 & D_{21} & D_{22} & D_{23} \\ C_3 & D_{31} & D_{32} & D_{33} \end{array}\right]$$

Since the infinity-norm is the operator norm that relates 2-norm bounded inputs to 2-norm bounded outputs (or RMS of input to RMS of output), an H_∞ performance optimization problem may be constructed to minimize the infinity-norm of the closed-loop transfer from d to e, and if this quantity can be made less than or equal to one (implying nominal performance specifications are met), then stability robustness may be ensured via the SGT by verifying that $\|M(s)\|_\infty \|\Delta(s)\|_\infty \leq 1$. This may be restated more clearly by considering Figure 5.4, which illustrates the closed-loop transfer function from w and d to z and e, obtained from substituting u = Ky into (5.1).
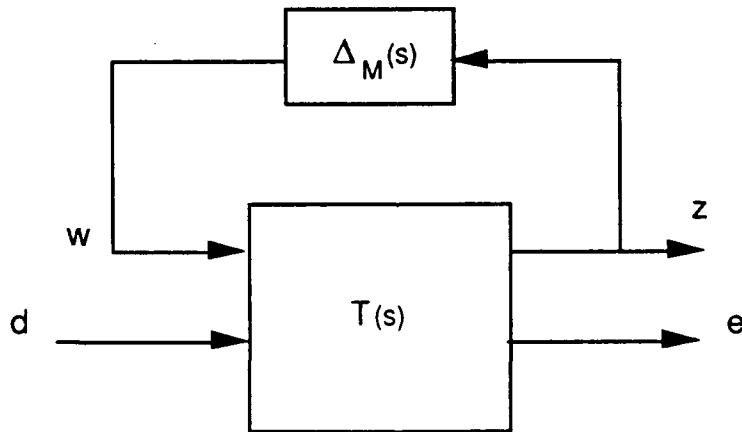
Figure 5.4 Closed-Loop Transfer Function.

The closed-loop transfer function, T(s), can be partitioned such that

$$\begin{bmatrix} z \\ e \end{bmatrix} = \begin{bmatrix} T_{11}(s) & T_{12}(s) \\ T_{21}(s) & T_{22}(s) \end{bmatrix} \begin{bmatrix} w \\ d \end{bmatrix}$$

and, in the context of the framework discussed above, nominal system performance specifications are then met as long as

$$\|T_{22}(s)\|_\infty \leq 1$$

and stability robustness is ensured if

$$\|T_{11}(s)\|_\infty \leq 1$$

Note that the framework for robust control system design presented in this section addresses only stability robustness issues, and allows no general provisions for testing the robustness of performance. Performance robustness, or the guaranteeing of system performance in the presence of uncertainty, is not specifically designed for in this thesis. Performance robustness of the final design selected is, however, independently assessed in Chapter 8, for certain known types of system errors.

Output feedback controller synthesis techniques suitable for use in conjunction with the stability robustness test of the Small Gain Theorem are now addressed.

5.3   Compensator Design Techniques

5.3.1   Introduction

Three multivariable feedback design methodologies suitable for use in the framework of Section 5.2 are now considered: H_2 optimal control, H_∞ optimal control, and H_2/H_∞ loop-shaping techniques. Multivariable feedback design is conveniently discussed in terms of Figure 5.3 and its associated state-space realization (5.1). Also, certain assumptions regarding the structure of (5.1) allow formulation of the various controllers to be greatly simplified. The following conditions on the matrices of (5.1) are assumed to hold in the succeeding discussion of compensator designs:

1) $D_{22} = 0$

2) $D_{33} = 0$

3) $D_{23}^T [C_2 \quad D_{23}] = \begin{bmatrix} 0 & \rho^2 I \end{bmatrix}$

73

$$4) \quad B_2 D_{32}{}^T = 0$$

where ρ is a scalar.

Assumption 1 simply states that there is no direct feed-through of the disturbance to the error which we are trying to minimize so that $\|T_{22}(s)\|_2$ is finite, while assumption 2 indicates that the open-loop plant is strictly proper. Assumption 3 implies that D_{23} and C_2 are orthogonal, so that the error vector includes a non-singular penalty on u that is linearly independent of the penalty on the state variables. The constant penalty on all the controls guarantees that D_{23} is of full column rank, and prevents the solution from requiring infinite control effort. Finally, assumption 4 is a consequence of lumping both process and measurement noise into the disturbance vector, and assuming they act independently on the state dynamics and measurements, respectively. The above assumptions are fairly standard in conventional H_2 control theory, and will be seen to be non-restrictive in the H_∞ case.

5.3.2 H_2 Optimal Control

In the above context, H_2 optimal control is a design methodology for selecting an output feedback compensator which minimizes the 2-norm of the closed-loop transfer function from d to e. The H_2 problem can thus be posed as the determination of a dynamic compensator $K(s)$ such that

$$K(s) = \inf_K \|T_{22}(s)\|_2 = \inf_K \left(\frac{1}{\pi} \int_0^\infty \text{trace} \left[T_{22}(j\omega)^H \, T_{22}(j\omega) \right] d\omega \right)^{\frac{1}{2}} \tag{5.2}$$

The H_2 problem is equivalent to a Linear-Quadratic Gaussian (LQG) design problem with cost function

$$J = \lim_{T \to \infty} E \int_0^T e(t)^T e(t) \, dt \tag{5.3}$$

where E is the expectation operator, the T inside the integral represents the transpose

74

operator, and the disturbances are all assumed to be uncorrelated, stationary, zero mean white Gaussian noise processes with unit intensities.

As per the LQG separation principle, by solving two independent matrix algebraic Riccati equations (AREs):

Full-State Feedback ARE

$$A^T P + PA - PB_3(D_{23}{}^T D_{23})^{-1} B_3{}^T P + C_2{}^T C_2 = 0 \qquad (5.4)$$

Kalman Filter ARE

$$\Sigma A^T + A\Sigma - \Sigma C_3^T(D_{32}{}^T D_{32})^{-1} C_3 \Sigma + B_2 B_2{}^T = 0 \qquad (5.5)$$

and computing the LQ and Kalman gains, respectively

$$K_{lq} = (D_{23}{}^T D_{23})^{-1} B_3{}^T P$$

$$K_f = \Sigma C_3^T(D_{32}{}^T D_{32})^{-1}$$

the H_2 optimal controller is obtained in the form of a model-based compensator

$$K(s) = -K_{lq}(sI - A + K_f C_3 + B_3 K_{lq})^{-1} K_f \qquad (5.6)$$

or

$$K(s) = \left[\begin{array}{c|c} A - K_f C_3 - B_3 K_{lq} & K_f \\ \hline -K_{lq} & 0 \end{array} \right]$$

which has dimension equal to the order of the plant due to the model-based nature of the compensator.

Unique positive-semidefinite solutions to (5.4) and (5.5) exist and provide guaranteed closed-loop nominal stability as long as (5.1) is both stabilizable and detectable, meaning that any uncontrollable/unobservable states are asymptotically stable [7]. This implies that

75

the open-loop plant should be represented by a minimal state-space realization prior to design via H_2 optimal control.

5.3.3 H_∞ Optimal Control

As its name implies, H_∞ optimal control is a methodology for selecting a feedback compensator which minimizes the infinity-norm of the closed-loop transfer function from d to e. The H_∞ problem can thus be posed as the determination of a dynamic compensator $K(s)$ such that

$$K(s) = \inf_K \|T_{22}(s)\|_\infty = \inf_K \sup_\omega \sigma_1(T_{22}(j\omega)) \tag{5.7}$$

A two-Riccati equation state-space algorithm described in [20] provides an efficient solution to the H_∞ optimization problem, which is commonly referred to as γ-iteration. In this procedure, γ represents an upper bound on the infinity-norm of the closed-loop transfer from d to e, which, as discussed in Sections 2.3, 3.4, and 5.1, must be less than or equal to one in order to achieve the specified performance objectives. In order to ascertain what closed-loop infinity-norm is attainable, a starting value of γ is assumed; it is then attempted to solve the H_∞ Riccati equations:

State-Feedback ARE

$$X_\infty A + A^T X_\infty - X_\infty Q X_\infty + C_2^T C_2 = 0 \qquad X_\infty \geq 0 \tag{5.8}$$

where

$$Q = B_3 \left(D_{23}^T D_{23}\right)^{-1} B_3^T - \frac{1}{\gamma^2} B_2 B_2^T$$

Output Injection ARE

$$Y_\infty A^T + A Y_\infty - Y_\infty R Y_\infty + B_2 B_2^T = 0 \qquad Y_\infty \geq 0 \tag{5.9}$$

where

$$R = C_3^T(D_{32}D_{32}^T)^{-1}C_3 - \frac{1}{\gamma^2}C_2^TC_2$$

and acceptance of the assumed γ value is conditional upon the two Riccati equation solutions being stabilizing, as per the following conditions:

1) $A - QX_\infty$ is stable

2) $A - Y_\infty R$ is stable

3) $\rho(X_\infty Y_\infty) < \gamma^2$

(5.10)

where $\rho(.)$ represents the spectral radius of the indicated matrix. Given a minimal system realization, if a stabilizing solution for the assumed value of γ cannot be obtained, then the assumed γ value is too small, and no stabilizing compensator can achieve that level of performance; γ must then be increased. If a stabilizing solution can be obtained, however, the assumed level of performance can be met. Since the idea is to make γ as small as possible (≤ 1), a smaller value of γ is then assumed, and the process is repeated until some set tolerance on the change in γ values is achieved. At this point, it is assumed that the upper bound on attainable closed-loop d to e transfer infinity-norm provided by γ closely approximates actual achievable performance, and the H_∞ optimal compensator is represented as

$$K(s) = \left[\begin{array}{c|c} \widehat{A}_k & \widehat{B}_k \\ \hline \widehat{C}_k & 0 \end{array} \right]$$

(5.11)

where

$$\widehat{A}_k = A - B_3(D_{23}^TD_{23})^{-1}B_3^T X_\infty Z - Y_\infty\left[C_3^T(D_{32}D_{32}^T)^{-1}C_3 - \frac{1}{\gamma^2}C_2^TC_2 \right]$$

$$\widehat{B}_k = Y_\infty C_3^T(D_{32}D_{32}^T)^{-1}$$

$$\widehat{C}_k = -(D_{23}^TD_{23})^{-1}B_3^T X_\infty Z$$

$$Z = \left(I - \frac{1}{\gamma^2} Y_\infty X_\infty\right)^{-1}$$

Note that like the H_2 optimal compensator, the generally non-unique H_∞ optimal compensator has dimension equal to the dimension of the plant.

Comparison of (5.6-5.9) indicates that the H_∞ Riccati equations reduce to the H_2 Riccati equations when γ is chosen to equal infinity. Thus, H_2 design can be thought of as H_∞ design with the particular choice of infinity for γ. Recalling that γ only represents an upper bound on the infinity-norm of the closed-loop transfer from d to e, however, it should not be assumed that the H_2 closed-loop transfer infinity-norm will be infinite. However, the actual H_2 closed-loop transfer infinity-norm from d to e can be computed and used as an initial guess for γ in the H_∞ design process. If success is obtained in reducing γ from this level, better worst-case performance (smaller d to e infinity-norm) results from the H_∞ design than from the H_2 design.

5.3.4 Loop-Shaping Techniques

In an intuitive sense, the H_∞ design process can be thought of as a tool for manipulating the peak value of the closed-loop transfer function from d to e. This suggests that by altering where the peak value of the open-loop transfer function occurs, we can dictate a particular frequency range in which we want the H_∞ design to focus its efforts. Similarly, the H_2 design process can be interpreted as trying to simultaneously push down all the maximum singular values of the T_{22} block, providing the ability to affect the entire closed-loop transfer. Thus, by augmenting the open-loop dynamics with frequency dependent weighting functions, H_∞ and H_2 optimal control provide a means of effectively shaping the frequency response of the transfer function of interest. Consider Figure 5.5, which illustrates the two-block open-loop design plant augmented with frequency dependent weighting functions on the system error and control vectors.
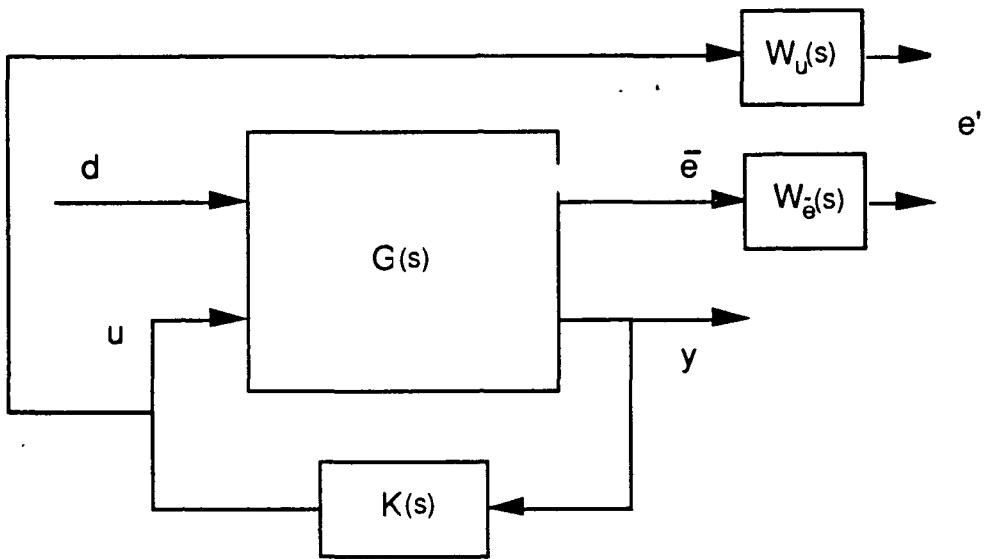
Figure 5.5 Weighted Open-Loop 2-Block Model.

The H_p optimization problem (where p represents either the 2-norm or infinity-norm) is now posed as the determination of a dynamic compensator K(s) such that

$$K(s) = \frac{\inf}{K} \|T_{e'd}(s)\|_p = \frac{\inf}{K} \left| \begin{array}{c} W_{\bar{e}}(s)\, T_{\bar{e}\,d}(s) \\ W_u(s)\, T_{ud}(s) \end{array} \right|_p \qquad (5.12)$$

where

$$\bar{e} = \left[\begin{array}{c} e_{sp} \\ e_{los} \end{array} \right]$$

Note that due to the additional states augmented onto the plant to represent the shaping-filter dynamics, loop-shaped compensators are invariably of higher order than the original plant. It is hoped that the extra dimensionality afforded the compensator by this process can be taken advantage of to achieve superior performance.

Now, to facilitate discussion, consider only the control portion of the performance criterion in an H_∞ optimization problem. With proper scaling performed, assume the design objective is posed as

79

$$\| W_u(s) \, T_{ud}(s) \|_\infty \le 1 \tag{5.13}$$

Equation (5.13), due to the sub-multiplicative property of the infinity-norm, can be rewritten

$$\| W_u(s) \|_\infty \, \| T_{ud}(s) \|_\infty \le 1 \tag{5.14}$$

or

$$\| T_{ud}(s) \|_\infty \le \frac{1}{\| W_u(s) \|_\infty} \tag{5.15}$$

Thus, $T_{ud}(s)$ can be made small in the frequency range of interest by choosing the weighting function $W_u(s)$ to be large enough in that frequency range (so that this is where the peak value of the closed-loop transfer occurs). The same argument of course applies to the segment phasing and LOS portions of the error. A similar argument applies to the H_2 optimization problem, except (5.14) and (5.15) cannot be explicitly written for the 2-norm. However, because the H_2 optimization problem works with all the maximum singular values of the closed-loop transfer instead of just the peak value, H_2 loop-shaping techniques sometimes allow easier manipulation of the overall frequency response. Further illustration of loop-shaping techniques is best provided by application to the SBL BEA ROM example, the details of which are discussed in Section 7.4. .

CHAPTER 6

The Design Plant Model

6.1 Introduction

The framework for robust control system design discussed in Sections 5.1 and 5.2 assumes a state-space realization (5.1) is available for the open-loop 3-block system model of Figure 5.3. The framework further assumes that the disturbance and error vectors are unity bounded in a 2-norm sense. As discussed in Chapter 2, the BEA system model developed so far is of the 2-block form seen in Figure 6.1, which represents the open-loop transfer from the vibrational torque disturbances and actuators to the measured and penalized LOS and segment phasing errors.
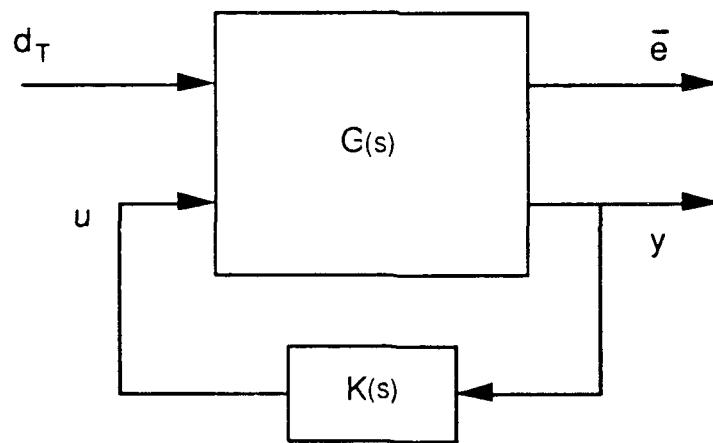
Figure 6.1 Nominal Open-Loop 2-Block System.

This chapter illustrates the details of transforming the BEA model of Chapter 2 into the form discussed in Sections 5.1 and 5.2, which shall then be referred to as the design plant model (DPM). Sections 6.2 and 6.3 address formulation and norm bounding of the error and disturbance vectors, respectively, and Section 6.4 details selection of process and measurement noise levels via simulation and H_∞ requirements analysis. Section 6.5 illustrates augmentation of the 2-block system with the multiplicative error block seen in Figure 5.3 so as to form the nominal open-loop 3-block design model.

6.2 Error Vector Formulation and 2-Norm Bounding

As discussed in Sections 5.1 and 5.2, all quantities that are desired to be kept small by the control system must be included in the error (performance) vector of Figure 5.3. In Section 2.3, the primary performance variables for the SBL BEA were identified as the LOS and segment phasing errors, which were represented as linear combinations of the state variables

$$\bar{e}(t) = \overline{C}_2 x(t)$$

Also, as per assumption 3) of Section 5.2.2.1, the error vector must include a non-singular penalty on the system controls independent of the LOS and segment phasing errors. The error vector can therefore be represented

$$e(t) = \begin{bmatrix} \overline{C}_2 \\ 0 \end{bmatrix} x(t) + 0\, d_T(t) + \begin{bmatrix} 0 \\ \rho\, I \end{bmatrix} u(t) \tag{6.1}$$

which can be seen to meet all assumptions made so far, except for the assumption that $\| e \|_2 \leq 1$. Norm bounding of the error vector will now be addressed.

Consider Figure 6.2, which represents the closed-loop transfer from d to e', where e' represents a scaled version of e such that if the performance goals of Section 2.3 are achieved, then the 2-norm of e' is less than 1.
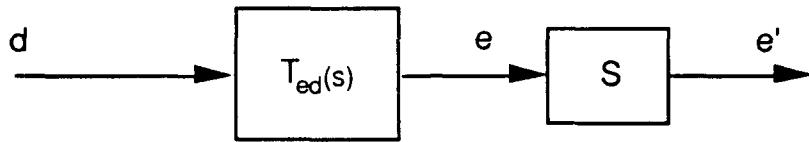
Figure 6.2 Closed-Loop System with Scaled Error Vector.

The problem is to select the diagonal scaling matrix S to accomplish the above conditions. From Figure 6.2

$$e' = S\, e$$

and we want

$$\| e' \|_2 \leq 1$$

However, the performance goals of Section 2.3 were expressed in terms of allowable 2-norms for the segment phasing and LOS errors only, and, therefore, the quantity that we are really interested in bounding is not the 2-norm of e (including controls) but instead

$$\| \bar{e}' \|_2 = \left\| \begin{matrix} e_{sp}' \\ e_{los}' \end{matrix} \right\|_2$$

$$= \sqrt{\| e_{sp}' \|_2 + \| e_{los}' \|_2} \qquad (6.2)$$

By allowing the diagonal elements of S (represented by lower case) to be different only for the segment phasing and LOS components of the error vector

$$e_{sp}' = s_{sp}\, e_{sp}$$

$$e_{los}' = s_{los}\, e_{los}$$

the desired relationship becomes

$$\sqrt{s_{sp}^2 \| e_{sp} \|_2^2 + s_{los}^2 \| e_{los} \|_2^2} \leq 1$$

or, squaring both sides,

$$s_{sp}^2 \, \| \, e_{sp} \, \|_2^2 \; + \; s_{los}^2 \, \| \, e_{los} \, \|_2^2 \; \leq \; 1 \qquad (6.3)$$

At this point, we have one equation and two unknowns (s_{sp} and s_{los}), and therefore we must assign relative importance to the two error terms. Making both error sources equally important results in

$$s_{sp}^2 \, \| \, e_{sp} \, \|_2^2 \; \leq \; \frac{1}{2}$$

$$s_{los}^2 \, \| \, e_{los} \, \|_2^2 \; \leq \; \frac{1}{2} \qquad (6.4)$$

which can be solved trivially to yield

$$s_{sp} \; = \; \frac{1}{\sqrt{2} \, \| \, e_{sp} \, \|_2}$$

$$s_{los} \; = \; \frac{1}{\sqrt{2} \, \| \, e_{los} \, \|_2} \qquad (6.5)$$

Substitution of the values for the allowable 2-norms of the segment phasing and LOS errors obtained in Section 2.3 results in

$$s_{sp} \; = \; \frac{1}{\sqrt{2} \left(0.15 \times 10^{-6} \right)}$$

$$s_{los} \; = \; \frac{1}{\sqrt{2} \left(0.1 \times 10^{-6} \right)} \qquad (6.6)$$

To reduce the dimensionality of the design problem, only 14 of the 27 possible segment phasing outputs were included in the error vector along with the two LOS outputs and 24 controls (scaled by ρ). Therefore, the first 14 diagonal elements of the matrix S are set equal to s_{sp}, the next two are set equal to s_{los}, and the final 24 diagonal elements (corresponding to the system controls) are set equal to one. Since we now want to work with e' instead of e, e is replaced with $S^{-1}e$ in (6.1), and multiplying both sides by S yields

84

$$e'(t) = S \begin{bmatrix} \overline{C}_2 \\ 0 \end{bmatrix} x(t) + 0 \, d_T(t) + \begin{bmatrix} 0 \\ \rho I \end{bmatrix} u(t)$$

$$(6.7)$$

as the error equation.

6.3 Disturbance Vector Formulation and 2-Norm Bounding

The robust control system methodology presented in Section 5.1 requires that all exogenous inputs to the system be lumped together to form a single "disturbance" input vector, $d(t)$. As discussed in Chapter 2, the exogenous inputs for the SBL BEA come from only two sources: broadband noise, $\theta(t)$, that results in corruption of sensor measurements, and vibrational torque disturbances, $d_T(t)$, which enter the system as process noise. By combining these two noise sources into a single disturbance vector

$$d(t) = \begin{bmatrix} d_T(t) \\ \theta(t) \end{bmatrix}$$

the system dynamics can be represented

$$\dot{x}(t) = A\,x(t) + [B_{21} \quad 0]\begin{bmatrix} d_T(t) \\ \theta(t) \end{bmatrix} + B_3\,u(t)$$

$$y(t) = C_3\,x(t) + [0 \quad I]\begin{bmatrix} d_T(t) \\ \theta(t) \end{bmatrix} + 0\,u(t)$$

$$(6.8)$$

and (6.7) remains unchanged except for the increased dimension of the zero D_{22} matrix. Note that $B_2 D_{32}{}^T$ and D_{33} are now zero as assumed in Section 5.2.2.1, and we can once again turn to the subject of norm bounding.

Consider Figure 6.3, which represents the closed-loop transfer from d' to e', where now d' has 2-norm less than one.
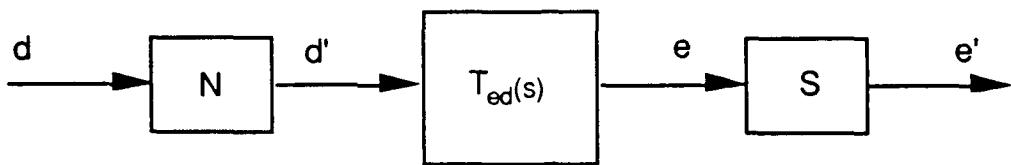
Figure 6.3 Closed-Loop System with Scaled Disturbance and Error Vectors.

By proceeding in exactly the same manner as for the error vector, we arrive at the equations

$$n_{d_T} = \frac{1}{\sqrt{2} \parallel d_T \parallel_2}$$

$$n_\theta = \frac{1}{\sqrt{2} \parallel \theta \parallel_2} \tag{6.9}$$

for the diagonal elements of the disturbance scaling matrix N, and the open-loop 2-block system G(s) is now given by

$$\dot{x}(t) = A x(t) + [B_{21} \ \ 0] N^{-1} d'(t) + B_3 u(t)$$

$$e'(t) = S \begin{bmatrix} \overline{C}_2 \\ 0 \end{bmatrix} x(t) + 0 d'(t) + \begin{bmatrix} 0 \\ \rho I \end{bmatrix} u(t)$$

$$y(t) = C_3 x(t) + [0 \ \ I] N^{-1} d'(t) + 0 u(t) \tag{6.10}$$

or, using lower case letters for the matrices of (6.10) now to avoid confusion in later manipulations,

$$G(s) = \begin{bmatrix} a & b_2 & b_3 \\ \hline c_2 & 0 & d_{23} \\ c_3 & d_{32} & 0 \end{bmatrix} \tag{6.11}$$

Unlike the situation for the error vector, however, we do not have upper bound values for the 2-norms of the torque disturbances and measurement noise. Obtaining these values is the subject of the next section, which falls under the heading of requirements analysis.

6.4 Requirements Analysis via H_∞ Design

6.4.1 Procedure

The H_∞ design problem with known performance specifications formulated above allows requirements analysis to be easily performed by discretizing a search space over a range of allowable disturbance levels and sensor noise norms, and then performing a finite number of H_∞ controller computations. Given reasonable upper and lower bounds for the 2-norms of the disturbances and measurement noises, the open-loop system can be scaled to yield unity bounded d and e vectors as in Sections 6.2 and 6.3, and the closed-loop H_∞ problem solutions then permit attainable performance to be parametrized in terms of these 2-norms. The requirements analysis computations are performed without bandwidth constraints (affected by making ρ in (6.7) very small (= 0.002)), to make certain that the noise levels are the parameters actually driving achievable performance.

6.4.2 Segment Phasing Sensor Configuration Study

Besides establishing 2-norm bounds on the process and measurement noises, another question to be resolved by the requirements analysis process is how many of the 27 segment phasing outputs actually need to be measured to provide enough information for effective control. Intuition suggests that since the BEA ROM does not contain any bending mode dynamics, two measurements along any mirror segment edge border should give enough information to assess the relative positions of the two rigid segments. To verify this and determine the effect of various sensor configurations on achievable performance, six different combinations of segment phasing outputs (see Figure 6.4) were selected for inclusion with the two LOS outputs in the measurement vector, y(t), and the above H_∞-based requirements analysis process was iterated.

87
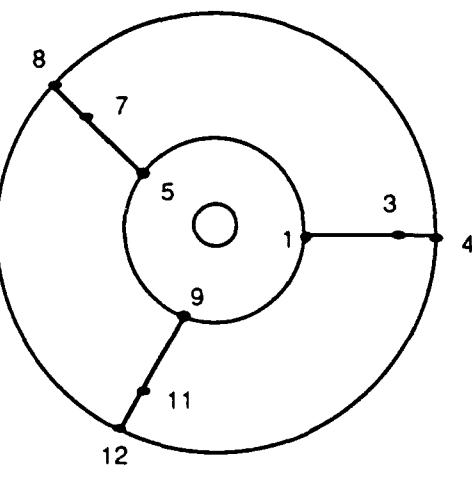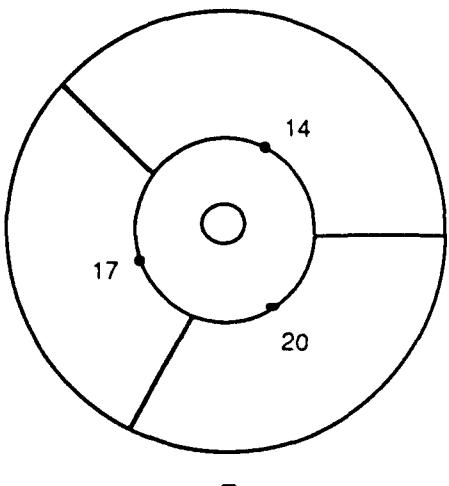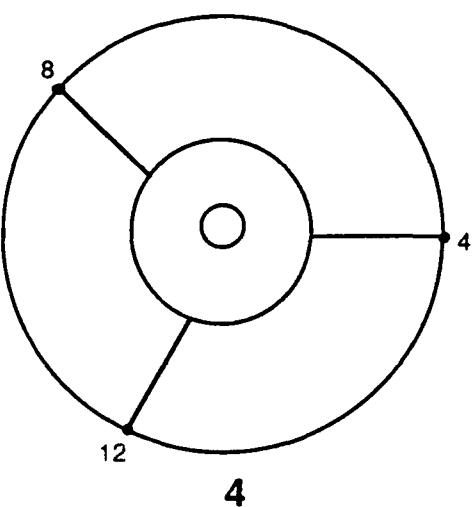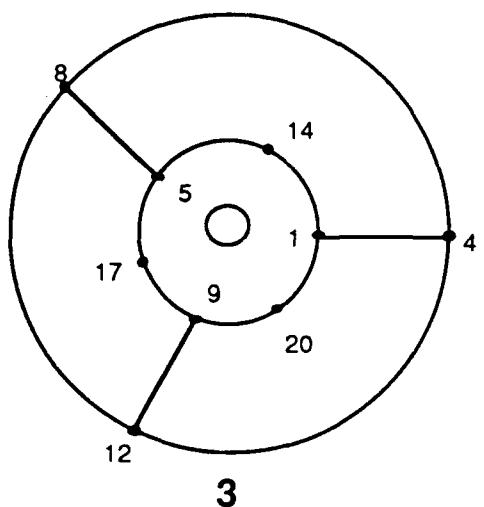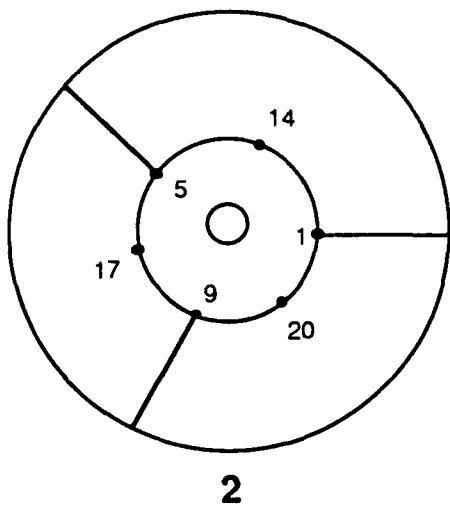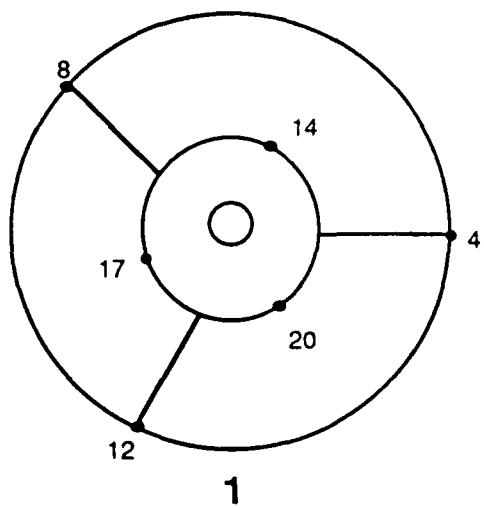
Figure 6.4 Requirements Analysis Sensor Configurations.

Lines of closed-loop infinity-norm (γ) equal to one versus disturbance torque and measurement noise 2-norms for the six different segment phasing sensor configurations of Figure 6.4 are plotted below in Figure 6.5 for an 18-state B&T SBL beam expander model. The 18-state ROM was used to reduce the computation time and effort involved in repeatedly solving the H_∞ Riccati equations (5.8-5.9). Note that the system has been scaled as illustrated in Section 5.2 so that a closed-loop infinity-norm of one indicates that desired performance specifications are met.
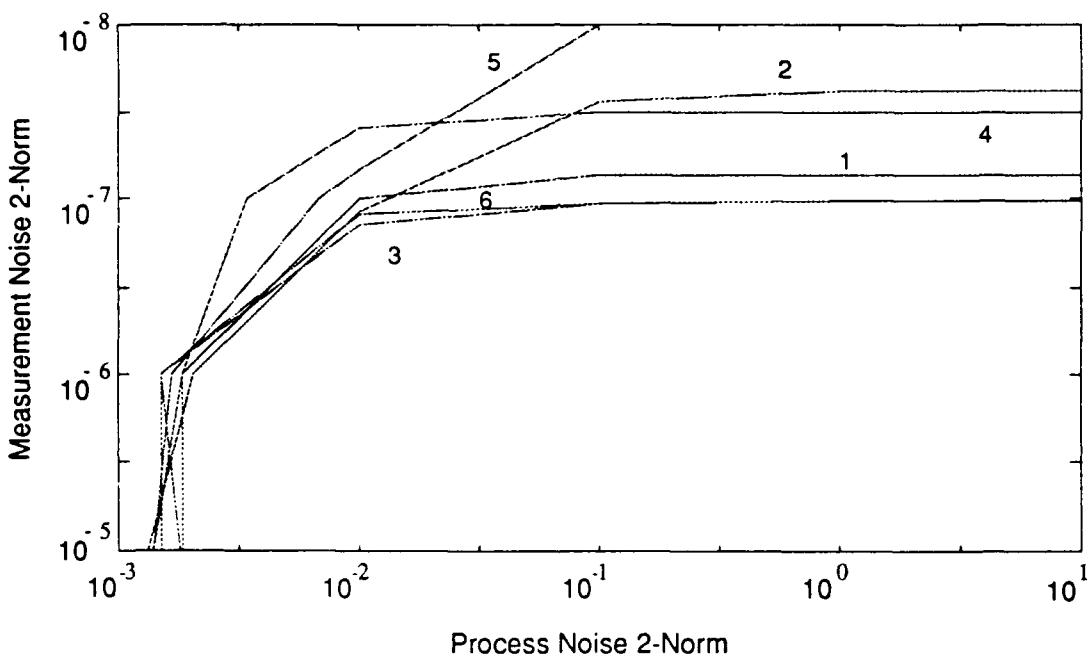
Figure 6.5 $\gamma = 1$ Versus { $\| d_T \|_2$, $\| \theta \|_2$ }.

From Figure 6.5 it can be seen that, for a given level of disturbance torque energy, sensor configurations 3 and 6 allow performance specifications to be met with the largest amount of measurement noise (or least accurate sensors). Sensor configuration 1, which uses only six measurements compared to 9 for configurations 3 and 6, requires only slightly more accurate sensors. Configurations 4 and 5, which employ only 3 measurements each, require significantly more accurate sensors, and configuration 2, which provides 6 segment phasing measurements all taken along the center segment, does not appear to be a good choice either. Based on Figure 6.5 and a desire to reduce dimensionality of the plant model, sensor configuration 1 was chosen to provide the segment phasing measurements

89

for the SBL BEA model. Figure 6.6 illustrates the tradeoffs between achievable closed-loop performance, and process and measurement noise for sensor configuration 1.
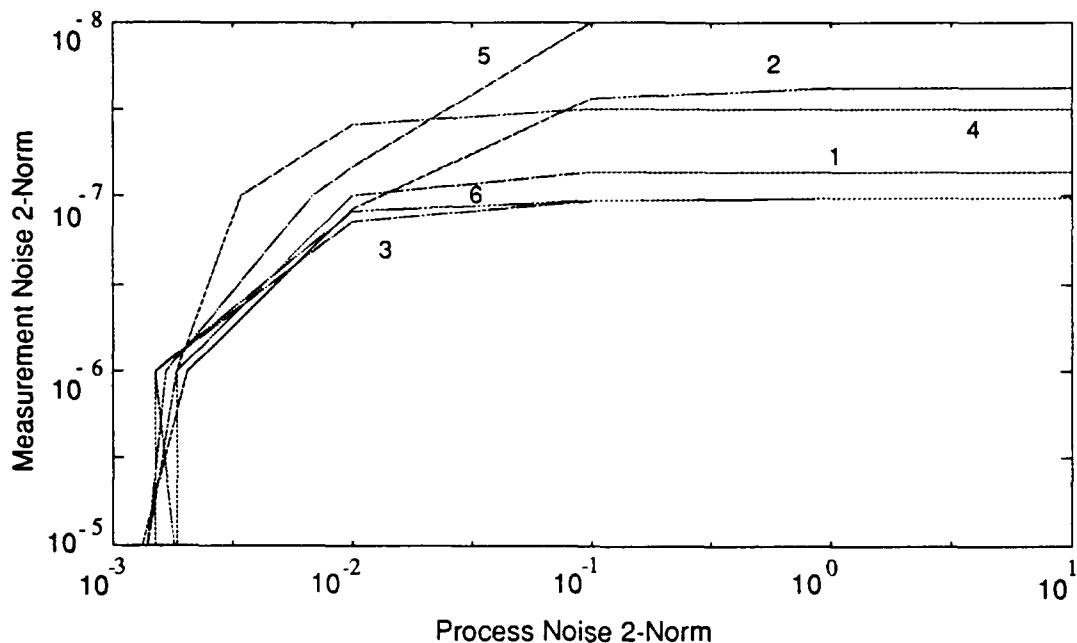
Figure 6.6 Achievable Performance Versus { $\| d_T \|_2$, $\| \theta \|_2$ }
(Sensor Configuration 1).

From this figure, various combinations of disturbance torque and measurement noise 2-norms can be chosen for which performance goals are met. A likely scenario for the SBL disturbance environment will now be created.

6.4.3 Disturbance Environment Scenario

In order to obtain a rough estimate for the level of disturbance torques likely to be experienced by the SBL BEA, the following hypothetical situation is postulated[5]. Due to attitude control and gross pointing requirements, the SBL forebody will often be commanded to perform slew manuevers. In such an event, the SBL system concept calls

---

[5] Effort is made in this thesis to fabricate a reasonable, but not totally realistic, set of disturbance and performance parameters in order that the control system synthesis procedure may be carried out in an illustrative manner. Fully realistic choices for these parameters are not chosen, in order to avoid any complications with the classification status of this document.

90

for the aftbody to reposition itself in order to avoid saturation of the forebody/aftbody gimbal. In performing this manuever, the aftbody will invariably impart some small amount of vibrational energy to the forebody via the gimbal isolation subsystem. Since the aftbody dynamics are not modeled in this thesis, it is assumed that the rigid body motion of the aftbody can be approximated by using the 12-state rigid body dynamics model of the BEA. The torque required to perform various aftbody slew manuevers is computed via simulation with this model, and, due to the dissipating effects of the gimbal isolation system, the torque energy imparted to the BEA is then assumed to be five percent of the torque energy required for the aftbody slew manuever. This five percent figure is consistent with the upper bound on an assumed ability of the vibration isolation subsystem to attenuate transmitted torque by a factor of ten to twenty. In the simulations, the torque input is assumed to be of a sinusoidal nature with period equal to the duration of the slew. Table 6.1 details the one-input maximum torque required to slew the SBL LOS through various angles parametrized versus selected slew durations.

$d_{T (max)}$ (N-m)	Slew Duration, T (sec)	$\Delta\theta$ (degrees)
10	10	0.27
2.2	10	0.06
1	10	0.027
500	1	0.135
100	1	0.027
5	25	0.84
1	25	0.168

Table 6.1 Aftbody Slew Manuever Requirements.

From the choices available in Table 6.1, the 0.06 degree, ten second slew manuever was arbitrarily selected as an upper bound on the allowable demands of slew manuevers. From the table it can be seen that this places an upper bound of 2.2 N-m on the maximum required torque. The 2-norm of the single element torque is given by

$$\| d_{Ti}(t) \|_2 = \left(\int_0^T d_{Ti (max)}^2 \sin^2(\omega t) \, dt \right)^{\frac{1}{2}}$$

91

$$= d_{Ti\,(max)} \left(\frac{T}{2}\right)^{\frac{1}{2}}$$

(6.12)

and is found to have the value 4.92 N-m-s$^{1/2}$ for the selected upper bound values of $d_{Ti(max)}$ and T. Taking five percent of this value yields 0.246 N-m-s$^{1/2}$, which is bounded above by 0.25 N-m-s$^{1/2}$ for convenience. Allowing this maximum 2-norm for both of the disturbance torque elements results in a total disturbance torque 2-norm of

$$\| d_T(t) \|_2 = \sqrt{\| d_{Ti}(t) \|_2^2 + \| d_{Ti}(t) \|_2^2} = 0.353 \text{ N-m-s}^{1/2}$$

(6.13)

for use in (6.8).

Now that a value has been chosen for allowable disturbance torque levels, Figure 6.6 can be used to establish sensor requirements. From the figure, a logarithmic measurement noise 2-norm bound of

$$\log_{10}\left(\| \theta \|_2\right) = -7.85$$

(6.14)

(m-s$^{1/2}$ or rad-s$^{1/2}$ as appropriate) was chosen for use in (6.9), resulting in a value for the 2-norm of θ of 1.414×10^{-8} m-s$^{1/2}$/rad-s$^{1/2}$. This choice allows some leeway for performance to be lost and still meet specifications when the 56-state model is used for design (versus the 18-state model used in computations), and for when plant uncertainty is accounted for via robustness considerations.

Note that the selection of disturbance parameters was performed under deterministic assumptions. As mentioned previously, the design problem can be formulated in a stochastic framework, by interpreting the scale factors in (6.9) as reciprocals of the square roots of intensities of filtered white noise disturbances, or as upper bounds on the RMS values of non-white random disturbances.

The open-loop 2-block system has now been formulated to fit into the robust control system design framework described in the previous sections. Equations (6.6), (6.10-6.11), and (6.12-6.13) provide all the system matrices needed for solution of the H₂ and H∞ Riccati equations presented in Section 5.2.2 ((5.4-5.6) and (5.8-5.11), respectively). What remains to be done is to augment the 2-block system with the multiplicative error block of Figure 5.2, to facilitate closed-loop robustness analysis with the Small Gain

Theorem. Creation of the nominal 3-block system via unstructured uncertainty error bl_ck augmentation will now be addressed.

6.5 Augmentation of the Multiplicative Error Block

As described in Section 5.2, robustness analysis with the Small Gain Theorem requires that all uncertainties in the plant be modeled as stable errors with infinity-norms less than or equal to one. For the SBL BEA robust design problem, the only uncertainties present are the unmodeled high-frequency dynamics truncated in the model reduction process of Chapter 4, as motivated by the need to limit plant dimensionality. Modeling of the error due to the truncated high-frequency dynamics in a manner consistent with the SGT can be accomplished in the following way. Consider Figure 6.7, which, without including measurement noise, shows the plant uncertainty due to model reduction as a multiplicative error at the plant output.
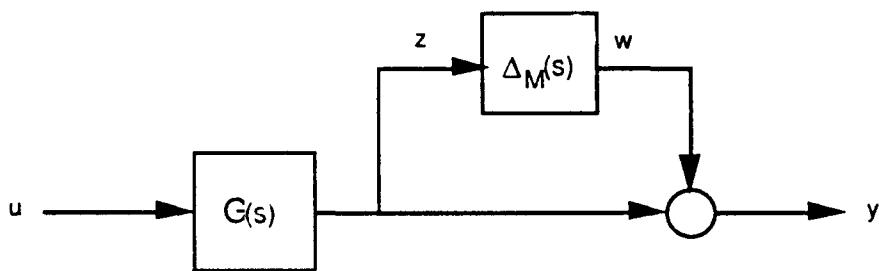
Figure 6.7 ROM with Multiplicative Modeling Error.

By comparing Figure 6.7 with Figure 6.8, which shows the actual 1-block open-loop plant, $G_a(s)$,
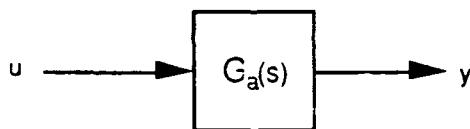
Figure 6.8 Actual Open-Loop Plant.

it can be seen that

$$G_a(s) = \left(I + \Delta_M(s)\right) G(s) \qquad (6.15)$$

Solving for $\Delta_M(s)$,

$$\Delta_M(s) = (G_a(s) - G(s)) G(s)^{-1} \qquad (6.16)$$

Thus, by using the state-space realization of the 120-state B&T model for $G_a(s)$ and the state-space realization of the 56-state ROM for $G(s)$, and computing the right-hand-side of (6.16) as a function of frequency, the singular value frequency response of the multiplicative error at the plant output due to model reduction can be obtained. Note that by using the 120-state B&T model for the actual plant instead of the 390-state full model, we are neglecting the effects of the other 270 full model states on the system frequency response, which in Chapter 4 were seen to be slight. More importantly, however, by using a minimal realization for $G(s)$, we are guaranteeing that $G(s)$ is non-singular, and therefore $G(s)^{-1}$ will be computable at all frequencies. Figure 6.9 shows the maximum singular value frequency response for the plant output multiplicative error due to model reduction, calculated as discussed above.
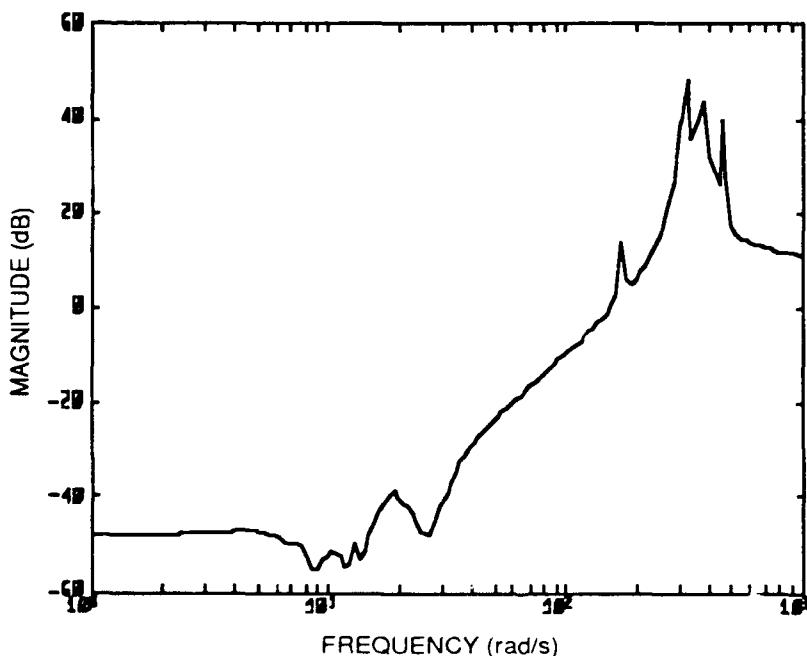
Figure 6.9 Multiplicative Modeling Error at the Plant Output.

As can be seen from the figure, the error is small at low frequencies where all the vibrational modes of the mirror segments were retained, and jumps up to very high values in the 200 to 600 rad/sec frequency range where the bending mode dynamics have been truncated. The error reaches significant levels (0 dB) at about 100 rad/sec.

In order for this error representation to be useful in testing robustness, a state-space realization must be obtained, and scaling must be performed so that the infinity-norm of $\Delta_M(s)$ is less than or equal to one. To illustrate how this process may be accomplished, consider Figure 6.10, which is just Figure 6.7 except that now

$$\Delta_M(s) \leq F(s) \underline{\Delta}_M(\underline{s})$$ (6.17)

where F(s) is any stable transfer function which effectively represents an upper bound on the multiplicative error maximum singular value response, and $\|\Delta_M(s)\|_\infty$ is less than or equal to one.
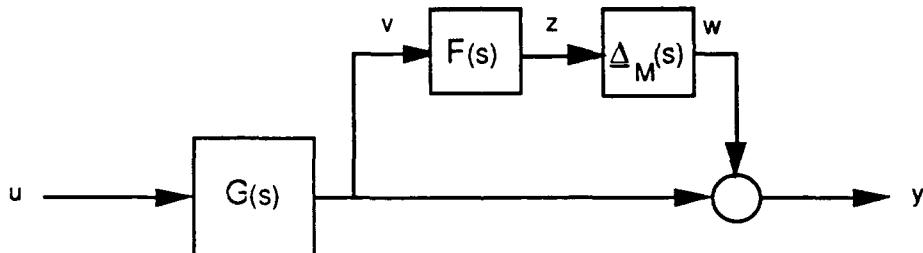
Figure 6.10 ROM with Scaled Error Block.

By augmenting the dynamics of G(s) to include the dynamics of the error bounding filter, F(s), the system of Figure 6.10 can be expressed as in Figure 6.11, which is an appropriate form for use in analysis with the Small Gain Theorem.

95
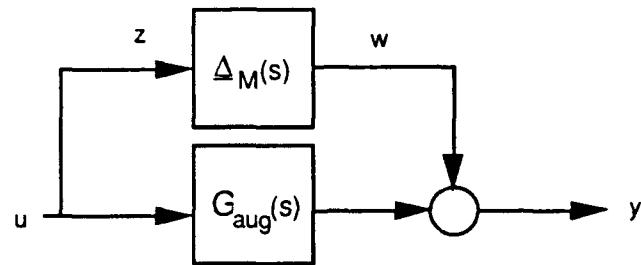
Figure 6.11 Augmented Plant with Scaled Error Block.

This procedure shall now be carried out for the SBL BEA design problem. Consider Figure 6.11, which shows the multiplicative error at the plant output maximum singular value frequency response, and a third-order, single-input/single-output, minimum-phase, and stable transfer function frequency response which effectively bounds the multiplicative error response curve.
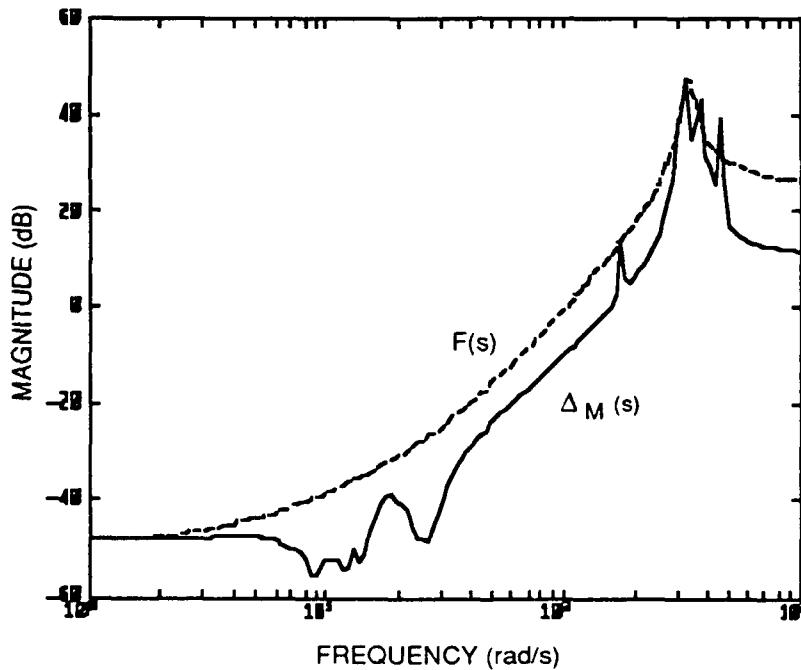
Figure 6.12 Plant Output Multiplicative Modeling Error
and Bounding Transfer Function, F(s).

If a state-space realization for this bounding transfer function is

$$\left[\begin{array}{c|c} a_f & b_f \\ \hline c_f & d_f \end{array}\right] \tag{6.18}$$

then a state-space realization for F(s) can be obtained by realizing that each channel of the output must be independently filtered by (6.18) to satisfy (6.17), since it is not known in which channel the maximum transfer will occur. Enlarging the dimension of (6.18) to correspond to the dimension of the plant output, which in this case is eight, results in a 24 state, uncoupled state-space realization for F(s)

$$F(s) \ = \ \left[\begin{array}{c|c} a_f I_8 & b_f I_8 \\ \hline c_f I_8 & d_f I_8 \end{array}\right] \ = \ \left[\begin{array}{c|c} A_f & B_f \\ \hline C_f & D_f \end{array}\right] \tag{6.19}$$

where I_8 is an 8 x 8 identity matrix.

The dynamics of the error scaling filter can now be augmented to the ROM state-space realization of G(s) (6.11) by writing the equations for the filter as

$$\dot{p}(t) \ = \ A_f\, p(t) \ + \ B_f\, v(t)$$

$$z(t) \ = \ C_f\, p(t) \ + \ D_f\, v(t) \tag{6.20}$$

and recognizing that the input to the shaping filter is equal to the state component of the output:

$$v(t) \ = \ C_3\, x(t) \tag{6.21}$$

so that

$$\left[\begin{array}{c} \dot{x}(t) \\ \dot{p}(t) \end{array}\right] = \left[\begin{array}{cc} a & 0 \\ B_f c_3 & A_f \end{array}\right]\left[\begin{array}{c} x(t) \\ p(t) \end{array}\right] + \left[\begin{array}{c} 0 \\ 0 \end{array}\right] w(t) + \left[\begin{array}{c} b_2 \\ 0 \end{array}\right] d'(t) + \left[\begin{array}{c} b_3 \\ 0 \end{array}\right] u(t)$$

$$w(t) = \left[\begin{array}{cc} D_f c_3 & C_f \end{array}\right]\left[\begin{array}{c} x(t) \\ p(t) \end{array}\right] + 0\, w(t) + 0\, d'(t) + 0\, u(t)$$

$$e'(t) = \left[\begin{array}{cc} c_2 & 0 \end{array}\right]\left[\begin{array}{c} x(t) \\ p(t) \end{array}\right] + 0\, w(t) + 0\, d'(t) + d_{23}\, u(t)$$

$$y(t) = [c_3 \quad 0] \begin{bmatrix} x(t) \\ p(t) \end{bmatrix} + I\,w(t) + d_{32}\,d'(t) + 0\,u(t) \tag{6.22}$$

Equation (6.22) gives the 3-block augmented plant, $G_{aug}(s)$, in the form required for robustness analysis via the Small Gain Theorem described in Section 5.2. The design model has now been fully formulated so that control system synthesis and robustness analysis may proceed. This topic is addressed is Chapter 7.

CHAPTER 7

Compensator Designs

7.1 Introduction

In this chapter, the controller design methods of Section 5.3 are applied to the BEA open-loop 2-block system given by (6.10-6.11), and nominal performance and robustness analyses are performed on the system obtained by closing the resulting compensator loop (substituting $u = Ky$) of the augmented 3-block system given by (6.22). Three basic types of compensator designs are presented. The first type (Section 7.2) is the unconstrained bandwidth H_2/H_∞ design arising as a natural extension of the requirements analysis of Section 6.4, and which provides a lower bound on achievable performance without regard to stability robustness or actuator constraints. Section 7.3 presents robustly stable H_2/H_∞ designs accomplished via inclusion of constant control penalty in the performance vector. Frequency dependent penalty of the error and/or control gives rise to H_2/H_∞ loop-shaping designs, which are presented in Section 7.4. In order to strike a balance between presenting too much or too little information to make meaningful comparisons between designs, the method of design presentation chosen focuses on certain important maximum singular value frequency response plots. These plots are intended to capture and illustrate the significant differences between the various designs, without overloading the reader with too much information to readily digest. The level of information available in these plots is sufficient for selection of a best design and illustration of its major characteristics, which is the immediate objective of this chapter. More detailed discussion of the selected design is then presented in Chapter 8, where design implementation/validation issues are considered.

In this chapter, the unconstrained bandwidth H_2 and H_∞ designs are shown to validate the requirements analysis process of Chapter 6, and both designs are shown to meet nominal performance specifications. However, as might be expected, the resulting high bandwidths of these designs are seen to have sufficient potential to excite the neglected high-frequency dynamics so that they violate the stability robustness test of the Small Gain Theorem, making these designs unacceptable. Incorporating significant constant control penalty into the error vector is seen to solve the stability robustness problem, but results in an unacceptable degradation of closed-loop system performance. By using loop-shaping techniques on the system errors in conjunction with H_2 optimal control, robust designs that meet performance goals over limited low and high-frequency bands are then developed. Since the system disturbances are assumed to be broadband in nature and therefore have significant power in between these low and high frequency regions, this too is an unacceptable solution. Finally, frequency dependent penalty of the system controls and H_∞ optimal control yield the desired combination of robust stability and desired closed-loop performance over the entire frequency range of interest.

7.2 Nominal Performance (Unconstrained Bandwidth) Designs

As mentioned previously, the requirements analysis of Section 6.4 which determined levels of process and measurement noise used to establish the DPM was performed on an 18-state B&T BEA reduced-order model without bandwidth constraints ($\rho = 0.002$). In order to assess the change in achievable performance incurred by increasing the model dimension from 18 to 56 states, but still using unlimited control authority, the H_∞ optimal controller is recomputed in this section using the DPM system matrices of (6.10-6.11), and nominal closed-loop performance ($\|T_{22}(s)\|_\infty$) is reevaluated. Also, we would like to ascertain how close the DPM-based unconstrained bandwidth design comes to meeting the stability robustness test of the Small Gain Theorem, so the infinity-norm of the T_{11} block is computed as well.

Figure 7.1 shows the open and closed-loop transfer maximum singular value frequency response plots from d to e for the plant model and unconstrained bandwidth H_∞ design, respectively. For purposes of comparison, the closed-loop nominal performance maximum singular value frequency response is also shown for an H_2 optimal controller derived from the same plant model realization. As can be seen from Figure 7.1, closing the feedback loop about either unconstrained bandwidth controller results in a system that achieves

nominal performance specifications (closed-loop transfer infinity-norm from d to e less than 1 (0 dB)), effecting an over 60 dB decrease in worst-case system transfer from the disturbances to the errors when compared to open-loop performance. Note that over most of the frequency range of interest, the H_2 design outperforms the H_∞ design (in terms of better disturbance attenuation), but the H_∞ response has a slightly smaller infinity-norm (-7.54 dB versus -2.43 dB), indicating that it has better worst-case disturbance rejection properties than the H_2 design. Also, the H_∞ response is flatter than the H_2 response, suggesting that the H_∞ design achieves a more perfect inversion of the open-loop dynamics.
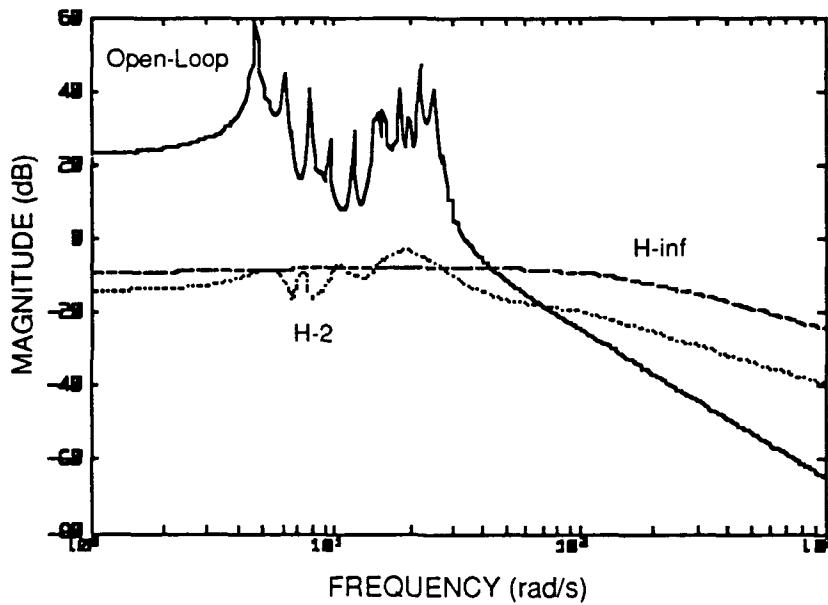
Figure 7.1 Open and Closed-Loop Transfer From All Disturbances to All Errors (T_{22}) (Unconstrained Bandwidth Designs).

Recalling that the disturbance vector contains both torque disturbances and sensor measurement noise, and that the error vector has both segment phasing and LOS terms, the closed-loop transfer from d to e can be partitioned

$$\begin{bmatrix} e_{sp} \\ e_{los} \end{bmatrix} = \begin{bmatrix} T_{2211}(s) & T_{2212}(s) \\ T_{2221}(s) & T_{2222}(s) \end{bmatrix} \begin{bmatrix} d_T \\ \theta \end{bmatrix}$$

(7.1)

and the singular value frequency responses of the four sub-blocks can be computed to

101

provide insight into the effects of the various terms. Figures 7.2-7.5 show the maximum singular value frequency responses for the T_{2211}, T_{2212}, T_{2221}, and T_{2222} sub-blocks, respectively. From Figure 7.3 it is clear that the transfer from the measurement or sensor noise to the segment phasing errors is driving achievable performance for the unconstrained bandwidth designs. This verifies the conclusion drawn earlier from the requirements analysis process, in which we saw (recall Figure 6.6) that for disturbance torque 2-norms greater than 0.01, achievable performance varied only with measurement noise. Note that it also makes sense that the segment phasing errors are driving performance rather than LOS errors, since the open-loop transfer to the segment phasing errors was about 13 dB greater than the open-loop transfer to the LOS errors.
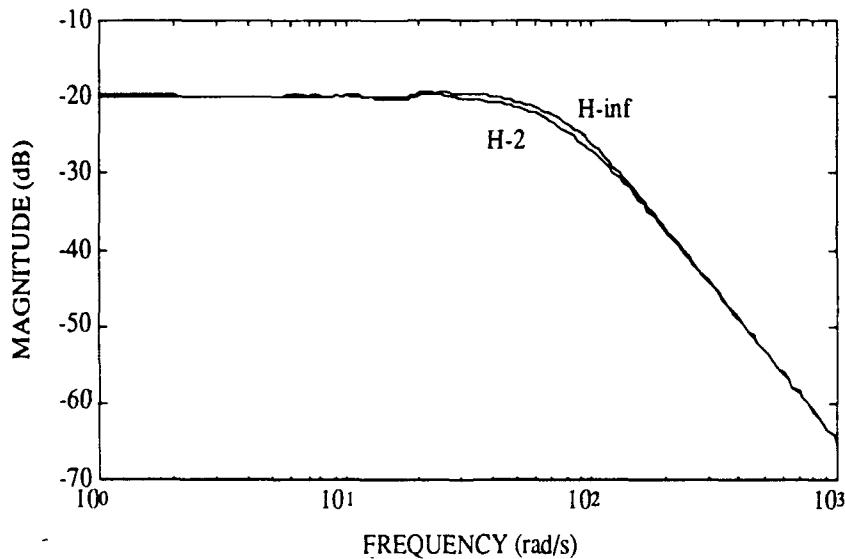
Figure 7.2 Max. Singular Value Closed-Loop Transfer from
Torque Disturbances to Segment Phasing Errors (T_{2211})
(Unconstrained Bandwidth Designs).

102
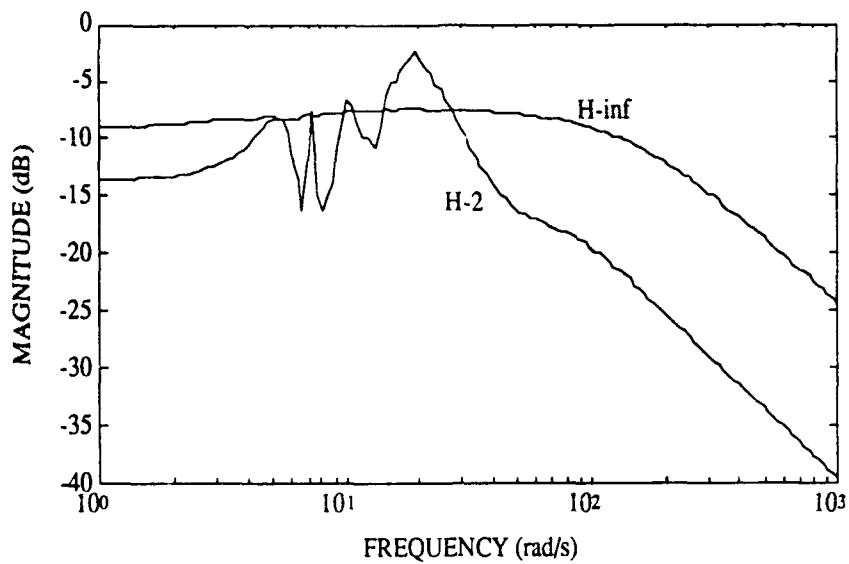
Figure 7.3 Max. Singular Value Closed-Loop Transfer from
Sensor Noise to Segment Phasing Errors (T_{2212})
(Unconstrained Bandwidth Designs).
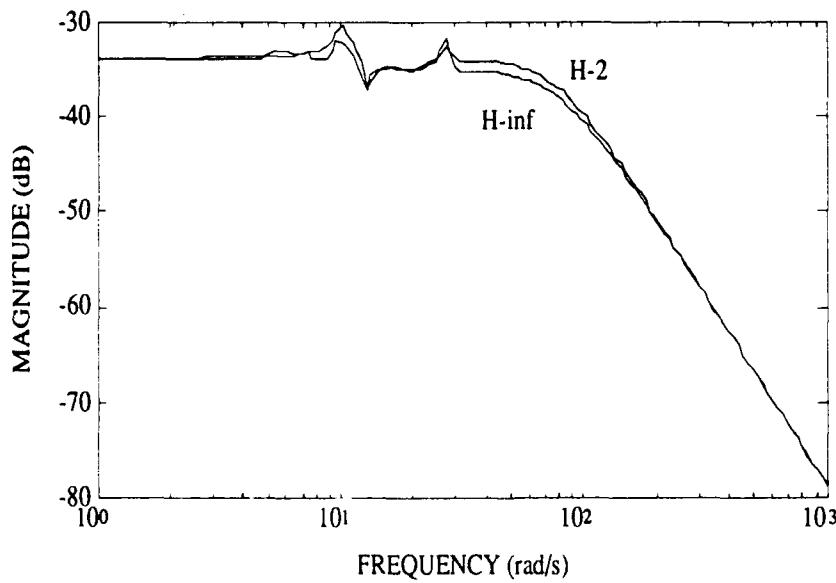
Figure 7.4 Max. Singular Value Closed-Loop Transfer from
Torque Disturbances to Line-of-Sight Errors (T_{2221})
(Unconstrained Bandwidth Designs).
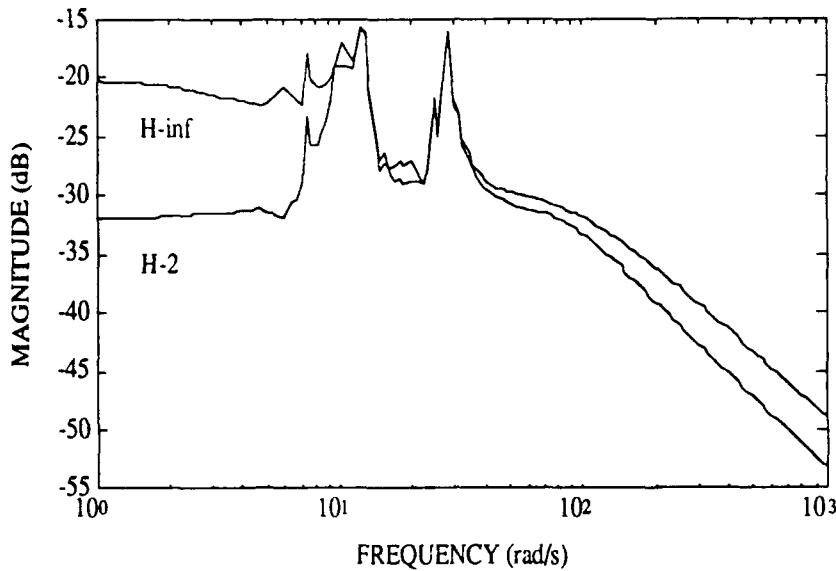
Figure 7.5 Max. Singular Value Closed-Loop Transfer from
Sensor Noise to Line-of-Sight Errors (T_{2222})
(Unconstrained Bandwidth Designs).

Turning to stability robustness issues, since both these designs employ virtually no penalty on control authority, they should be expected to possess high gain, high bandwidth characteristics. As there is significant modeling error at high frequencies as well, the combined large error and loop gain at high frequencies should severely degrade the ability of these systems to satisfy the Small Gain Theorem. In order to verify this conjecture, consider Figure 7.6, which shows the closed-loop transfer about the multiplicative error block, T_{11}, for the unconstrained bandwidth H_2 and H_∞ designs. As predicted, from Figure 7.6 it is clear that both designs violate the stability robustness test of the Small Gain Theorem, as there is a large high-frequency region ($\omega > 100$ rad/sec) in which the closed-loop transfer about the delta block is greater than 1 (0 dB). In fact, the unconstrained bandwidth designs do not even come close to meeting the stability robustness condition, as the infinity-norms of both T_{11} blocks can be seen to be approximately 40 dB. Recalling that the nominal plant rolls off at high frequencies, it would seem that the SGT is being violated due to too much gain being injected by the controllers at high frequencies. To verify this, consider Figure 7.7, which shows the compensator maximum singular value frequency response for both designs. From this figure it is clear that both compensators are indeed injecting high gains at high frequencies, creating a possibility for excitation of

104

the truncated bending mode dynamics, and leading to possible instability due to high-frequency gain considerations. Thus, from Figure 7.7 it is obvious why the closed-loop system violates the stability robustness test of the Small Gain Theorem.
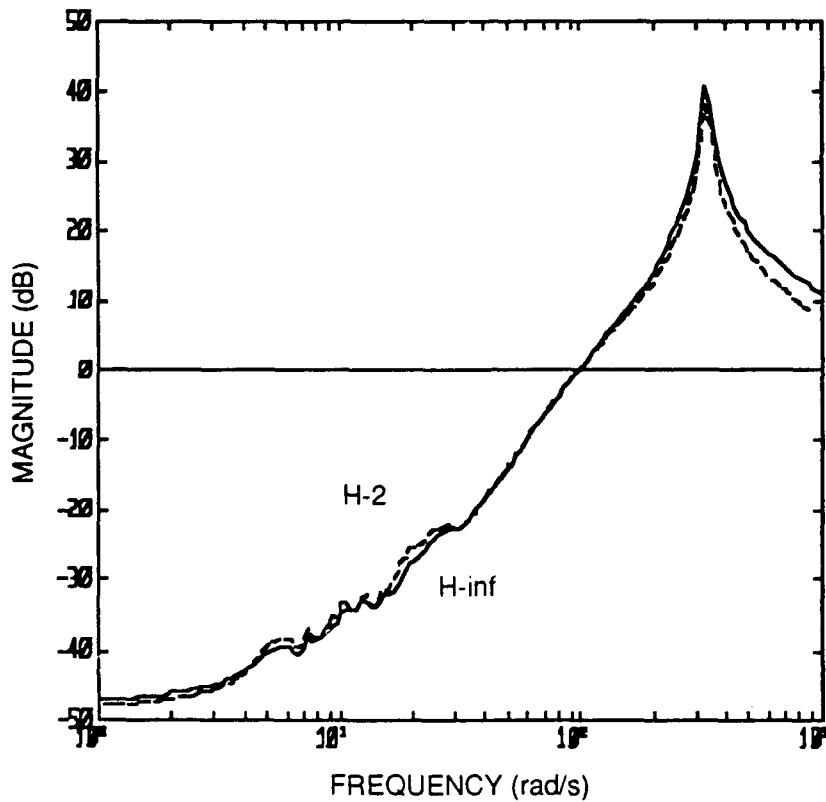
Figure 7.6 Closed-Loop Transfer About Δ_M (T_{11})
(Unconstrained Bandwidth Designs).
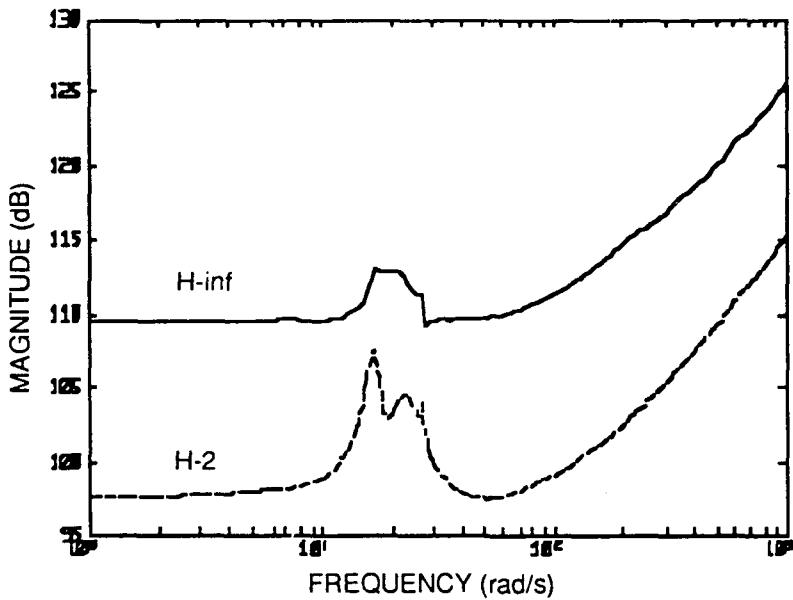
Figure 7.7 Unconstrained Bandwidth Compensator Maximum
Singular Value Frequency Responses.

The final transfer function which is used in this thesis to evaluate compensator performance is the the closed-loop transfer function matrix with the loop broken at the plant output, $C_o(j\omega)$, given by

$$C_o(j\omega) = \{I - G(j\omega) K(j\omega)\}^{-1} \{-G(j\omega) K(j\omega)\} \cdot \qquad (7.2)$$

Note that this transfer function is the "complementary sensitivity function" to the sensitivity function at the plant output, $S_o(j\omega)$, discussed in Section 3.3 in that

$$C_o(j\omega) + S_o(j\omega) = I \text{ for all } \omega \qquad (7.3)$$

The complementary sensitivity function at the plant output provides several pieces of information that are typically useful in evaluating compensator performance. $C_o(j\omega)$ describes the transfer from a reference input at the output to the output itself, and is thus a measure of command following performance at the plant output. $C_o(j\omega)$ is also commonly

106

used to determine the closed-loop system bandwidth[6], a quantity which is known to provide a rough measure of closed-loop system response time to a step input [7]. Finally, $C_o(j\omega)$ provides information relevant to compensator implementation issues that are discussed in Chapter 8. Since command following is not a design characteristic of interest to the pure disturbance rejection problem being considered in this thesis and since implementation issues are addressed in Chapter 8, the main use that will be made of the $C_o(j\omega)$ frequency response plots presented in this chapter is to assess closed-loop system bandwidth.

The maximum singular values of $C_o(j\omega)$ versus frequency for the robust H_2 and H_∞ designs are shown in Figure 7.8. From Figure 7.8 it appears that the two designs have similar bandwidths. Close examination of the singular values reveals this to be the case, with the bandwidth of the H_∞ design approximately equal to 150 rad/s, and the bandwidth of the H_2 design approximately equal to 155 rad/s. The H_2 design should therefore be expected to exhibit a slightly faster attenuation of a step output error than the H_∞ design.

---

[6] In this thesis, the bandwidth of a system is given in terms of its complementary sensitivity function at the plant output, $C_o(j\omega)$, and is determined as the frequency at which $C_o(j\omega) = C_o(0) - 3$ dB.
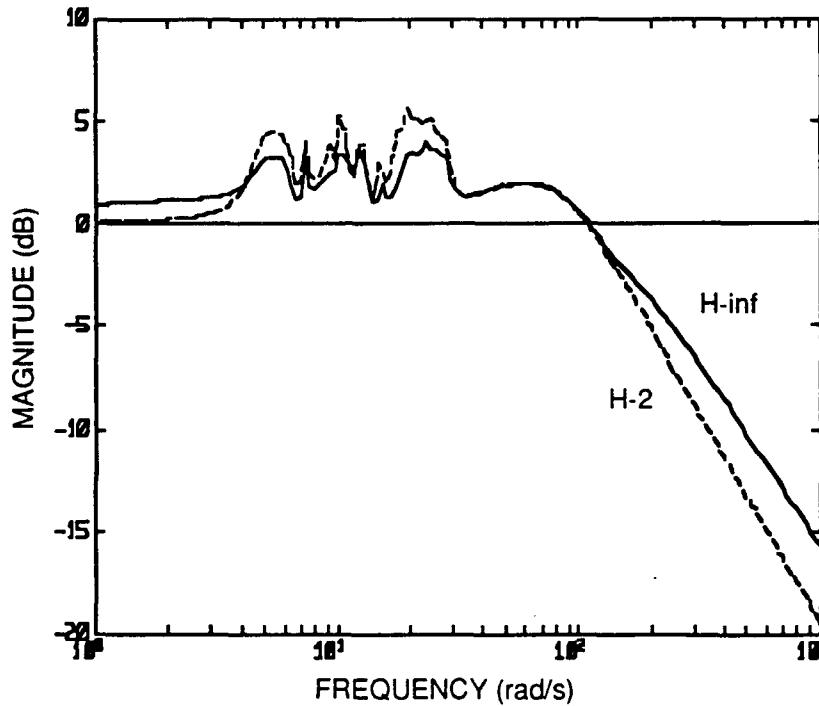
Figure 7.8 Complementary Sensitivity at Plant Output
(Unconstrained Bandwidth Designs).

From the results presented in this section, it can be seen that both unconstrained bandwidth designs have no difficulty in meeting the performance specifications prescribed in Chapter 2. Indeed, both the H_2 and H_∞ designs presented can do significantly better than desired performance objectives; however, they do so in a way that violates the stability robustness test of the Small Gain Theorem. From Figures 7.6 and 7.7, it is clear that this occurs because too much gain is being injected by the compensators at high frequencies. Methods of reducing the high-frequency gain so that a robustly stable design is achieved are now addressed.

7.3 Robust Designs

Traditional means of overcoming the high-frequency, high gain problem displayed by the unconstrained bandwidth designs of Section 7.2 involve increasing the value of ρ in (6.1), so that the error vector effectively penalizes the system control, u, at all frequencies. This tends to limit the amount of gain injected by the compensator at all frequencies so that the system bandwidth is decreased, which is desirable from a stability robustness point of

108

view, but has the undesirable consequence of making the system time response more sluggish. Stability robustness is obtained via this methodology by increasing the penalty weighting on u until the gain injected at high frequencies diminishes enough to offset the large modeling error present. Figures 7.9 and 7.10 show open and closed-loop transfer maximum singular value plots from d to e and about Δ_M, respectively, for robust H_2 and H_∞ designs achieved by increasing the value of ρ from 0.002 to 6000. From Figure 7.9 it can be seen that the robust H_2 and H_∞ designs appear to be nearly identical in terms of closed-loop performance, the main difference being a slightly greater infinity-norm for the H_2 design (the H_∞ design has a performance transfer function infinity-norm of 11.1 dB, compared to 11.4 dB for the H_2 design). Also, as indicated by the figure, both these designs exhibit unacceptable disturbance amplification (> 0 dB) in the frequency range from dc to ~30 rad/s, so that performance specifications are not met by either design. Figure 7.10, however, indicates that both designs are robustly stable. Therefore, although bandwidth reduction has resulted in a sacrifice of about 20 dB in worst-case disturbance rejection performance from the unconstrained bandwidth designs, it has been effective in achieving the important goal of stability robustness.

Figures 7.9 and 7.10 and the preceding discussion clearly illustrate the nature of a tradeoff existing between obtaining stability robustness via bandwidth reduction and formulating the optimal control problem so as to strictly attain nominal performance objectives. As seen in Section 7.2, the unconstrained bandwidth option yields a system with excellent nominal performance, but unacceptable robustness qualities. As illustrated in this section, frequency independent penalty of the control reduces the high-frequency gain as desired so that stability robustness is achieved, but also penalizes the control at low frequency, so that an unavoidable degradation in nominal performance results. Figure 7.9 indicates, though, that even with this degradation, the reduced bandwidth robust designs still manage to accomplish a significant improvement over the open-loop performance of the system.
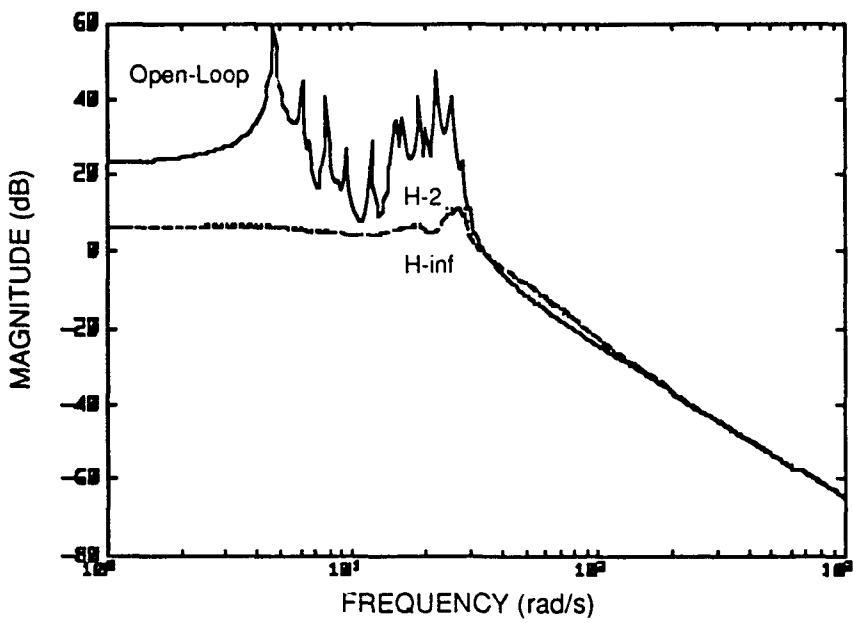
Figure 7.9 Open and Closed-Loop Transfer From All Disturbances to All Errors (T_{22})
(Robust Designs).
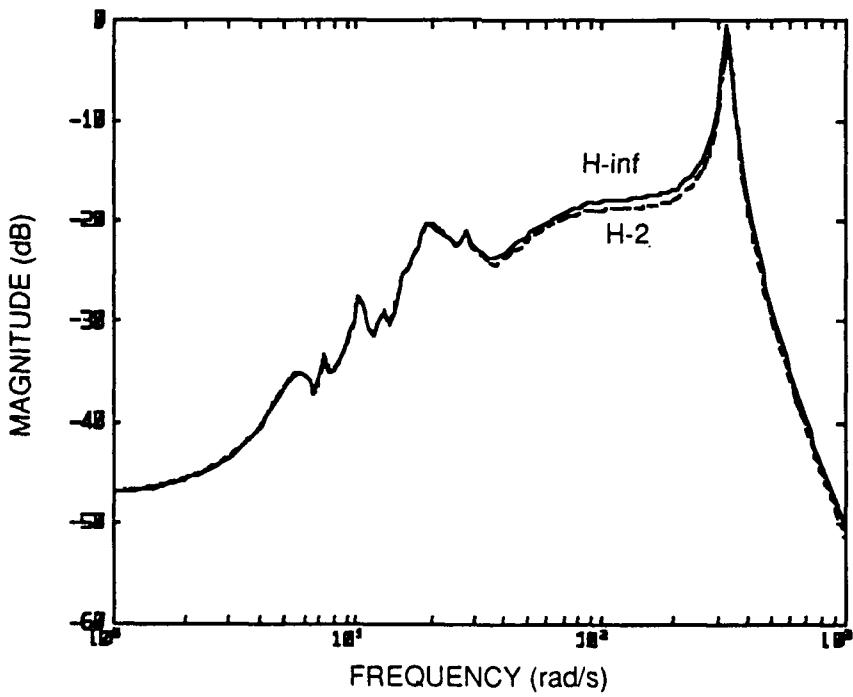
Figure 7.10 Closed-Loop Transfer About Δ_M (T_{11})
(Robust Designs).

110

To see which combination of disturbances and errors is now driving performance, consider Figures 7.11-7.14, which show the maximum singular value frequency responses for the T_{2211}, T_{2212}, T_{2221}, and T_{2222} sub-blocks of the robust designs. Note that now it is the transfer from the disturbance torques to the LOS errors that is driving attainable closed-loop performance, and that the transfer from the torques to both sets of performance variables no longer meets performance specifications. The figures also indicate that measurement noise is no longer a factor in determining performance, which is the result intended by selection of the allowable measurement noise levels in the requirements analysis process.
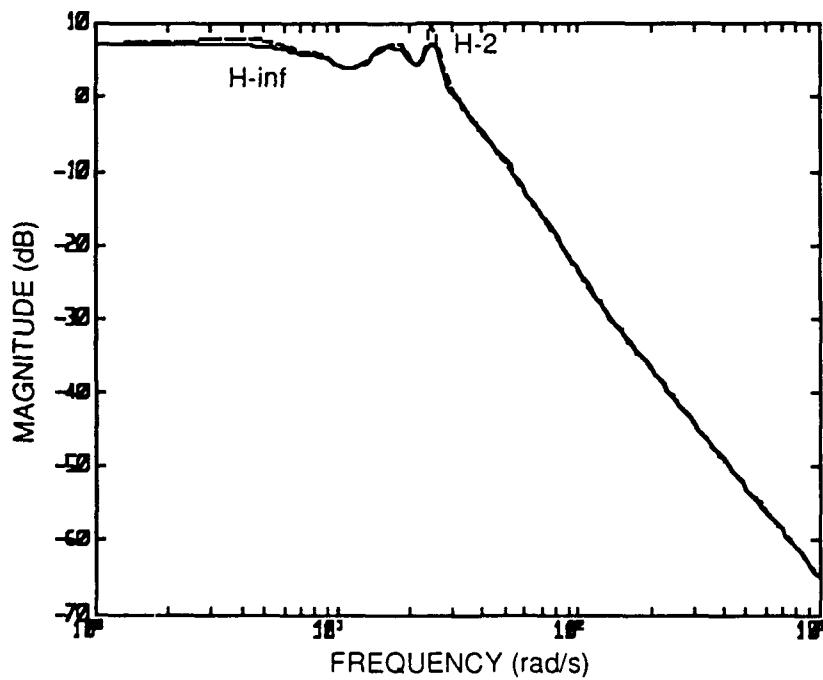
Figure 7.11 Max. Singular Value Closed-Loop Transfer from
Torque Disturbances to Segment Phasing Errors (T_{2211})
(Robust Designs).
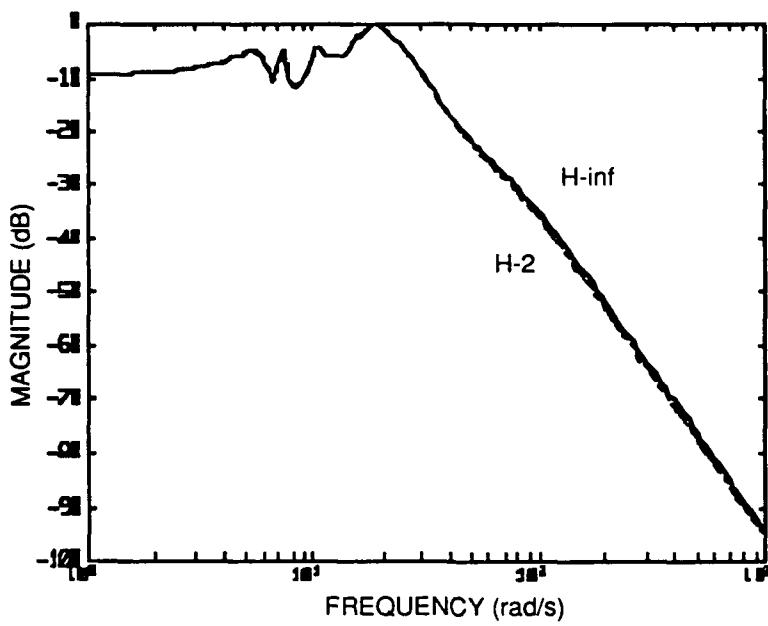
Figure 7.12 Max. Singular Value Closed-Loop Transfer from
Sensor Noise to Line-of-Sight Errors (T_{2212})
(Robust Designs).
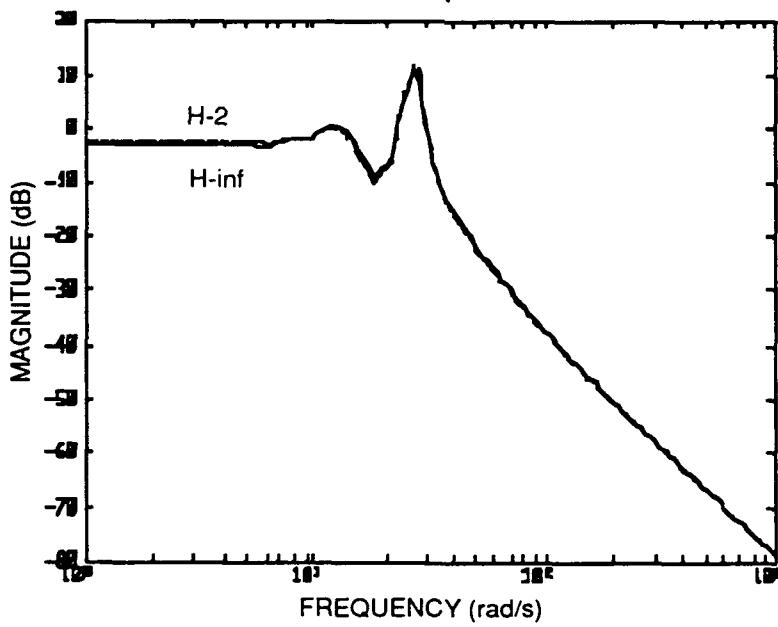
Figure 7.13 Max. Singular Value Closed-Loop Transfer from
Torque Disturbances to Line-of-Sight Errors (T_{2221})
(Robust Designs).

112
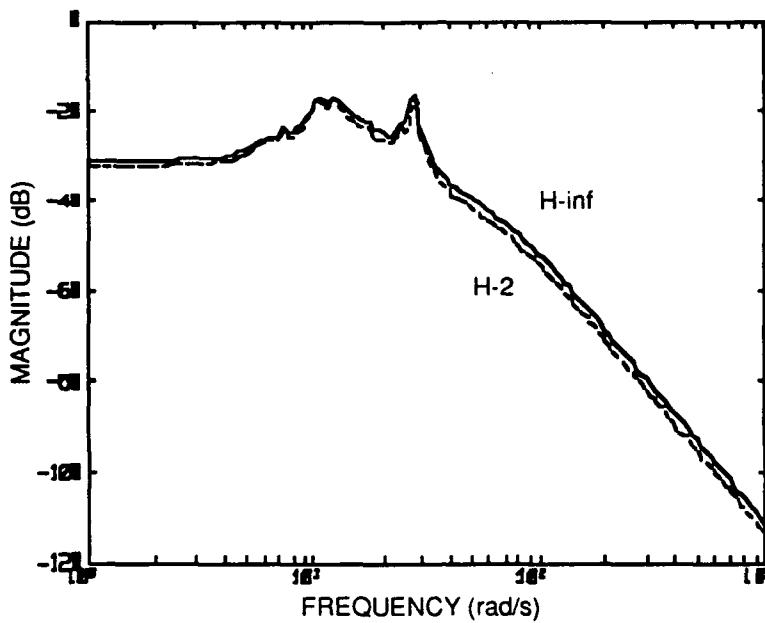
Figure 7.14 Max. Singular Value Closed-Loop Transfer from
Sensor Noise to Line-of-Sight Errors (T$_{2222}$)
(Robust Designs).

To gain more insight into how stability robustness has been achieved with these designs, consider Figure 7.15, which shows the maximum singular value frequency responses of the robust H$_2$ and H$_\infty$ compensators. Note that the two curves are very similar up to about 20 rad/s, where the H$_\infty$ design again starts to display higher gain than the H$_2$ design. The most significant thing to be observed from the figure is that now both compensators are rolling off the injected gain at about the 100 radians per second mark. This is what allows the designs to meet the stability robustness test of the Small Gain Theorem. Also important to note is the over two orders of magnitude (40 dB) drop in gain injected at lower frequencies compared to the unconstrained bandwidth designs (reference Figure 7.7), resulting in the degradation in nominal performance displayed by the robust designs. This is the expected result of penalizing the control at low as well as at high frequency.

113
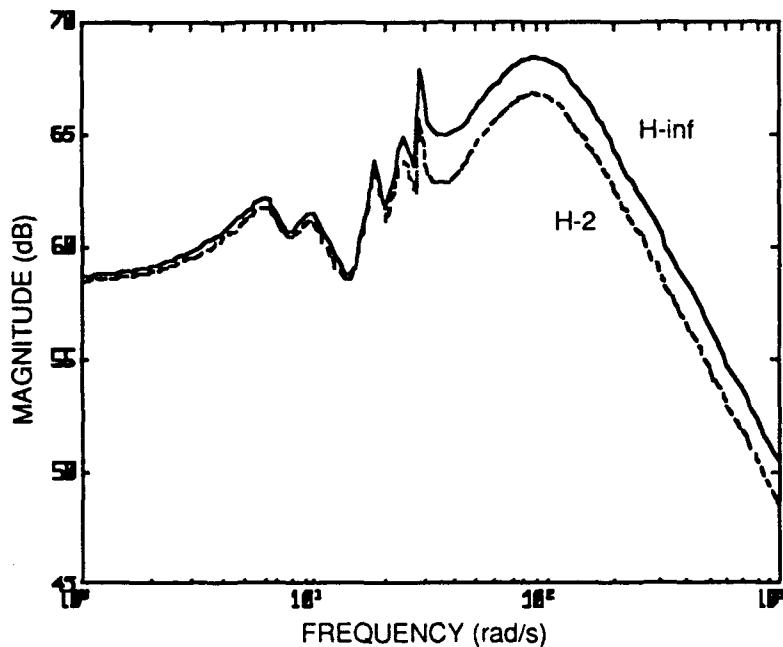
Figure 7.15 Robust Compensator Maximum Singular Value
Frequency Responses.

Earlier in this section, the claim was made that imposing constant (frequency-independent) control penalty in the error vector resulted in a decrease of closed-loop system bandwidth. To verify this claim, consider Figure 7.16, which shows the closed-loop gain at the plant output, $C_0(j\omega)$, for the robust designs. As is evident form the figure, the closed-loop bandwidth has indeed decreased markedly, from ~160-180 radians per second in the unconstrained bandwidth designs to about 36 radians per second in the robust designs. The time response of the robust designs should therefore be expected to be significantly more sluggish than that of the unconstrained bandwidth designs. This is further evidence of the sacrifices incurred by obtaining stability robustness via constant control penalty.
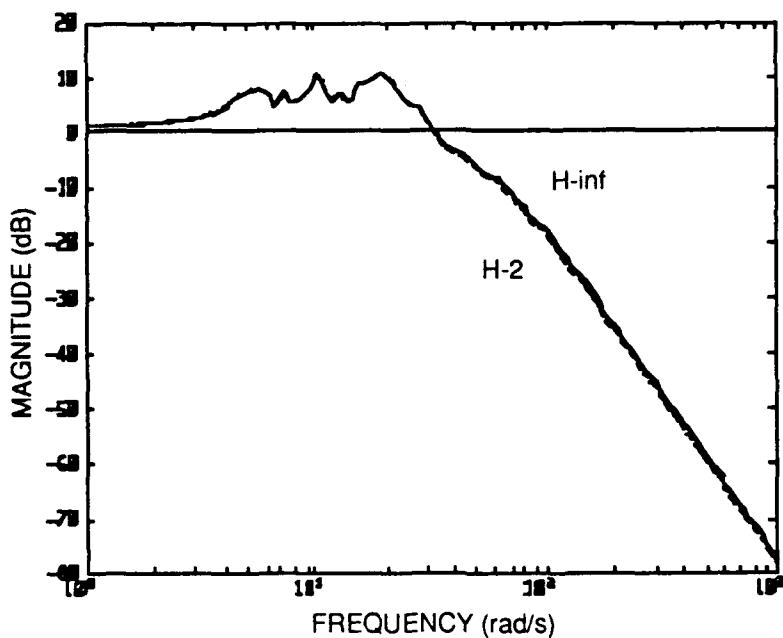
Figure 7.16 Complementary Sensitivity at Plant Output
(Robust Designs).

From this section, it can be seen that penalizing the control at all frequencies in the optimal control problem is effective in attaining closed-loop stability robustness, but results in an unacceptable degradation of system disturbance rejection performance, particularly at low frequencies. Alternate means of achieving stability robustness without greatly sacrificing achievable performance are therefore required. From Figure 7.15, it seems that what is needed is a methodology that induces the compensator to inject higher gain at low frequencies (thereby improving performance), while still forcing a fast roll-off of gain at high frequencies in order to meet the stability robustness constraint. This design objective suggests the use of frequency dependent design techniques, otherwise known as loop-shaping methods. Implementation of such design techniques is now addressed.

115

7.4 Loop-Shaping Designs

7.4.1 Introduction

In Section 5.4.3, a design methodology is presented involving augmentation of frequency dependent weighting functions to the error and/or control vector, followed by solution of either the H_2 or H_∞ Riccati equations in order to obtain a compensator realization. The details of application of these techniques are now presented. Section 7.4.2 describes a frequency weighted error vector H_2 design, and Section 7.4.3 describes a frequency weighted control vector H_∞ design. Augmentation of the plant dynamics with shaping filters is discussed for each design, followed by presentation of the same closed-loop frequency response plots as seen in Sections 7.1 and 7.2 for the unconstrained bandwidth and robust designs.

7.4.2 Weighted-Error H_2 Design

In Section 7.3 it was seen that the robust designs resulting from large control penalty at all frequencies degraded low frequency performance beyond allowable limits. Intuition suggests that by skillful formulation of a frequency weighted control problem, it should be possible to design a compensator that injects high gain at low frequencies and still rolls off quickly enough to be robustly stable. A means of employing this strategy utilizing weights on the error vector only is now pursued. Ignoring the controls portion of the error, the condition for meeting performance specifications reduces to

$$\| W_{\bar{c}}(s) \, T_{\bar{c}\,d}(s) \|_\infty \leq 1 \tag{7.4}$$

as discussed in Section 5.3.4. In light of the above discussion, (7.4) suggests that the frequency dependent weighting function (or shaping filter), $W_e(s)$, should be selected to be large at low frequencies and small at high frequencies. This can be interpreted as telling the optimal control problem to penalize the low frequency error more than the high frequency error, so that the compensator will focus its effort on and inject more gain into the low frequency region. Once a weighting function has been selected that possesses the above characteristics, a state-space realization is obtained, and the filter dynamics are augmented

to the open-loop 2-block model (6.11) as follows. Given a state-space realization for the shaping filter, $W_e(s)$,

$$W_e(s) = \left[\begin{array}{c|c} A_w & B_w \\ \hline C_w & D_w \end{array} \right]$$

the filter dynamics can be written

$$\dot{p}(t) = A_w\, p(t) + B_w\, \bar{e}(t)$$

$$e'(t) = C_w\, p(t) + D_w\, \bar{e}(t) \qquad (7.5)$$

Recalling that

$$\bar{e}(t) = c_2\, x(t)$$

the 2-block system for use in the Riccati equations becomes

$$\left[\begin{array}{c} \dot{x}(t) \\ \dot{p}(t) \end{array} \right] = \left[\begin{array}{cc} a & 0 \\ B_f c_2 & A_f \end{array} \right] \left[\begin{array}{c} x(t) \\ p(t) \end{array} \right] + \left[\begin{array}{c} b_2 \\ 0 \end{array} \right] d'(t) + \left[\begin{array}{c} b_3 \\ 0 \end{array} \right] u(t)$$

$$e'(t) = [D_f c_2 \quad C_f] \left[\begin{array}{c} x(t) \\ p(t) \end{array} \right] + d_{23}\, u(t)$$

$$y(t) = [c_3 \quad 0] \left[\begin{array}{c} x(t) \\ p(t) \end{array} \right] + d_{32}\, d'(t) \qquad (7.6)$$

A shaping filter must now be selected that accomplishes the above-stated goals. Note that there is a great deal of freedom in selecting such a shaping filter. Filter order, poles, zeros, and dc gain may all be varied by the designer. Consider (7.7), which shows the transfer function of a candidate single error shaping filter:

$$w(s) = \frac{\omega_b}{s + \omega_b} \qquad (7.7)$$

The filter of (7.7) is a simple, unity gain, first-order low-pass filter with break frequency ω_b. The MIMO weighting function, $W_e(s)$, resulting from applying (7.7) to all the system errors can be formed simply by obtaining a state-space realization for (7.7),

117

$$w(s) = \left[\begin{array}{c|c} a_w & b_w \\ \hline c_w & d_w \end{array}\right] = \left[\begin{array}{c|c} -\omega_b & \sqrt{\omega_b} \\ \hline \sqrt{\omega_b} & 0 \end{array}\right] \tag{7.8}$$

and defining $W_e(s)$ to be represented by

$$W_e(s) = \left[\begin{array}{c|c} a_w I_e & b_w I_e \\ \hline c_w I_e & 0 \end{array}\right] \tag{7.9}$$

where I_e is the square identity matrix with dimension equal to the number of errors, which is 16 in this case. The filter of (7.7) is first-order, and it therefore limits the increase in dimension incurred by augmenting the filter dynamics to the plant to an additional 16 states, one for each segment phasing and LOS error. The filter also has unity dc gain for simplicity. Such a choice for the structure of the error shaping filter reduces the number of parameters to be varied in the design process to two, namely the break frequency of the shaping filter, ω_b, and the scalar control weight, ρ. The design process can now be carried out by selecting various values for ω_b and ρ, obtaining a compensator, and evaluating closed-loop performance in an iterative fashion until a satisfactory design results.

Figures 7.17 and 7.18 show the closed-loop maximum singular value transfers from d to e for H_2 loop-shaped designs incorporating error shaping filters with break frequencies at 0.1 and 10 rad/s, respectively. The respective values of ρ for the two designs are 150 and 4000, arrived at by trial and error iteration until a robust design was achieved. Only the H_2 solutions are presented for the frequency weighted error designs, because augmenting unity gain error shaping filters was not found to significantly change the H_∞ closed-loop solutions from the non-filtered versions. From Figure 7.17 it can be seen that choosing ω_b to be 0.1 rad/s results in a significant improvement in low-frequency performance. In fact, performance specifications are met by this design up to ~2 rad/s. However, note that severe disturbance amplification now occurs in the 2 to ~40 rad/s frequency range. The infinity-norm of the T_{22} block for this design is more than 10 dB greater than that of the robust H_∞ design of Section 7.3 (22.3 dB versus 11.1 dB). This loop-shaped design therefore results in over three times as poor worst-case disturbance rejection. From Figure 7.18 it can be seen that moving the break frequency of the error shaping filter two decades to the right yields a design very similar to the robust designs seen in Section 7.3. Close examination of the figure, however, indicates that the low-

frequency performance of this design is somewhat better than that of the robust H_∞ design (3.1 dB versus 6.4 dB), and its performance transfer function infinity-norm is only slightly greater (13.8 dB versus 11.1 dB). The figures indicate that a tradeoff exists between low and high frequency performance, as determined by location of the shaping filter break frequency. For smaller values of ω_b, excellent low-frequency performance is attained, but worst-case performance suffers extensively. As ω_b gets larger, low-frequency performance degrades, but worst-case performance improves. From Figures 7.17 and 7.18, it does not appear that any choice of ω_b will result in achieving performance specifications at all frequencies. Since the low-frequency performance of the 0.1 rad/s ω_b design is so good, however, it does appear that an optimal choice of ω_b exists greater than 0.1 rad/s but less than 10 rad/s such that performance goals can be met for a large portion of the low-frequency range, and worst-case performance will not be degraded too severely.
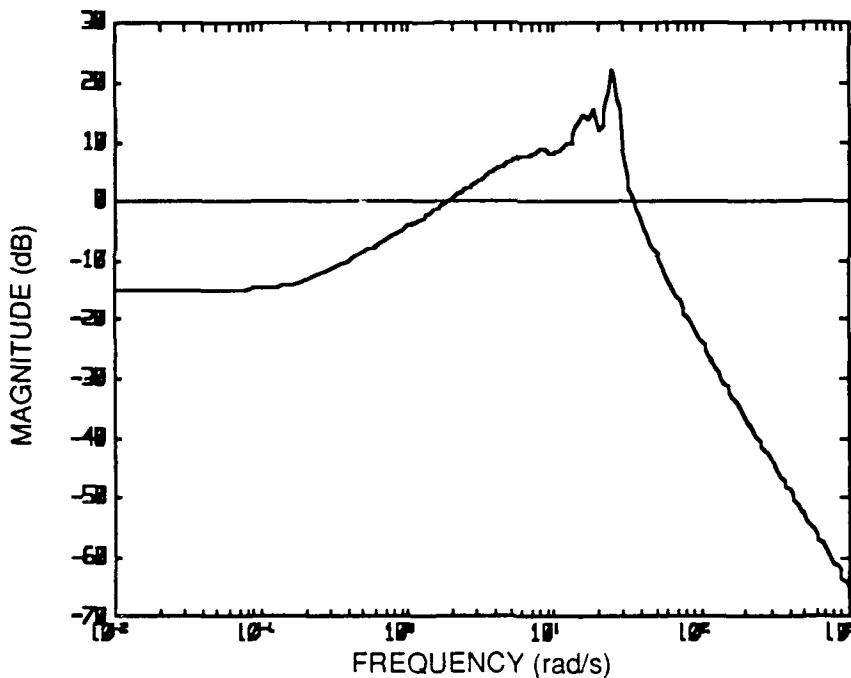
Figure 7.17 Closed-Loop Transfer from All Disturbances to All Errors (T_{22})
(Weighted-Error H_2 Design, ω_b = 0.1 rad/s).

119

MAGNITUDE (dB)

20

10

0

-10

-20

-30

-40

-50

-60

-70

10^0 10^1 10^2 10^3
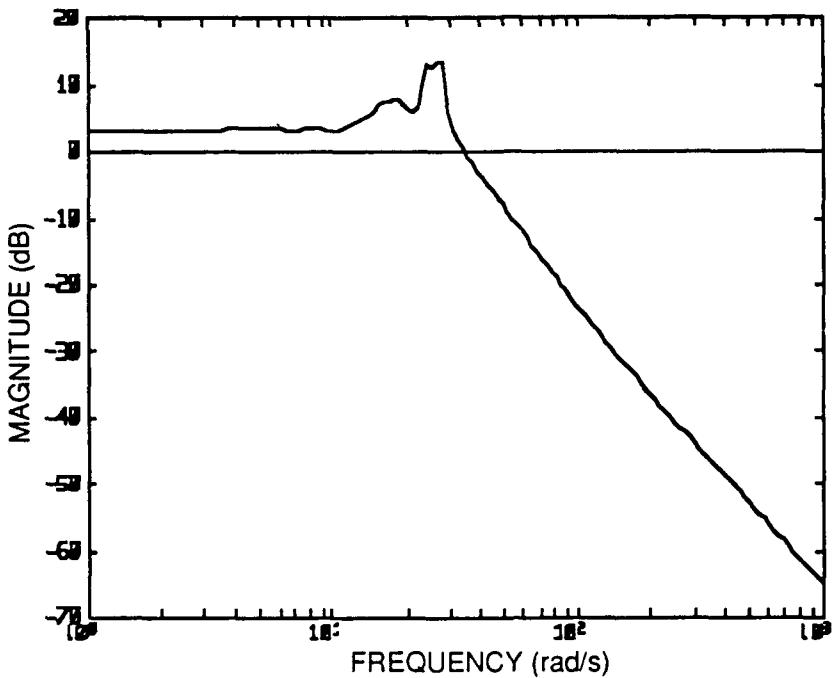
FREQUENCY (rad/s)

Figure 7.18 Closed-Loop Transfer from All Disturbances to All Errors (T_{22})
(Weighted-Error H_2 Design, $\omega_b = 10$ rad/s).

Figures 7.19 and 7.20 show the filter frequency response and closed-loop transfer from d to e for a weighted error H_2 design with break frequency at 2 rad/s and ρ value of 950. This design was obtained by trial and error iteration as the design that allowed performance specifications to be met over the greatest frequency range. From Figure 7.19, it can be seen that the shaping filter is indeed unity gain at low frequency, and rolls off at higher frequency (at ~2 rad/s). From Figure 7.20, this design can be seen to meet performance specifications for all frequencies less than 5 rad/s and greater than 35 rad/s, while degrading worst-case performance from the robust H_∞ design by only 3.1 dB. The H_2 loop-shaping methodology applied to the system errors thus allows significant improvement in overall performance over robust designs accomplished via pure bandwidth reduction (constant control penalty).

120
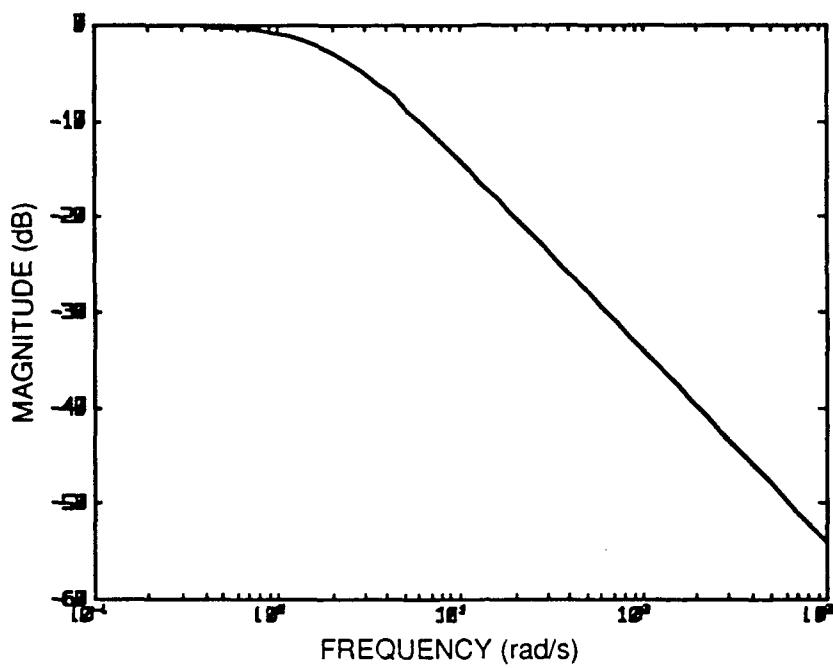
Figure 7.19 Error Shaping Filter Frequency Response
(Weighted-Error H_2 Design, ω_b = 2 rad/s).
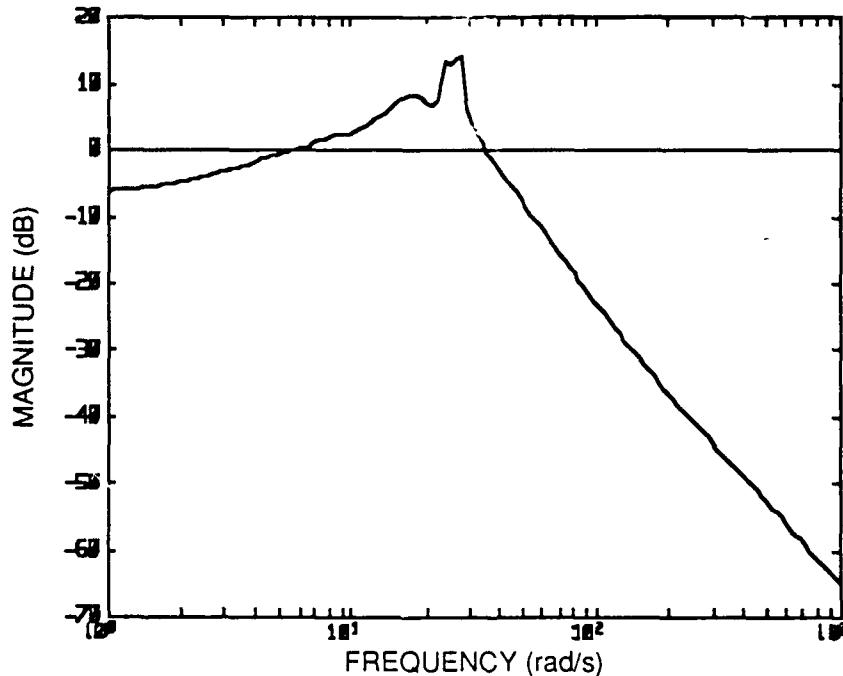
Figure 7.20 Closed-Loop Transfer from All Disturbances to All Errors (T_{22})
(Weighted-Error H_2 Design, ω_b = 2 rad/s).

Figures 7.21-7.25 show the maximum singular value frequency responses of the T_{11}, and T_{22} subblocks of the H_2 loop-shaped error design for comparison with the previous designs. As can be seen from Figure 7.21, the weighted-error H_2 design is indeed robust to the truncated high-frequency dynamics modeled at the plant output. From Figures 7.22-7.25, it appears that the transfer from the disturbance torques to the segment phasing errors is driving achievable performance over most of the frequency range of interest, but the maximum transfer occurs between the disturbance torques and the LOS errors. Also, of the four transfer functions, only the transfer from the measurement noise to the LOS errors meets performance specifications at all frequencies.
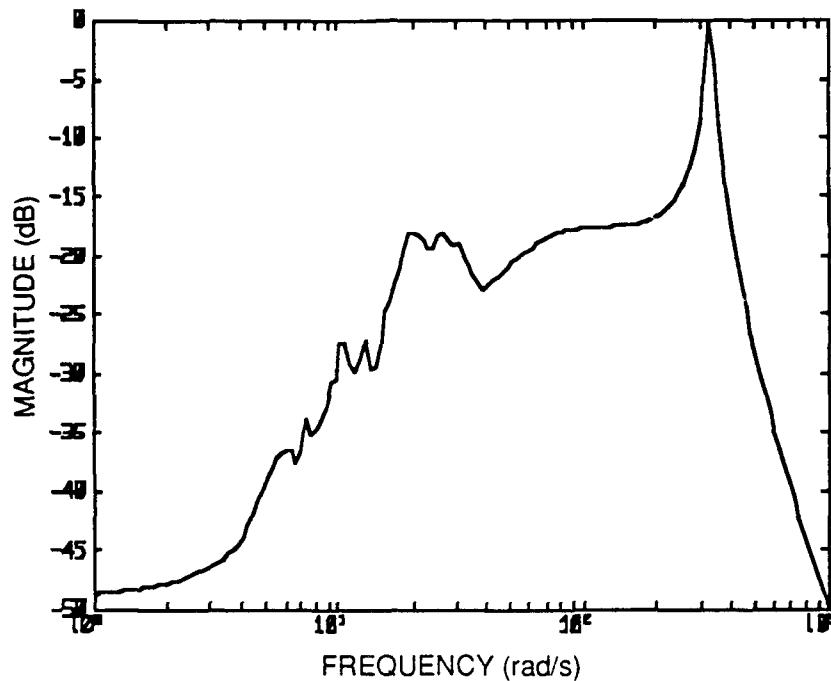
Figure 7.21 Closed-Loop Transfer about Δ_M (T_{11})
(Weighted-Error H_2 Design, $\omega_b = 2$ rad/s).

122
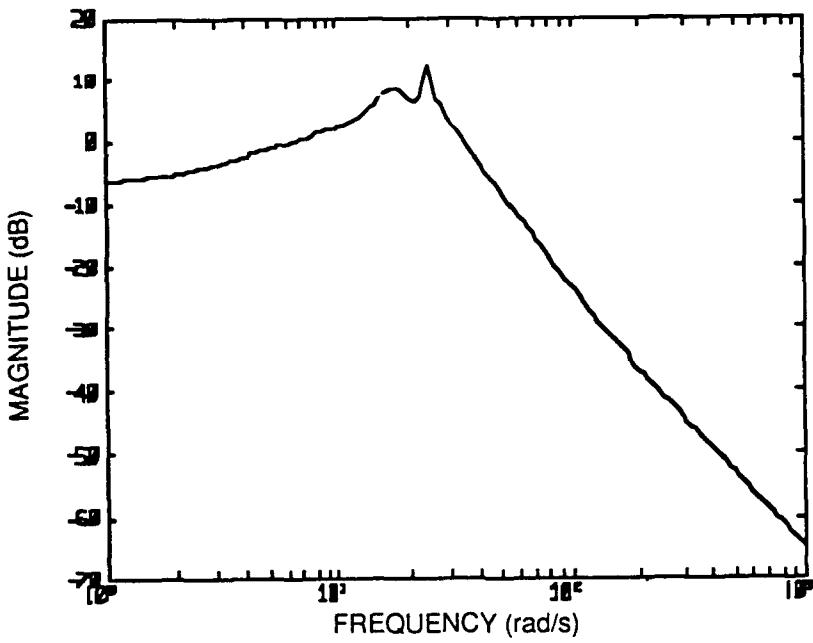
Figure 7.22 Max. Singular Value Closed-Loop Transfer from
Torque Disturbances to Segment Phasing Errors (T_{2211})
(Weighted-Error H_2 Design, ω_b = 2 rad/s).
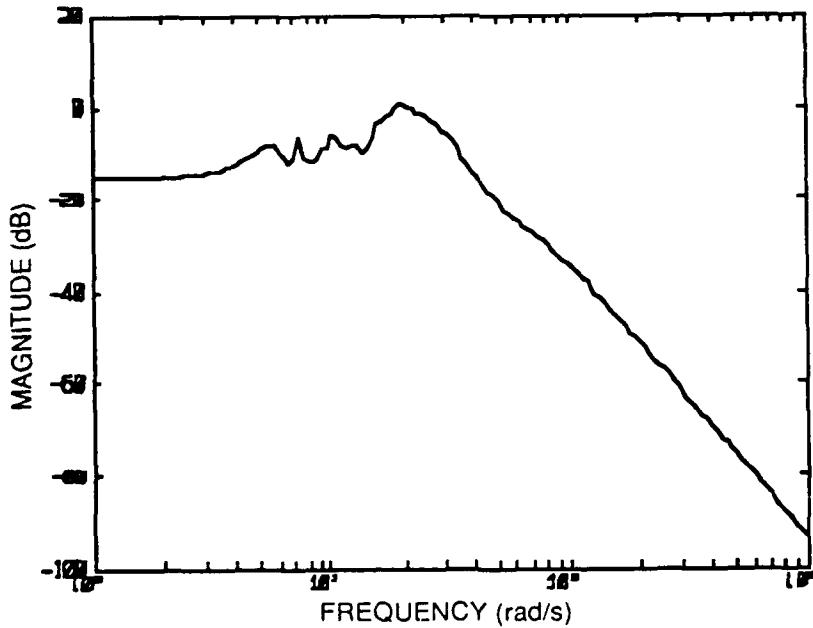
Figure 7.23 Max. Singular Value Closed-Loop Transfer from
Sensor Noise to Segment Phasing Errors (T_{2212})
(Weighted-Error H_2 Design, ω_b = 2 rad/s).

123
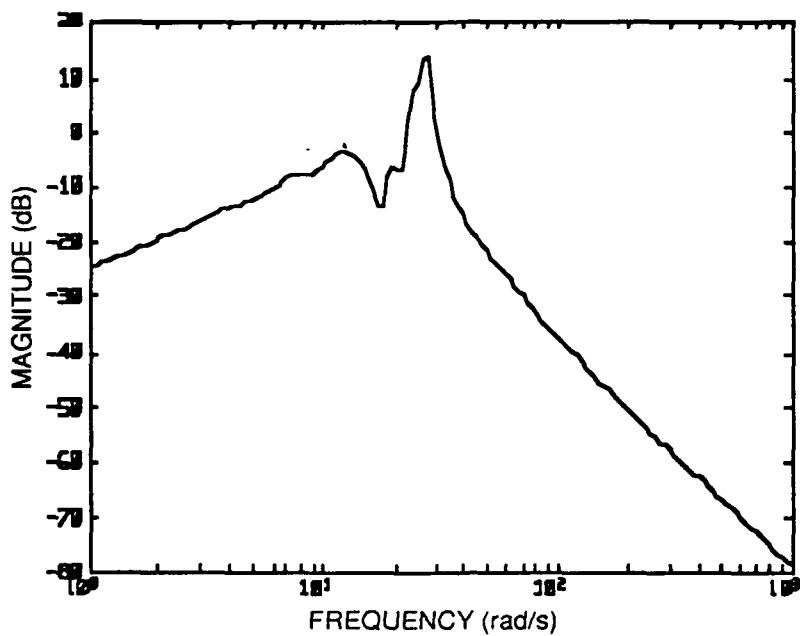
Figure 7.24 Max. Singular Value Closed-Loop Transfer from
Torque Disturbances to Line-of-Sight Errors (T_{2221})
(Weighted-Error H_2 Design, ω_b = 2 rad/s).
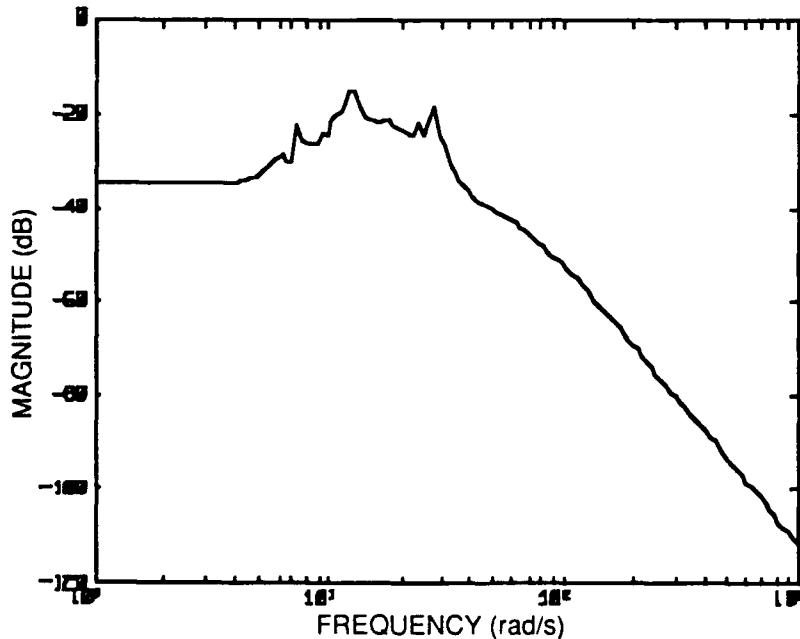
Figure 7.25 Max. Singular Value Closed-Loop Transfer from
Sensor Noise to Line-of-Sight Errors (T_{2222})
(Weighted-Error H_2 Design, ω_b = 2 rad/s).

124

Figure 7.26 shows the maximum singular value frequency response of the H_2 loop-shaped error design compensator. By comparing Figure 7.26 with Figure 7.15 , it can be seen that the H_2 loop-shaped compensator frequency response is very similar to the frequency response of the robust design compensators for frequencies greater than 10 rad/s. This explains why the high-frequency behavior of the loop-shaped design, and, hence, its worst-case performance, is not significantly different than that of the robust designs. However, note that the loop-shaped compensator injects ~15 dB higher gain at low frequencies than do the robust design compensators. This is what allows the H_2 loop-shaped design to meet performance specifications at low frequencies, while the robust designs do not. Recall that the H_2 loop-shaped compensator possesses 16 more states than do the robust design compensators, due to the augmented dynamics of the error shaping filter. It is these additional states which act at low frequency to yield the difference in performance between designs.
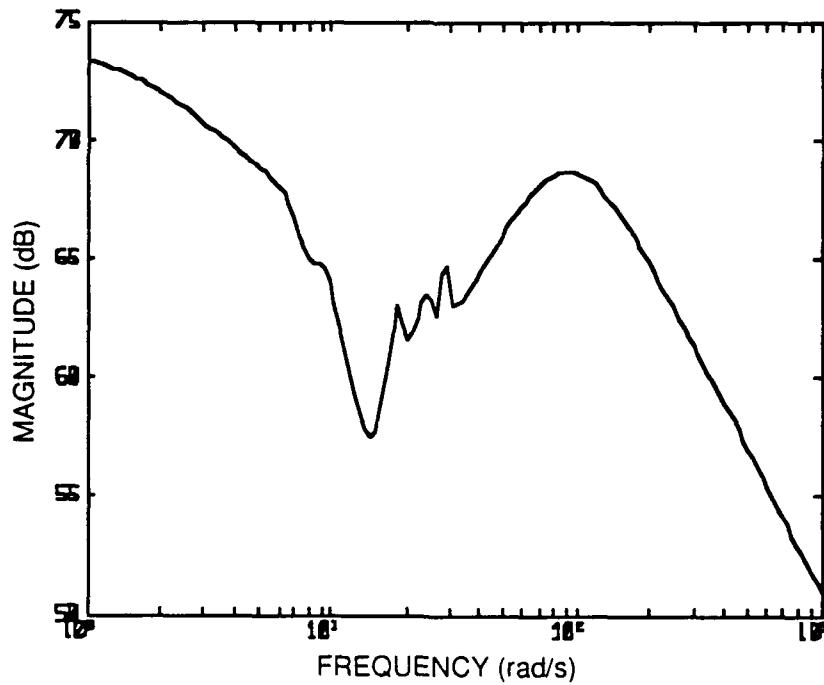
Figure 7.26 H_2 Loop-Shaped Error Compensator
Maximum Singular Values.

Seeing that the high-frequency behavior of the H_2 loop-shaped compensator is not tremendously different than that of the robust designs, it is expected that the bandwidths of

125

the designs should also be similar. Figure 7.27 shows the maximum singular value frequency response of the complementary sensitivity at the plant output, $C_o(j\omega)$, for the H_2 loop-shaped error design. The bandwidth of this design is 42 rad/s, as compared to a bandwidth of 36 rad/s for the robust designs. The H_2 loop-shaped error design is thus slightly faster, but not significantly more so, than the robust designs of Section 7.3.
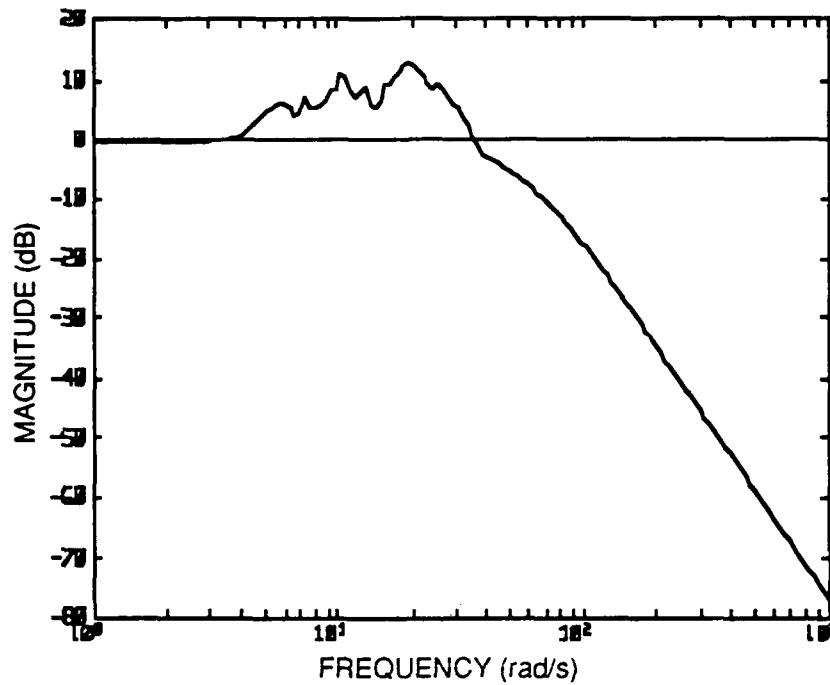
Figure 7.27 Complementary Sensitivity at Plant Output
(Weighted-Error H_2 Design, $\omega_b = 2$ rad/s).

In this section, it has been shown that the technique of augmenting frequency dependent weighting functions to the system performance variables, in combination with H_2 optimal control, allows realization of a robust, 72-state compensator that exhibits significantly superior performance to the robust designs accomplished via bandwidth reduction in Section 7.3. However, the H_2 loop-shaped error design obtained is not successful in meeting prescribed performance specifications at all frequencies. From Figures 7.17-7.20, it would appear that the H_2 error shaping methodology will not allow a sufficiently fast roll-off of gain to let us achieve performance goals above 5 rad/s, and still meet the stability robustness constraints of the Small Gain Theorem. Since frequency dependent actuation seems to be the key to this problem, intuition suggests that perhaps more success could be obtained by shaping the control directly, rather than relying on

126

penalization of the errors. Therefore, an alternative method of applying loop-shaping techniques involving frequency dependent penalty of the control, u, is now addressed.

Section 7.4.3   Weighted-Control H_∞ Design

As deduced in the previous section, the compensator designs obtained to this point suggest the shape of an "ideal" compensator response for the BEA segment phasing/jitter control problem. In order to meet performance specifications, it appears that a design methodology is needed which produces a compensator that injects high gain up to a certain critical frequency, and then rolls off very quickly so as to meet the stability robustness test of the Small Gain Theorem. The crucial problem, then, is how to directly effect the shape of this desired compensator. Since the frequency response of the control and the compensator are directly proportional (u = Ky), it would appear that by shaping the frequency response of the control, we should be able to shape the frequency response of the compensator to a large extent. Fortunately, the system performance vector contains the system control as well as segment phasing and LOS errors, so that the loop-shaping methodology previously discussed may be conveniently applied to this compensator shaping problem by focusing on the controls portion of the error vector. As discussed in Section 5.3.4, performance objectives for the appropriately scaled weighted-control loop-shaping problem can be posed as

$$\| T_{ud}(s) \|_\infty \leq \frac{1}{\| W_u(s) \|_\infty}$$

(7.10)

In order to obtain the compensator frequency response shape described above, (7.10) indicates that the control weighting function, $W_u(s)$, should be selected so as to be small at low frequency and large at high frequency. Choosing the weighting function in this manner forces the control to be high at low frequency and roll-off quickly at high frequency as desired. It is interesting to note that the shape of the control weighting function specified here is the inverse of the shape of the error weighting function used in Section 7.4.2.

Once a state-space realization is obtained for the control shaping filter,

$$W_u(s) = \left[\begin{array}{c|c} A_w & B_w \\ \hline C_w & D_w \end{array} \right]$$

127

then the filter dynamics can be written

$$\dot{p}(t) = A_w\, p(t) + B_w\, u(t)$$

$$u'(t) = C_w\, p(t) + D_w\, u(t) \tag{7.11}$$

The augmented plant is represented by

$$\begin{bmatrix} \dot{x}(t) \\ \dot{p}(t) \end{bmatrix} = \begin{bmatrix} a & 0 \\ 0 & A_f \end{bmatrix}\begin{bmatrix} x(t) \\ p(t) \end{bmatrix} + \begin{bmatrix} b_2 \\ 0 \end{bmatrix} d'(t) + \begin{bmatrix} b_3 \\ B_w \end{bmatrix} u(t)$$

$$\begin{bmatrix} e'(t) \\ u'(t) \end{bmatrix} = \begin{bmatrix} c_2 & 0 \\ 0 & C_w \end{bmatrix}\begin{bmatrix} x(t) \\ p(t) \end{bmatrix} + \begin{bmatrix} 0 \\ D_w \end{bmatrix} u(t)$$

$$y(t) = \begin{bmatrix} c_3 & 0 \end{bmatrix}\begin{bmatrix} x(t) \\ p(t) \end{bmatrix} + d_{32}\, d'(t) \tag{7.12}$$

and solution of the Riccati equations may proceed. Selection of an appropriate control *weighting function is now addressed.*

In order to again keep the number of design parameters and additional model states small, the following form for the single control weighting function is adopted:

$$w_u(s) = k\,\frac{(s + z)}{z}\,\frac{p}{(s + p)} \tag{7.13}$$

Such a SISO shaping filter is first-order, with a simple pole at frequency p, zero at frequency z, and dc gain k. There are therefore three design parameters for the weighted-control problem. As in the weighted-error design, once a state-space realization is obtained for (7.13),

$$w_u(s) = \left[\begin{array}{c|c} a_w & b_w \\ \hline c_w & d_w \end{array} \right]$$

the 24-input, 24-output control-weighting function is obtained by letting

$$W_u(s) = \left[\begin{array}{c|c} a_w\,I_{24} & b_w\,I_{24} \\ \hline c_w\,I_{24} & d_w\,I_{24} \end{array} \right]$$

The design process is then carried out by selecting various values for z, p, and k, until a robust design that meets performance specifications is obtained.

Figure 7.28 shows the maximum singular value frequency response of a control shaping filter with a zero at s = -5 rad/s, a pole at s = -500 rad/s, and a dc gain of 77. From the figure it can be seen that the shape of this frequency response is indeed the "inverse" of the shape of the error shaping filter frequency response used in the previous section's loop-shaped H_2 design (recall Figure 7.19), in that the control filter response is small at low frequency and large at high frequency. Also note that the control shaping filter zero frequency is slightly greater than the error shaping filter pole frequency, so that the weighted-control H_∞ design does not penalize the system controls at as low a frequency as the weighted-error H_2 design penalized the performance variables. Figure 7.29 shows the frequency response of the T_{22} block of the H_∞ design obtained from controller synthesis using the augmented plant associated with this control shaping filter. From Figure 7.29 it can be seen that the design meets closed-loop performance specifications at all frequencies, and it seems that the intuition which has led us to this point has been justified. As with the H_2 loop-shaped error design, this design was arrived at via trial and error iteration with the design parameters (z, p, and k). Only the H_∞ design results are presented for the loop-shaped controls technique, because the H_2 designs resulting from this method were almost identical with the H_∞ design, just as seen in the reduced bandwidth designs of Section 7.3. As was the case for the robust designs, the H_∞ loop-shaped control solutions yielded slightly smaller infinity-norms than the H_2 solutions, and, for the sake of brevity, only the best H_∞ design is therefore presented.
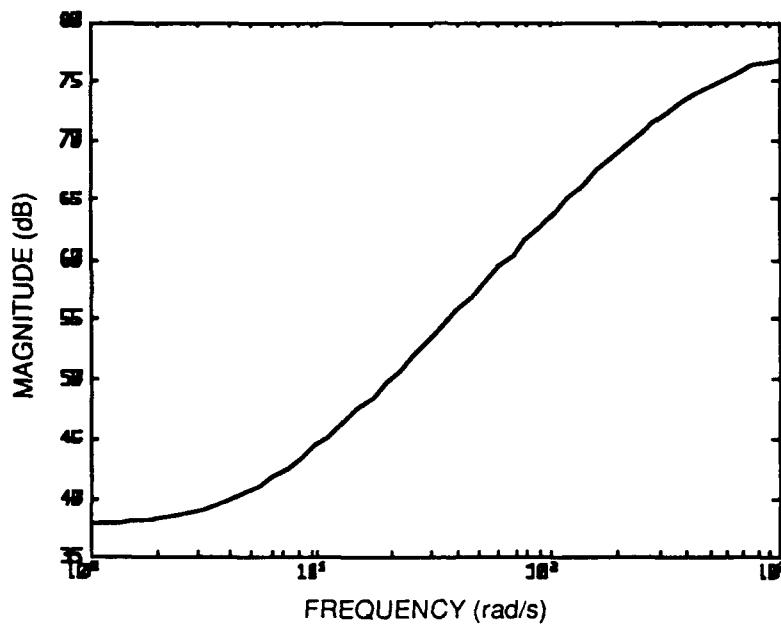
Figure 7.28 Control Shaping Filter Frequency Response.
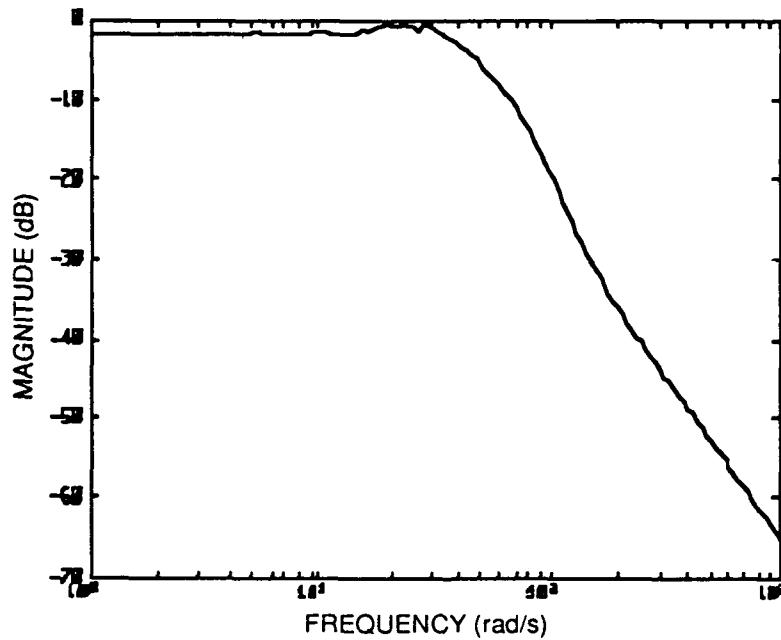
Figure 7.29 Closed-Loop Transfer from All Disturbances to All Errors (T_{22})
(Weighted-Control H_∞ Design).

130

Figure 7.30 shows the maximum singular value frequency response of the T_{11} block of the weighted-control H_∞ design, and Figures 7.31-7.34 show the frequency responses for the four subblocks of the T_{22} transfer function. As can be seen from Figure 7.30, the closed-loop transfer about the delta block has infinity-norm less than 1 (0 dB), so the H_∞ loop-shaped control design is indeed robust to the modeled uncertainty. Figure 7.31 indicates that the transfer from the torque disturbances to the segment phasing errors is driving performance of the design, and, of course, all the other subblock frequency responses are seen to have infinity-norms less than 1 (0 dB).
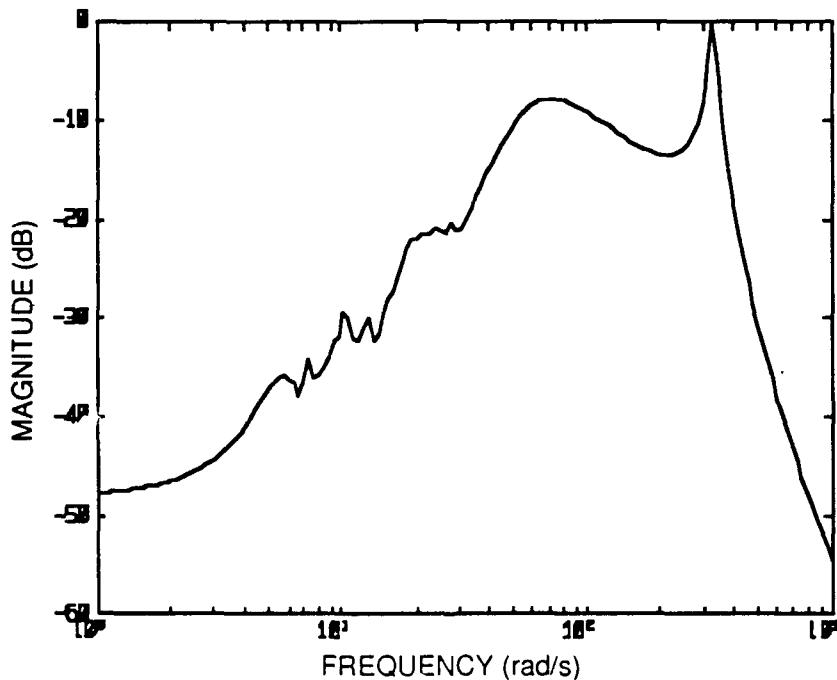
Figure 7.30 Closed-Loop Transfer about Δ_M (T_{11})
(Weighted-Control H_∞ Design).

131
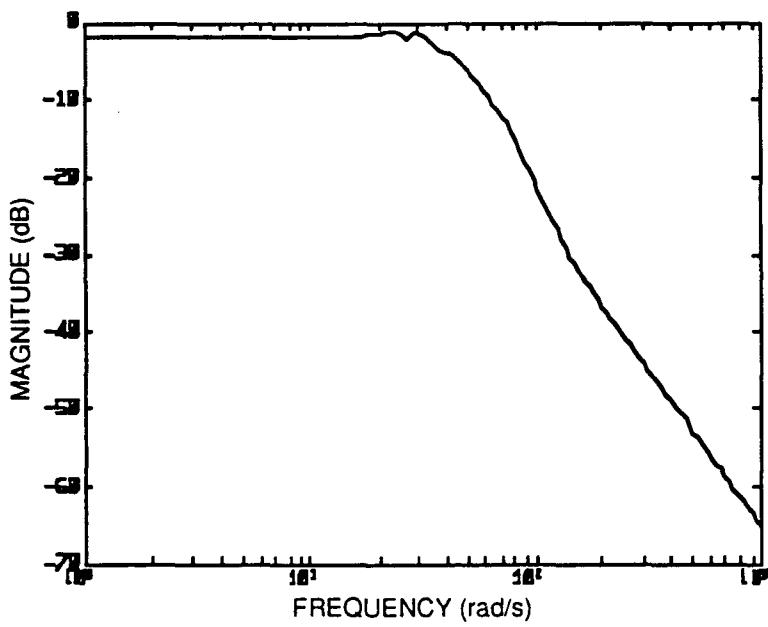
Figure 7.31 Max. Singular Value Closed-Loop Transfer from
Torque Disturbances to Segment Phasing Errors (T_{2211})
(Weighted-Control H_{∞} Design).
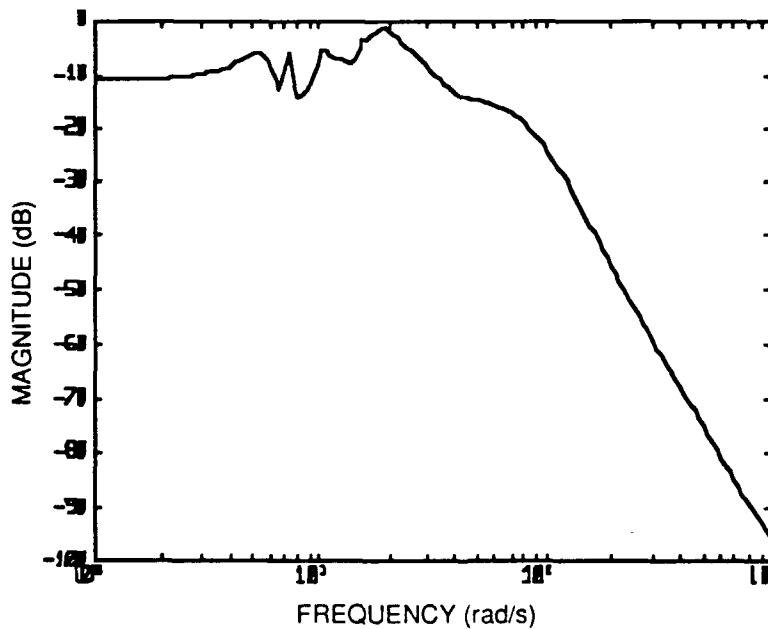
Figure 7.32 Max. Singular Value Closed-Loop Transfer from
Sensor Noise to Segment Phasing Errors (T_{2212})
(Weighted-Control H_{∞} Design).

132
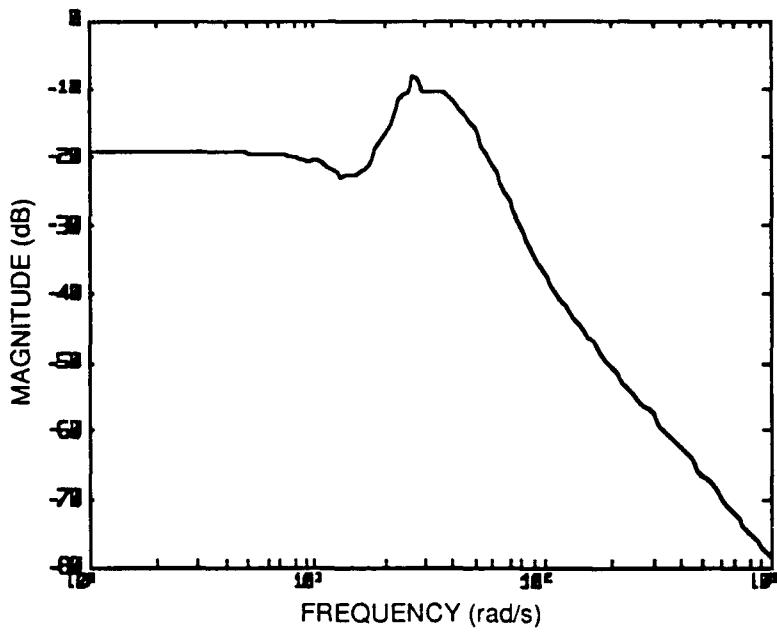
Figure 7.33 Max. Singular Value Closed-Loop Transfer from
Disturbance Torques to Line-of-Sight Errors (T$_{2221}$)
(Weighted-Control H$_\infty$ Design).
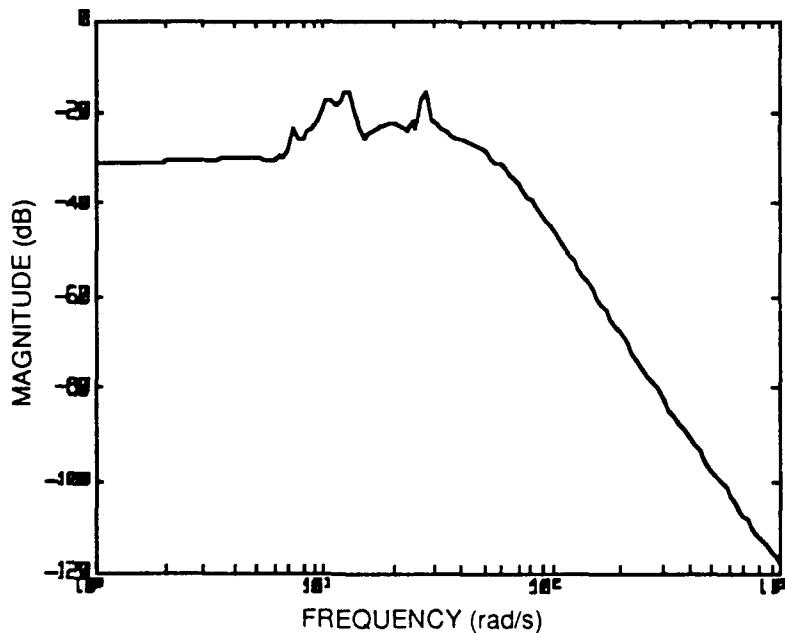
Figure 7.34 Max. Singular Value Closed-Loop Transfer from
Sensor Noise to Line-of-Sight Errors (T$_{2222}$)
(Weighted-Control H$_\infty$ Design).

133

Figure 7.35 shows the maximum singular value frequency response of the weighted-control H_∞ design compensator. The most significant difference between the frequency response of this compensator and the H_2 loop-shaped error compensator response is the high gain maintained by the H_∞ compensator over the frequency band from about 5 to 100 rad/s. This is what allows the H_∞ loop-shaped control compensator to meet performance specifications in the frequency range where the H_2 loop-shaped error compensator could not. Additionally, the maximum singular values of the H_∞ loop-shaped control compensator are about 7 to 8 dB greater than those of the H_2 loop-shaped error compensator in the frequency bands both above and below this critical region. It is the ability of the H_∞ loop-shaped control compensator to preserve high gain in the high frequency region and still roll-off fast enough to meet the stability robustness constraint that is especially crucial to the success of this design. Finally, Figure 7.35 indicates that there is a region of particularly high compensator gain between ~18 and 30 rad/s, including what appears to be a very lightly damped compensator pole at about 28 rad/s. The obvious presence of this pole seems to indicate that the compensator is performing some type of critical pole-zero cancellation of the plant dynamics at about 28 rad/s, in order to extend the design's disturbance rejection capability to higher frequencies.
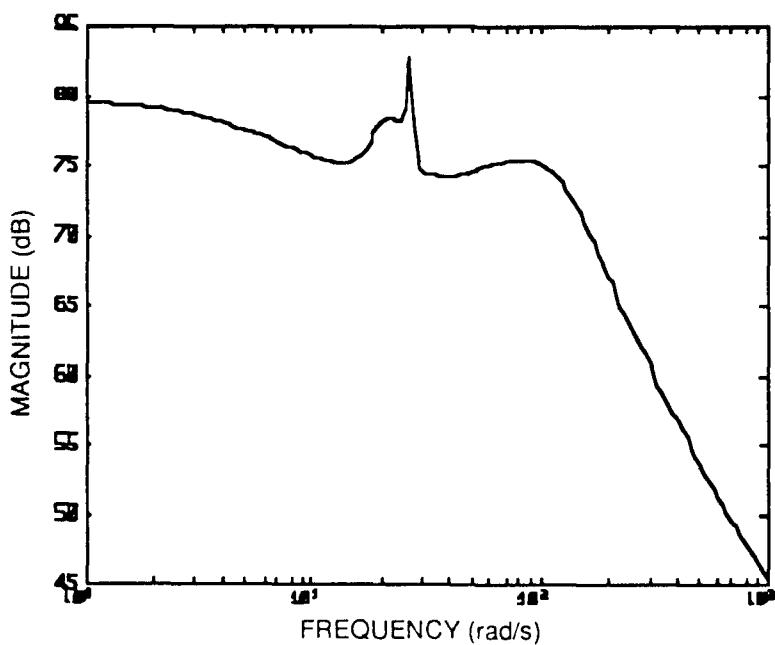
Figure 7.35 H_∞ Loop-Shaped Control Compensator
Maximum Singular Values.

134

Figure 7.36 shows the maximum singular value frequency response of the complementary sensitivity at the plant output for the weighted-control H_∞ design. Since the H_∞ loop-shaped control compensator is so effective at preserving high gain at high frequencies, we should expect the bandwidth of this design to be significantly higher than that of the other robust designs. From Figure 7.36 it can be seen that this is indeed the case. The bandwidth of the H_∞ loop-shaped control design is 80 rad/s, which is almost twice as large as the bandwidth of the weighted-error H_2 design. The H_∞ loop-shaped control design should therefore be expected to have a significantly quicker time response than any of the previous robust designs. Note that the H_∞ loop-shaped control design bandwidth still falls considerably short of the 160-180 rad/s bandwidths exhibited by the unconstrained bandwidth designs of Section 7.2, but the H_∞ loop-shaped control design is robust to the unmodeled high-frequency dynamics, while the unconstrained bandwidth designs were not.
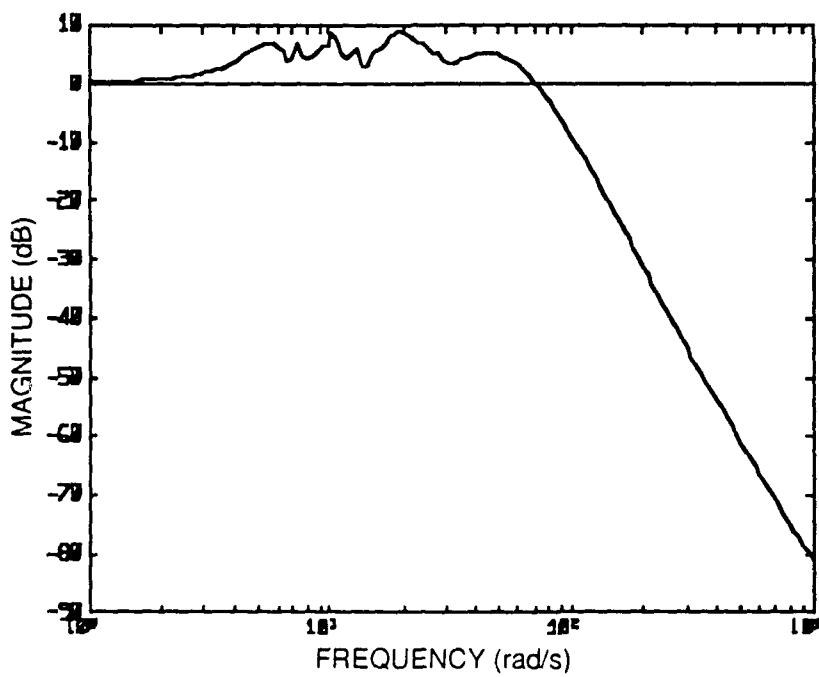
Figure 7.36 Complementary Sensitivity at Plant Output
(Weighted-Control H_∞ Design).

From the results presented in this chapter, it is obvious that the H_∞ loop-shaped control compensator design is the best design for the BEA segment phasing/jitter control problem.

135

Of all the design methods applied, only the H_∞ loop-shaped control compensator yields a closed-loop system that meets d to e transfer infinity-norm performance specifications, and is simultaneously robust to the high-frequency dynamics truncated in the model reduction process. Additionally, the H_∞ loop-shaped control compensator design is of significantly higher bandwidth than any of the other robust designs considered. The added flexibility and power of loop-shaping design methods over traditional optimization techniques are therefore demonstrated. The only disadvantage of the H_∞ loop-shaped control compensator is that it is of higher order than any of the other compensators designed (80 states for the H_∞ loop-shaped control compensator versus 72 for the loop-shaped error H_2 compensator or 56 for the robust H_2/H_∞ designs), and is therefore more cumbersome to implement. However, reduction of compensator order may be possible, allowing this problem to be somewhat alleviated.

A successful design for the BEA segment phasing/jitter control problem set forth in this thesis has now been obtained. As a final step in the control system synthesis procedure, certain issues, such as possible implementation methods and associated requirements, remain to be addressed in order to verify the practicality of the proposed design. Also, control system designs are typically validated via time domain simulation. In this way, it can be verified whether the design actually meets specified performance goals, and other interesting closed-loop system characteristics may be observed. Finally, performance robustness issues, or expectations of performance under reasonable types of uncertainties, are well to consider. All of these implementation/design validation issues are pursued in Chapter 8.

CHAPTER 8

Implementation/Validation Issues

8.1 Introduction

This chapter addresses several topics which fall under the heading of practical implementation/design validation issues. Section 8.2 presents a standard framework for digital implementation of continuous time compensators like those designed in Chapter 7, and discusses several relevant issues arising from the analog to digital conversion process. Section 8.3 illustrates the details of application of Moore's Balance and Truncate model reduction algorithm to the task of simplifying the 80th order compensator derived for the BEA segment phasing/jitter control problem in Chapter 7. In Section 8.4, open and closed-loop simulations using both deterministic and stochastic disturbance inputs are performed, and results of steady-state covariance analyses are presented for the stochastic disturbance scenarios. Finally, Section 8.5 addresses concerns regarding performance robustness and the effects of parametric uncertainty of the open-loop plant model natural frequencies on closed-loop system stability.

8.2 Digital Implementation Issues

The compensator design methodologies presented in Chapter 5 and applied to the BEA segment phasing/jitter control problem in Chapter 7 assume a continuous-time (C-T) framework of operation for all system elements as shown in Figure 8.1. While this assumption is generally valid for the plant, $G(s)$, realistic compensator implementation scenarios call for control algorithms to be executed by a digital computer, which operates

137

on a discrete-time (D-T) basis. Implementation requirements therefore necessitate that the C-T BEA segment phasing/jitter control compensator designed in Chapter 7 somehow be converted to the D-T domain. Consider Figure 8.2, which depicts a standard framework for accomplishing this analog to digital conversion. Note that in Figure 8.2, the C-T compensator of Figure 8.1 has been replaced with a D-T equivalent compensator, which consists of a low-pass pre-filter (PF), a sampling mechanism with period T, a D-T (digital) compensator, D(z), and a zero-order-hold (ZOH) element in series. The operation of the D-T equivalent compensator can be summarized as follows. The C-T output signal, y, enters the low-pass pre-filter, whose break frequency (recall the discussion of low-pass filters in Section 7.4.2) is selected so as to correspond to the closed-loop bandwidth, ω_m. The purpose of this pre-filtering is to eliminate any spurious high-frequency noise which may be present in the non-ideal system, thereby ensuring that the frequency of the "fastest" signal that reaches the sampler is known. This is important because the sampling period, T, is selected based on this fastest frequency, so as to satisfy the requirements of the Sampling Theorem [21][7]. The pre-filtered signal is then sampled every T seconds, yielding a discrete sequence of numbers upon which the D-T compensator (computer) can act. Next, the D-T compensator, which is a function of the complex variable,

$$z = e^{-sT}$$

utilizes the current and past sampled output values and the control algorithm software programmed into the computer to generate new D-T command values. Finally, the zero-order-hold takes these numerical values and holds them constant over the sampling interval, thereby creating a C-T control signal to be fed into the plant.

---

[7] With the system bandwidth given by ω_m, the Sampling Theorem states that the sampling period should be selected so as to satisfy

$$T < \frac{\pi}{\omega_m}$$

The Sampling Theorem provides a theoretical upper bound on T so as to prevent sampled high-frequency signals from being interpreted as low-frequency signals, a phenomenon known as aliasing [21]. In practice, however, the sampling period is usually selected so as to be 10 to 20 times faster than indicated by the Sampling Theorem.
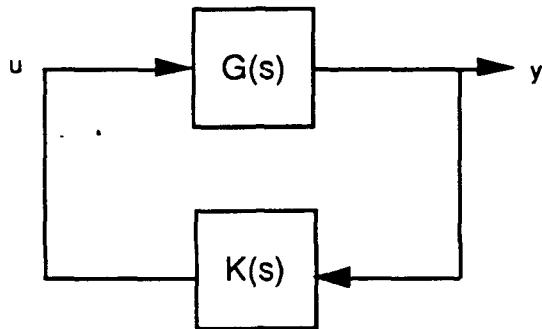
Figure 8.1 Open-Loop System with C-T Compensator.
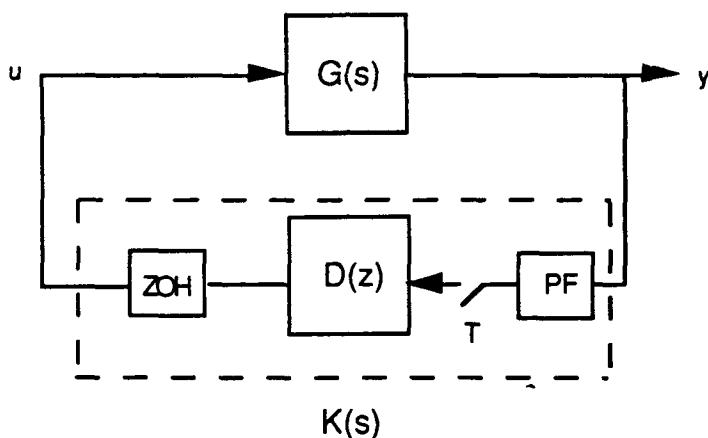
Figure 8.2 Open-Loop System with D-T Equivalent Compensator.

A number of important issues arise as a consequence of adopting this commonly used compensator implementation scheme. As the preceding discussion indicates, one particulary important issue is that the sampling period must be selected so as to be significantly "faster" than the system closed-loop bandwidth, ω_m. Very high bandwidth systems therefore require extremely small sampling periods, sometimes so small that the limitations of available sampling hardware come into play. For systems of this sort, the problem of not being able to sample fast enough can be further exacerbated by the fact that the length of the sampling interval also depends on the amount of computation and signal processing time required by the computer to generate new command values. Since computation time is directly proportional to the number of operations performed, higher dimensional compensators require more processing time than lower order alternatives. Writing efficient code and reducing compensator order to the lowest level possible is therefore a must.

139

Another issue that arises is conversion of the C-T compensator differential equations into D-T difference equations suitable for use in a digital computer. Methods of making such conversions are well-known and not particularly difficult to implement. The standard way in which this is accomplished for the system of Figure 8.2 is as follows. Given a state-space realization for the C-T compensator,

$$K(s) = \left[\begin{array}{c|c} A_k & B_k \\ \hline C_k & 0 \end{array}\right]$$

(8.1)

the D-T finite-difference equivalent state-space representation is given by [21]

$$D(z) = \left[\begin{array}{c|c} \Phi & \Gamma \\ \hline C_k & 0 \end{array}\right] = \left[\begin{array}{c|c} e^{A_k T} & A_k^{-1}\left[e^{A_k T} - I\right] B_k \\ \hline C_k & 0 \end{array}\right]$$

(8.2)

A number of remarks concerning (8.2) are in order. First, (8.2) clearly illustrates the effect the sampling period has on the D-T compensator equations. Second, (8.2) also indicates that the D-T compensator is of the same order as the C-T compensator. Since programming languages operate on a bit level and cannot perform matrix arithmetic, scalar equations must be coded for each compensator state. Thus, it can clearly be seen that higher-order compensators result in longer computation times, motivating the use of model reduction techniques on controller realizations.

An attempt is now made to identify how the above issues directly affect the BEA segment phasing/jitter control problem. Recalling that the loop-shaped H_∞ design selected in Chapter 7 had a bandwidth of 80 rad/s, the Sampling Theorem calls for a sampling period of no greater than 39.27 milliseconds. In practice, however, sampling periods 10 to 20 times faster than that called for by the Sampling Theorem are often used, so that a more likely value for T is 4 milliseconds. Such a sampling period is quite small, but not beyond the level reasonably achievable by modern sampling equipment. However, the effect of the high compensator dimensionality on the required sampling interval mentioned above has not been accounted for, and could present significant problems. As mentioned above, reduction of compensator order can help to alleviate this problem, and shall therefore now be addressed.

8.3 Reduction of Compensator Order

As discussed in Chapter 4, Moore's Balance and Truncate model reduction algorithm provides a convenient and intuitive method for attacking the problem of reducing model order. Using the B&T technique, uncontrollable/unobservable states are easily identified on the basis of small Hankel Singular Values (HSVs), and may then be removed from the system model. This section illustrates the details of application of the B&T model reduction technique to the 80-state H_∞ loop-shaped control compensator model obtained in Section 7.4.3. The primary objective is to reduce compensator model order as much as possible, while still meeting the infinity-norm performance specifications established for the BEA segment phasing/beam jitter control system.

Figure 8.3 shows the Hankel Singular Values of the H_∞ loop-shaped control compensator model versus state dimension. From the figure it can be seen that the magnitudes of the compensator HSVs decrease somewhat gradually up to about the 70-state level, at which point a sharp drop-off in magnitude occurs. Such a sharp break in the curve indicates that several of the compensator states above the 70 point level are significantly more uncontrollable/unobservable than the first 70 states, and may possibly be deleted without seriously affecting closed-loop performance in an adverse manner. Based on this assumption, reduced-order compensator models of various dimension were generated, and the resulting closed-loop performance was evaluated until the lowest order controller which still met performance specifications was obtained.
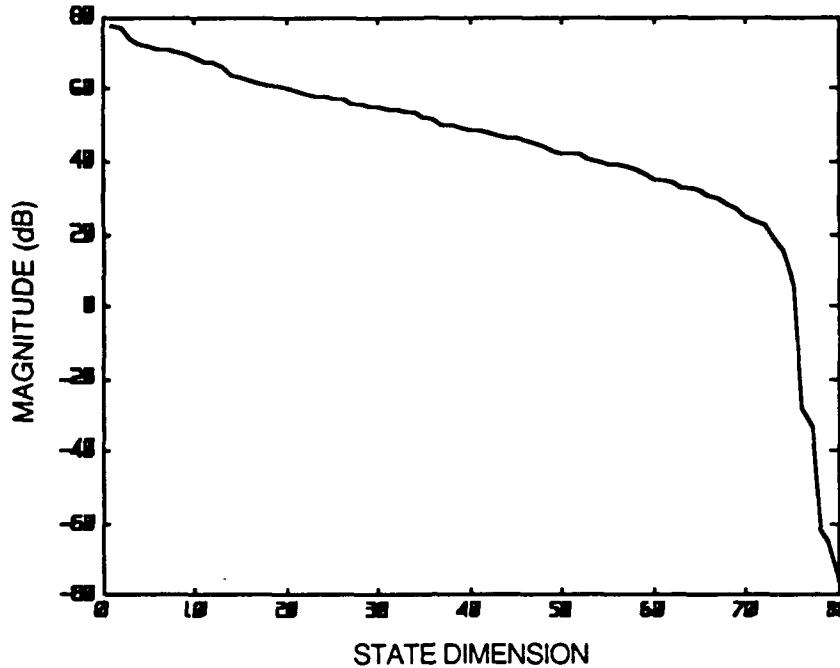
Figure 8.3 H∞ Loop-shaped Control Compensator Hankel Singular Values
versus State Dimension.

Figure 8.4 shows the maximum singular value closed-loop transfer from d to e for a system incorporating a 72-state compensator ROM. Since the infinity-norm of this transfer function can be seen to exceed 0 dB, such a reduced-order compensator obviously does not result in achieving performance specifications (albeit over a very small frequency range), and is therefore unacceptable. On the other hand, consider Figure 8.5, which shows the maximum singular value closed-loop transfer from d to e for a system incorporating a 73-state compensator ROM, as well as for the full 80-state controller realization. From this figure it can be seen that the 73-state compensator does what the 72-state compensator can not, namely achieve a pole-zero cancellation at ~4.8 rad/s so that performance specifications are met. It can also be seen from Figure 8.5 that there is very little difference between the closed-loop transfers resulting from use of a 73 versus 80-state controller model, the main contrast being several small bumps in the 73-state compensator system low-frequency response that are not present in the full order compensator system response. Thus, the 73rd compensator state can be seen to be the crucial one in terms of achieving performance goals, and the 73-state controller realization may therefore be adopted.
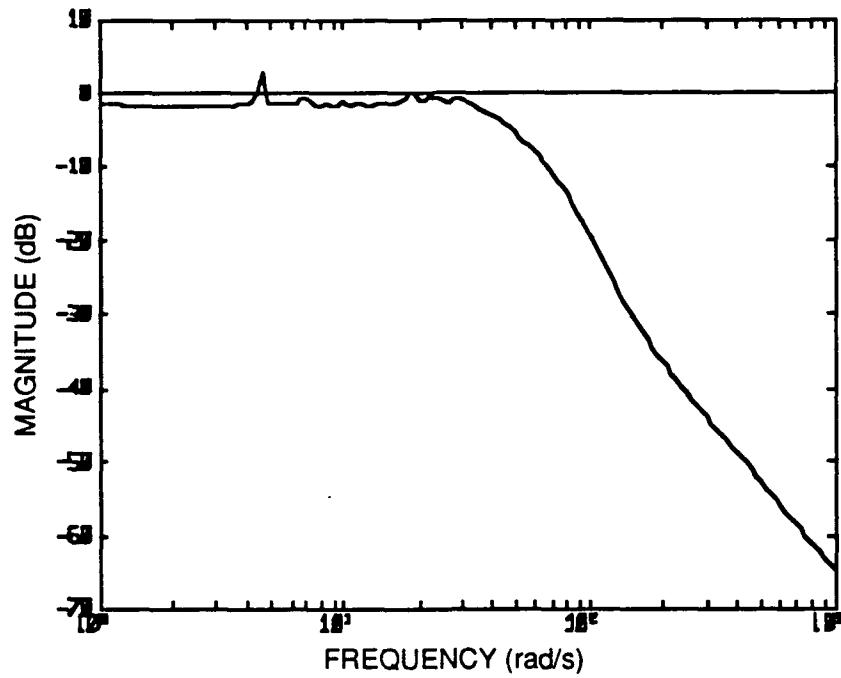
Figure 8.4 Closed-Loop Transfer from All Disturbances to All Errors (T$_{22}$)
(72-State Compensator).
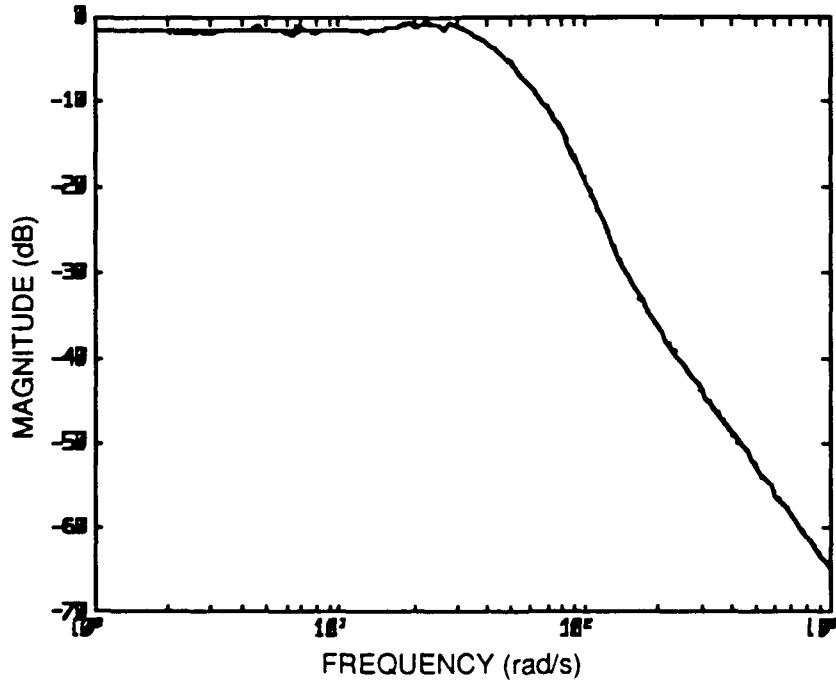
Figure 8.5 Closed-Loop Transfer from All Disturbances to All Errors (T$_{22}$)
(73 and 80-State Compensators).

143

As a final precaution to ensure that nothing catastrophic results from using the 73-state compensator model, Figures 8.6 and 8.7 respectively show the maximum singular value frequency responses of the 73 and 80-state compensators, and of the transfer about the delta block for the 73-state controller closed-loop system. From the figures, it can be seen that the two compensators have virtually identical maximum singular value frequency responses, and that robustness is preserved by using the 73-state compensator realization. Also, since the full and reduced-order compensators have nearly identical maximum singular values, it may be deduced that the bandwidth of the reduced-order system is the same as the 80 rad/s bandwidth of the full-order system.
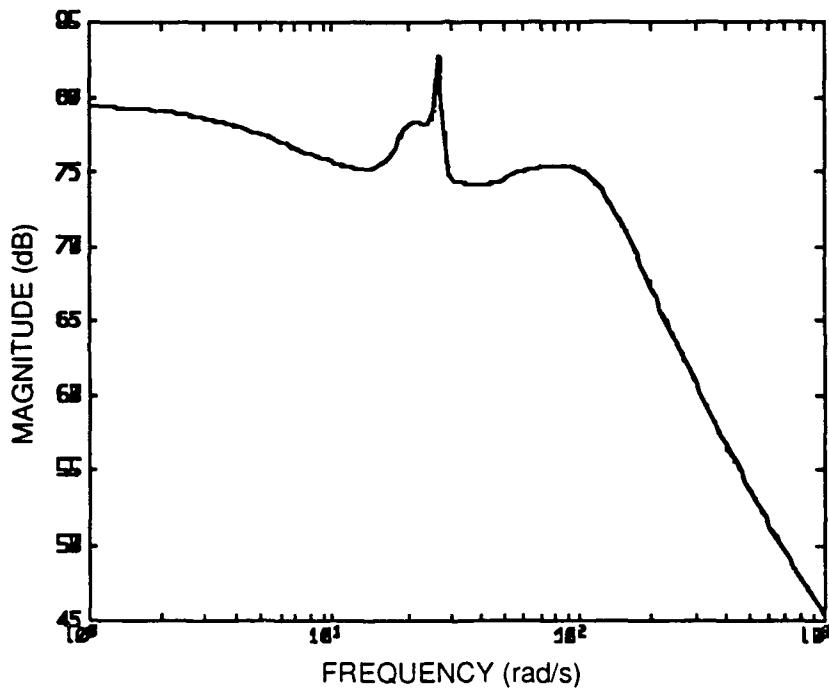
Figure 8.6 73 and 80-State H∞ Loop-Shaped Control Compensator
Max Singular Value Frequency Responses.
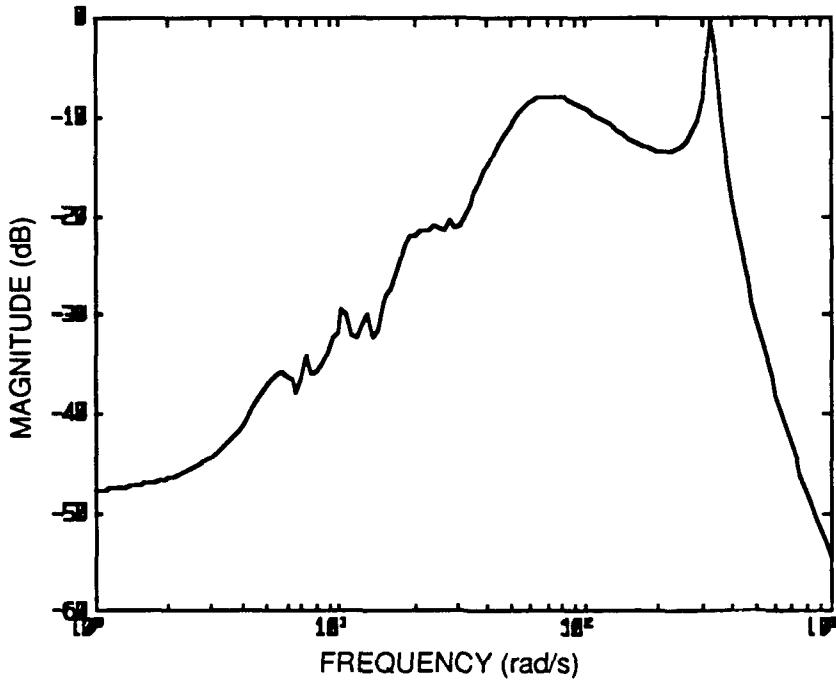
Figure 8.7 Closed-Loop Transfer about Δ_M (T_{11})
(73-State H_{∞} Loop-Shaped Control Compensator).

In this section, it has been demonstrated that use of the B&T model reduction technique allows elimination of 7 unnecessary states from the compensator model, yielding a significant (~10%) decrease in system complexity and required computation time. It has also been shown that reduction of the compensator model order to 73 states does not significantly detract from closed-loop performance and stability robustness, and in general does not alter any of the significant frequency response dependent characteristics of the resulting system. Consequently, the 73-state compensator is used in the validation of the control system design via simulation which follows.

8.4 Design Simulation

8.4.1 Introduction

In this section, the reduced-order H_{∞} loop-shaped control compensator design obtained in Section 8.3 is validated via time-domain simulation and steady-state covariance analysis for both open and closed-loop BEA models. In Section 8.4.2, the system is assumed to be

145

driven by filtered white noise disturbance inputs, and time domain simulation allows the relative magnitudes and spectral contents of the open and closed-loop errors to be compared, while steady- :ate covariance analysis techniques demonstrate the satisfaction of the infinity-norm bound on stochastic input-output RMS values asserted in Section 3.4.2. In Section 8.4.3, the disturbances are assumed to be sinusoidal, and representative time responses which illustrate the significant differences between open and closed-loop behavior under deterministic conditions are presented. As once again presentation of results for all system variables would result in a prohibitively large number of plots, an effort has been made to present only selective time responses which demonstrate characteristic or otherwise noteworthy behavior.

8.4.2 Stochastic Time-Domain Simulation

In this thesis, the fundamental premise upon which control system design is based is the induced-norm property of the operator infinity-norm to RMS (2-norm) bounded inputs and outputs. Based on this property and the scalings derived in Chapter 6, a 73-state compensator has been obtained which is supposed to guarantee that the RMS values (2-norms) of the segment phasing and LOS errors remain less than 0.15 micrometers and 0.1 microradians, respectively, for all torque disturbance inputs of RMS (2-norm) less than 0.353 N-m, and measurement noises of RMS (2-norm) less than 1.414×10^{-2} micrometers/microradians. In this subsection, the infinity-norm bound on input-output relationships is shown to be satisfied for the stochastic scenario in both the open and closed-loop settings. This is accomplished via steady-state covariance analysis techniques. Additionally, time responses are presented which illustrate characteristic system behavior under the influence of filtered white noise disturbances. Open and closed-loop results are presented simultaneously in order to facilitate comparison between the two.

As mentioned in the beginning of this thesis, the time-domain nature and spectral properties of the torque disturbances and measurement noise present in the BEA system are not precisely known. Therefore, the assumption is made that the disturbances can be represented as random processes with typically broadband spectral characteristics. One convenient way of modeling such processes is to represent them as outputs of linear-time-invariant low-pass systems driven by white noise. Such band-limited random signals are often called filtered white noise or "colored-noise" processes, because their spectral content is no longer equal at all frequencies, as is the case for white noise processes. As long as the bandwidth of the coloring filter is selected to be greater than the bandwidth of the

146

system being driven, colored-noise inputs may be used to excite all system natural frequencies. Modeling the system disturbances as filtered white noise processes therefore allows the dominant frequency dependent behavior of the system to be elicited.

Consider (8.3), which shows the transfer function of a typical SISO low-pass coloring filter. Here, k is the dc gain and ω_b is the coloring filter break frequency.

$$w(s) = \frac{k\,\omega_b}{s + \omega_b} \tag{8.3}$$

Letting the individual elements of the disturbance vector be represented by

$$d_i(s) = w(s)\,\xi \tag{8.4}$$

where ξ is unit-intensity white noise, makes d_i a filtered white noise process as desired, and the following relations are known to hold [22]. The power-spectral-density (PSD) of d_i, $\phi_d(s)$, is given by

$$\phi_d(s) = w(-s)w(s)\,\phi_\xi(s) = w(-s)w(s) = \frac{k^2\,\omega_b^2}{-s^2 + \omega_b^2} \tag{8.5}$$

and the variance of d_i, σ_d^2, is given by the integral of ϕ_d

$$\sigma_d^2 = \frac{1}{2\pi}\int_{-\infty}^{\infty} \phi_d(\omega)\,d\omega = \frac{k^2\,\omega_b}{2} \tag{8.6}$$

Since the RMS value of d_i, σ_d, is equal to the square-root of the variance of d_i, σ_d^2, (8.3-8.6) allow construction of stochastic disturbance inputs of bounded and known RMS values, via prudent selection of the coloring filter break-frequency and dc gain. Note that for a given disturbance variance, (8.6) indicates that k^2 and ω_b are inversely proportional. Therefore, higher bandwidth coloring filters will have smaller dc gains. Since any disturbance spectral content beyond the closed-loop system bandwidth is automatically attenuated, the approximate worst-case disturbance for a given disturbance variance is constructed by selecting ω_b to be just beyond the system bandwidth, thereby creating the "highest gain" disturbance which still excites all the system natural frequencies. Selecting

147

ω_b to equal 90 rad/s to exceed the closed-loop bandwidth of 80 rad/s observed in Chapter 7, and employing the single element RMS bounds corresponding to the vector RMS bounds noted at the beginning of this section (0.25 N-m and 7×10^{-3} micrometers/microradians), (8.6) yields respective values of 0.0373 and 7.454x10^{-10} for disturbance torque and measurement noise coloring filter dc gains.

Now, in order for steady-state covariance analysis techniques to be applied, the dynamics of the coloring filters must be augmented to the system dynamics representing the transfer from d to e, so that the system is in effect driven by white noise inputs only. If a state-space realization for the individual coloring filters is obtained

$$w(s) = \left[\begin{array}{c|c} a_w & b_w \\ \hline c_w & d_w \end{array} \right] = \left[\begin{array}{c|c} -\omega_b & \sqrt{k\omega_b} \\ \hline \sqrt{k\omega_b} & 0 \end{array} \right]$$

(8.7)

then the MIMO weighting function, W(s), resulting from applying (8.7) to all the system disturbances can be formed simply as

$$W(s) = \left[\begin{array}{c|c} A_w & B_w \\ \hline C_w & D_w \end{array} \right] = \left[\begin{array}{c|c} a_w I_d & b_w I_d \\ \hline c_w I_d & d_w I_d \end{array} \right]$$

(8.8)

where it is understood that the torque disturbances and measurement noise filters incorporate the different k values specified above, and I_d is the square identity matrix with dimnsion equal to the number of disturbances (=10). Consequently, if the state-space realization for the open or closed-loop transfer from d to e is given by

$$G_{11}(s), \; T_{22}(s) = \left[\begin{array}{c|c} A & B \\ \hline C & 0 \end{array} \right]$$

then the dynamics of the augmented system, $T_a(s)$, representing the transfer from white noise inputs to the performance vector e (either open or closed-loop as appropriate) can be represented as

$$T_a(s) = \left[\begin{array}{c|c} A_a & B_a \\ \hline C_a & D_a \end{array} \right]$$

(8.9)

where

148

$$A_a = \begin{bmatrix} A & BC_w \\ 0 & A_w \end{bmatrix}$$

$$B_a = \begin{bmatrix} 0 \\ B_w \end{bmatrix}$$

$$C_a = [C \quad 0]$$

$$D_a = 0$$

It is a well-known fact [9] that an LTI system driven by white noise inputs has a steady-state state covariance matrix, Σ_x, which is obtainable as the unique, positive-definite solution of the standard Lyapunov equation

$$A_a\Sigma_x + \Sigma_xA_a^T + B_aB_a^T = 0 \tag{8.10}$$

and a steady-state error covariance matrix, Σ_e, which is given by the relation

$$\Sigma_e = C_a\Sigma_xC_a^T \tag{8.11}$$

The RMS values of the segment phasing and LOS errors are easily obtained from (8.11) by picking off the diagonal elements of Σ_e corresponding to the individual error variances, adding, and taking the square-root of the resultant sum. With the disturbances selected as specified above, the framework described by (8.3-8.11) thus allows convenient time-domain simulation and direct verification of the design's ability to meet the performance objectives specified for the BEA segment phasing/jitter control system. The necessary groundwork for validation of the compensator design has now been laid. Results of application of the above procedure are now presented.

Table 8.1 below shows the variances for the 14 segment phasing and 2 LOS errors, as determined from solution of (8.10) and (8.11), and the RMS values of the total segment phasing and LOS errors, calculated as explained above, for the H_∞ loop-shaped control design. Most obvious from the numerical values in the table is that the open-loop variances are, as expected, significantly greater in magnitude than the closed-loop error variances, demonstrating the improvement in system performance achieved via feedback. Additionally, the variances of the segment phasing errors are in general significantly larger

149

than the LOS error variances. This too, is expected, as the transfer to the segment phasing errors was seen to drive attainable performance of the closed-loop weighted-control H_∞ design in Section 7.4.3. Also interesting to note from the table is that for the open-loop case, the variances of the segment phasing errors at the mirror corners (errors 1, 3, 5, 7, 9, 12, and 14) are in general 2 to 3 times as big as the variances of the errors in the middle of segment edges, while such a pattern does not hold for the closed-loop case. The most important information contained in the table appears in the last two rows, however, which detail the open and closed-loop RMS values of the total segment phasing and LOS performance vectors. As can be seen from the entries, the open-loop RMS error values exceed the 0.15 micrometer segment phasing and 0.10 microradian LOS performance specifications, while the closed-loop error variances are well within the specified performance tolerances. Since the scaled problem was set up so that a d to e transfer infinity-norm of 1 guaranteed achieving these performance specifications, and the closed-loop design selected had infinity-norm of 0.9413, the satisfaction of the infinity-norm bound on input-output RMS values is thus demonstrated for the closed-loop case (0.0736 < 0.9413 x 0.15 = 0.141, and 0.01056 < 0.9413 x 0.10 = 0.0941). Also, the magnitude of the improvement between closed and open-loop performance can be seen more clearly when one considers that the open-loop segment phasing and LOS error RMS values are respectively more than 65 and 20 times greater than their closed-loop counterparts. Recalling that the infinity-norm of the open-loop transfer is 59 dB (891), it is obvious that since the open-loop RMS error values at most exceed 33 times performance specifications, that the infinity-norm RMS input/output bound relationship is satisfied for the open-loop case as well (33 < 891).

	Open-Loop	Closed-Loop
σ_{sp1}^2 (microm)^2	2.7346	3.1159e-04
σ_{sp2}^2 (microm)^2	1.3023	8.1882e-04
σ_{sp3}^2 (microm)^2	2.7201	2.6163e-04
σ_{sp4}^2 (microm)^2	1.3150	6.7535e-04
σ_{sp5}^2 (microm)^2	1.6023	1.9846e-04
σ_{sp6}^2 (microm)^2	0.9678	8.5171e-04
σ_{sp7}^2 (microm)^2	2.7346	3.1159e-04
σ_{sp8}^2 (microm)^2	1.0804	2.9822e-04
σ_{sp9}^2 (microm)^2	2.7201	2.6163e-04
σ_{sp10}^2 (microm)^2	0.8311	2.3967e-04
σ_{sp11}^2 (microm)^2	0.8321	9.6641e-05
σ_{sp12}^2 (microm)^2	2.2888	3.3599e-04
σ_{sp13}^2 (microm)^2	0.8896	3.2232e-04
σ_{sp14}^2 (microm)^2	2.2856	4.3688e-04
σ_{losx}^2 (microrad)^2	0.0332	8.3876e-05
σ_{losy}^2 (microrad)^2	0.0177	2.7552e-05
σ_{sp} (microm)	4.9299	**0.07362**
σ_{los} (microrad)	0.2257	**0.01056**

Table 8.1 Steady-State Covariance Analysis Results
(Reduced-order H_∞ Loop-shaped Control Design).

Figures 8.8 and 8.9 show representative time responses of the two BEA filtered white noise torque disturbances, generated as described in the preceding paragraphs, and sampled at intervals of 0.01 seconds. The random nature of the torque disturbances is obvious from the plots, as any two consecutive values seem to be highly uncorrelated. The RMS values of the torque disturbances also seem to be accurately represented, as it appears that 95 percent of the values lie within the 3σ margins (± 0.75 N-m).
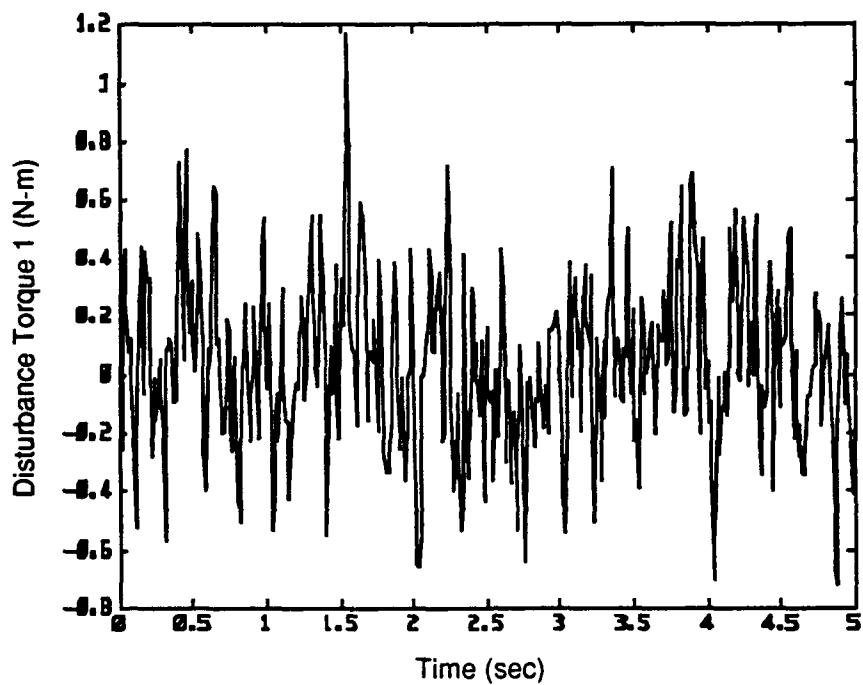
Figure 8.8 Stochastic Torque Disturbance 1 Time Response.
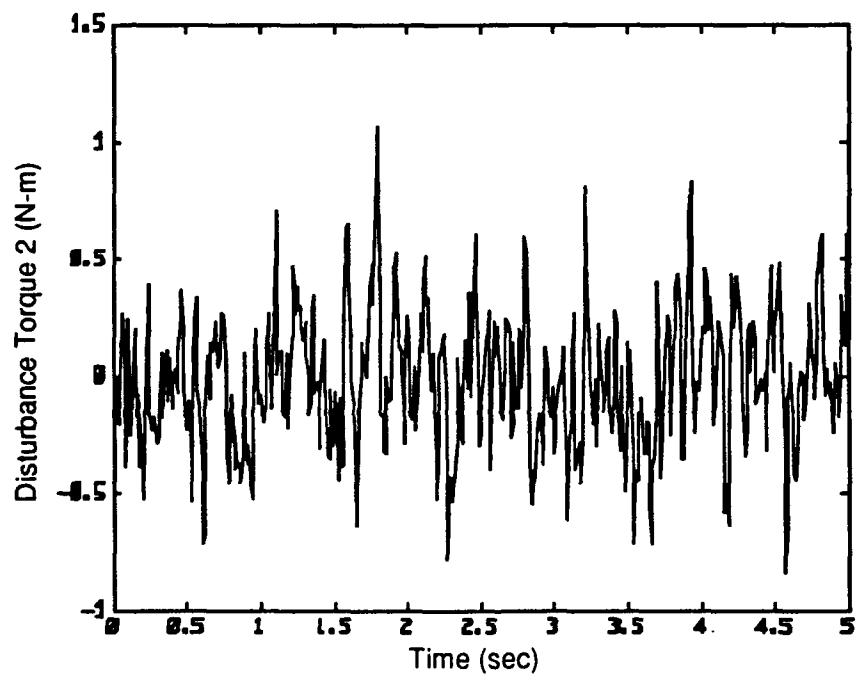
Figure 8.9 Stochastic Torque Disturbance 2 Time Response.

152

Time responses are not presented for the 8-element measurement noise vector, for two main reasons. First, measurement noise has no effect on the error vector in the open-loop setting, so that open-loop performance is characterized in terms of attenuation of the torque disturbances only. Therefore, closed-loop system performance can only fairly be compared to open-loop system performance in terms of the torque disturbance rejection properties of the two systems. Second, as was seen from the transfer functions of the various closed-loop subblocks in Section 7.4.3, it was the transfer from the torque disturbances to the segment phasing errors that drives performance of the closed-loop weighted-control H_∞ design, not the transfer from the measurement noise. Thus, the measurement noise is of secondary importance to performance of the closed-loop system. Simulation both with and without measurement noise validated these conclusions, and the final simulation results are therefore presented with torque disturbances only, although measurement noise was included for purposes of the steady-state covariance analysis performed above.

Figures 8.10 and 8.11 respectively show the open and closed-loop segment phasing errors at position 14 (reference Figure 2.5) as a function of time, again sampled at intervals of 0.01 seconds. Position 14 is at the midpoint of the edge connecting primary mirror petal 1 to the center primary mirror segment, and exhibits a time response characteristic of the other segment phasing errors. From the figures, it can be seen that, on the average, the open-loop response is significantly larger than the closed-loop response, as expected. In fact, the largest amplitude of the open-loop error is more than twenty times the magnitude of the largest amplitude closed-loop error value. The closed-loop system can again therefore be seen to exhibit a significant improvement over the open-loop system performance. The open-loop error also appears in general to be less jagged than its closed-loop counterpart, or in general more slowly time varying. This can be interpreted as meaning that the open-loop error is domir 'd by low-frequency components, while the closed-loop error is dominated by higher-frequency components. Since the compensator employed in the closed-loop system was designed specifically to reject low-frequency disturbances, this interpretation makes sense. Also note that both these error time responses are significantly less jagged than the torque disturbances. This effect can be attributed to the high-frequency attenuation resulting from passing the colored-noise through a lower-bandwidth system.
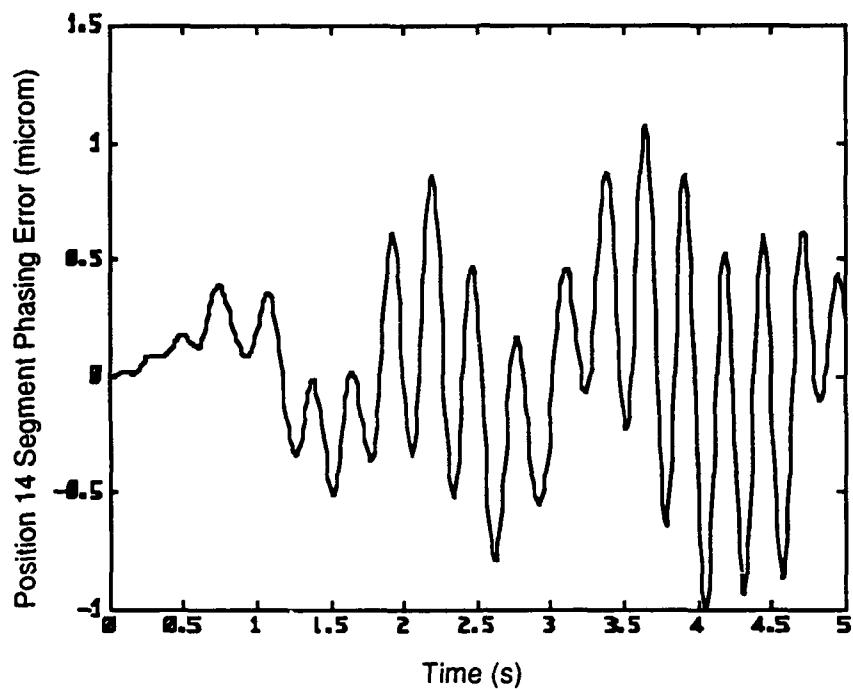
Figure 8.10 Open-Loop Position 14 Segment Phasing Error Time Response.
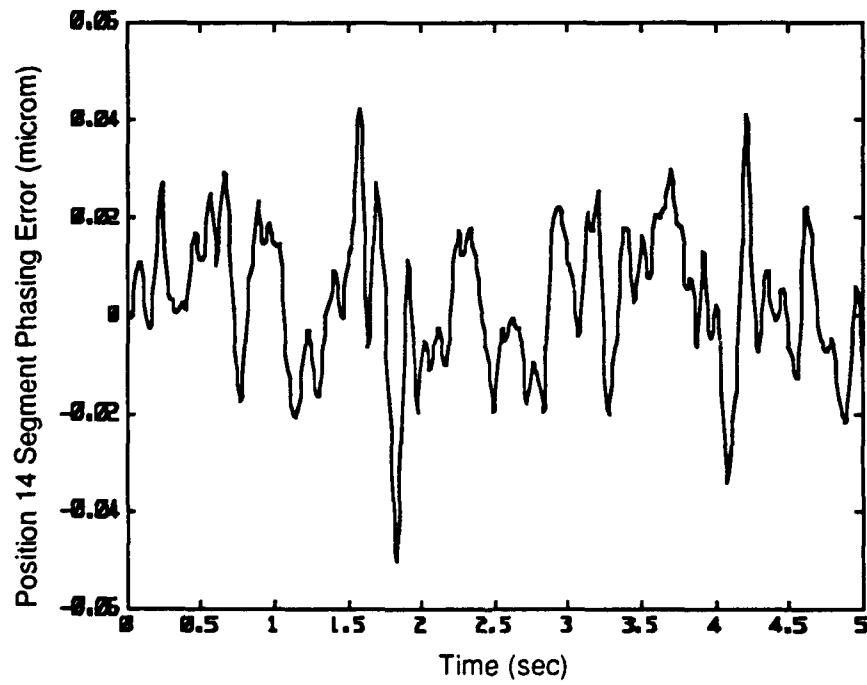
Figure 8.11 Closed-Loop Position 14 Segment Phasing Error Time Response.

154

Figures 8.12 and 8.13 respectively show the time responses of the open and closed-loop LOS errors about the X axis to the disturbances of Figures 8.8 and 8.9. Again, note that the open-loop response reaches significantly larger magnitudes (about 10 times greater) than the closed-loop response, and also displays a more predominantly low-frequency nature than does the closed-loop response.
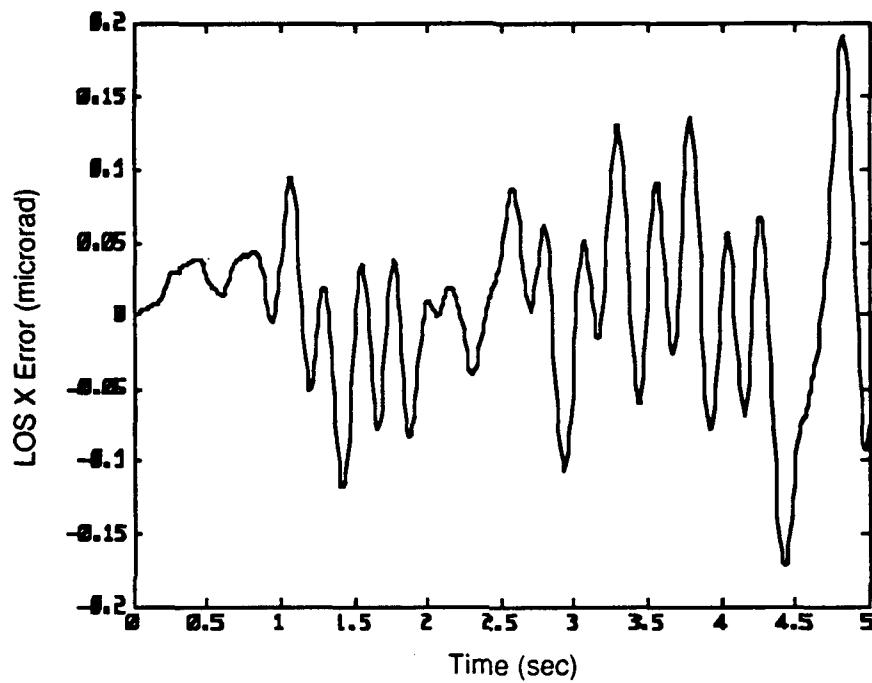
Figure 8.12 Open-Loop LOS X Error Time Response.
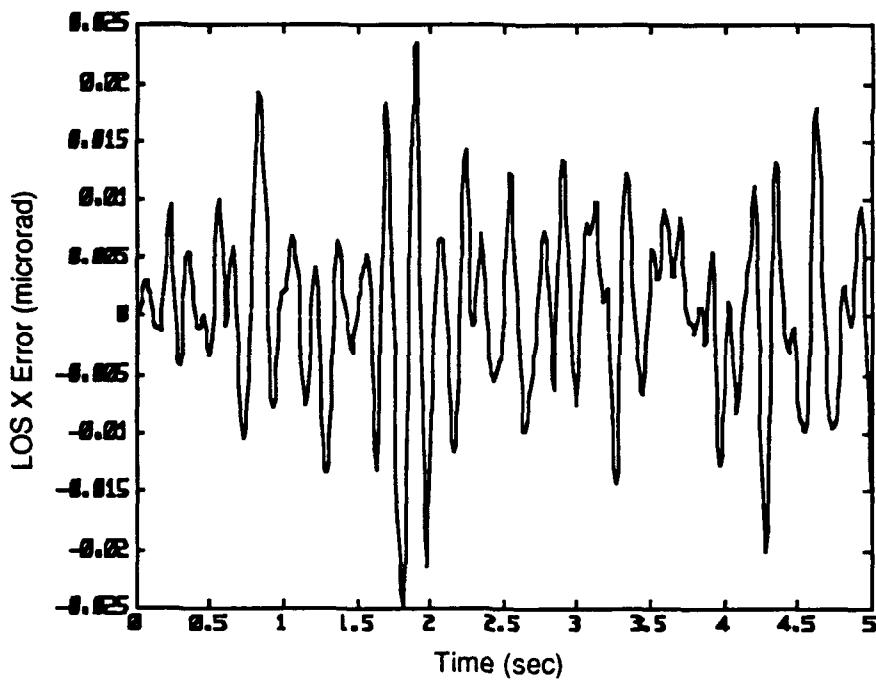
Figure 8.13 Closed-Loop LOS X Error Time Response.

As a final item of interest, Figures 8.14 and 8.15 show the time responses of two of the system controls generated in the closed-loop simulation. Figure 8.14 shows the time response of an in-plane (radial) actuator located on primary mirror segment 1, and Figure 8.15 shows the time response of the colocated out-of-plane (longitudinal) actuator. Two items of significance may be observed from the figures. First, the system controls display a random and predominantly high-frequency nature consistent with the high-frequency nature observed in the closed-loop performance variable time responses. Second, note that similar and very small radial and longitudinal actuator levels (fractions of a millinewton) are called for in rejecting these disturbances. Actuator saturation therefore does not appear to be a concern for operation in the disturbance environment created, although the very high actuation rates called for could provide some problems.
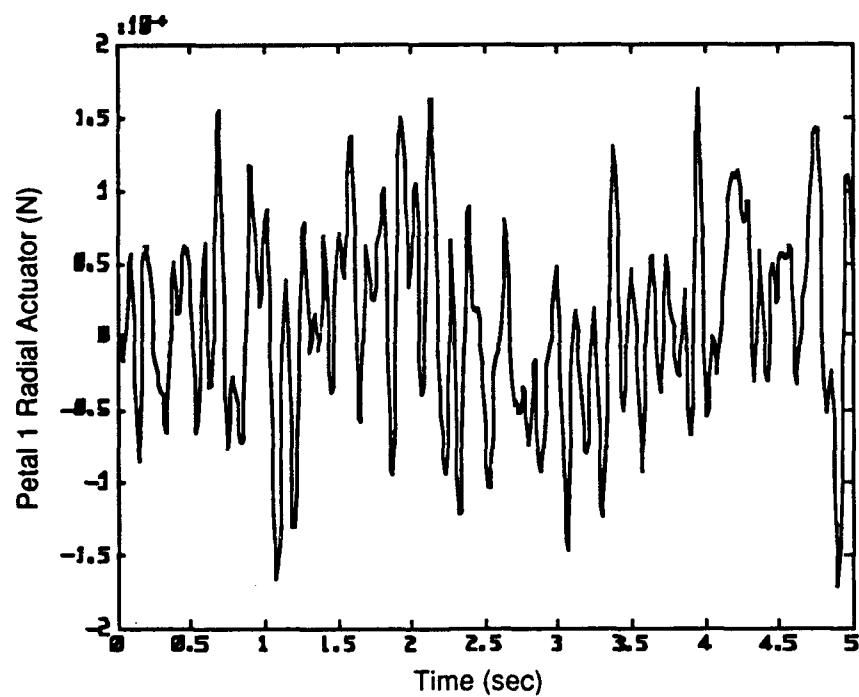
Figure 8.14 Petal 1 Radial Actuator Time Response.
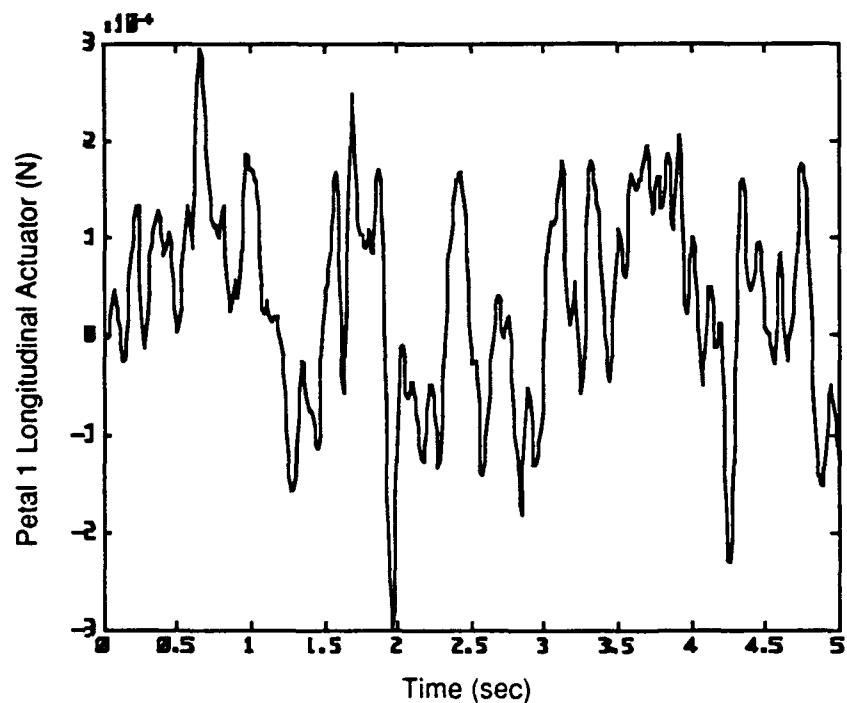
Figure 8.15 Petal 1 Longitudinal Actuator Time Response.

157

In this section, the reduced-order weighted-control H_∞ design obtained in Section 7.4.3 was validated for stochastic torque disturbance inputs via time domain simulation and steady-state covariance analysis. Via covariance analysis, the design was shown to meet performance specifications for filtered white noise inputs of prescribed RMS values, thereby demonstrating satisfaction of the infinity-norm bound relationship on input/output RMS values in a closed-loop setting. Satisfaction of this bounding relationship was also shown for the open-loop system, and it was verified that open-loop performance does not meet performance objectives. Time domain simulation further illustrated the superiority of the closed-loop system over the open-loop system, and demonstrated the low-frequency disturbance attenuation properties of the closed-loop system. While the results presented in this section concerning the response of the open and closed-loop systems to stochastic disturbances has revealed much about the nature of the compensator selected and the resulting closed-loop system, they still do not reveal as complete a picture as might be obtained. Toward this end, the response of the open and closed-loop systems to re resentative deterministic disturbance inputs will now be addressed.

8.4.2 Deterministic Sinusoidal Simulation

In this section, system response to sinusoidal torque disturbances is briefly addressed. The main purpose of this is to further demonstrate the differences between the open and closed-loop system time behaviors, and to illustrate certain details of the compensator design not yet revealed. As the infinity-norm bound on input/output behavior has already been shown to be satisfied in the stochastic setting, that topic is not addressed herein.

Figures 8.16 and 8.17 respectively show the open-loop maximum amplitude segment phasing and LOS Y errors versus time for a disturbance torque vector of the form

$$
d_T(t) \;=\;
\begin{bmatrix}
0.11\sin\left(0.628t\right) \\[2mm]
0.11\sin\left(0.628t - \dfrac{\pi}{2}\right)
\end{bmatrix}
\text{N-m}
$$

(8.12)

acting for a duration of 10 seconds. Note that each element of the sinusoidal disturbance has 0.11 N-m maximum amplitude, frequency of 0.628 rad/s, and period equal to 10 seconds, so that the simulated disturbance has been constructed so as to act over one period. From the equations presented in Section 6.4, it can be verified that the 2-norm of (8.12) acting over its period is 0.35 N-m, so that (8.12) is consistent with the upper bound

on allowable disturbance 2-norms established in Section 6.4. It can also be seen from (8.12) that the two torque disturbances are 90 degrees out of phase with each other. Selecting the disturbance torque vector as in (8.12) provides a relatively general scenario for comparing deterministic open and closed-loop system time responses, consistent with the disturbance assumptions made up to this point.

Examination of Figures 8.16 and 8.17 reveals several interesting characteristics of the open-loop system. The most obvious feature of the two plots is the very lightly damped nature of the open-loop model, as evidenced by the tremendously long oscillatory time responses. The effects of the sinusoidal disturbance torques are clearly evident in the first 10 seconds of the plots, but even 70 seconds after the disturbance has ceased to act, the induced transient oscillations are still nowhere near having settled out. Fairly large open-loop error magnitudes may also be observed from the figures. The unsatisfactory nature of the open-loop system disturbance rejection performance is thus apparent.
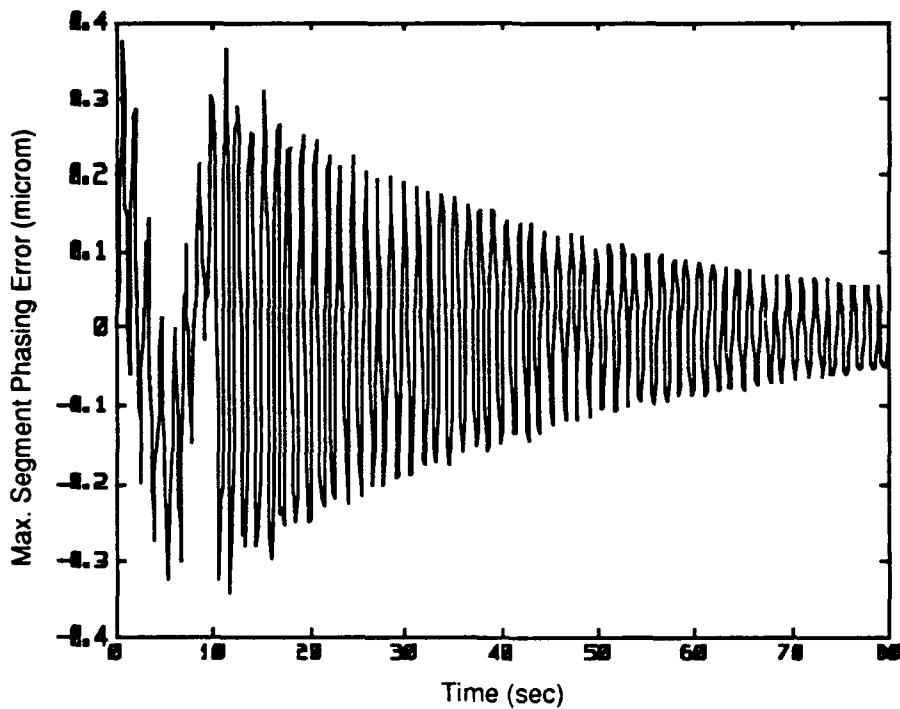
Figure 8.16 Open-Loop Max. Segment Phasing Error Time Response.

159
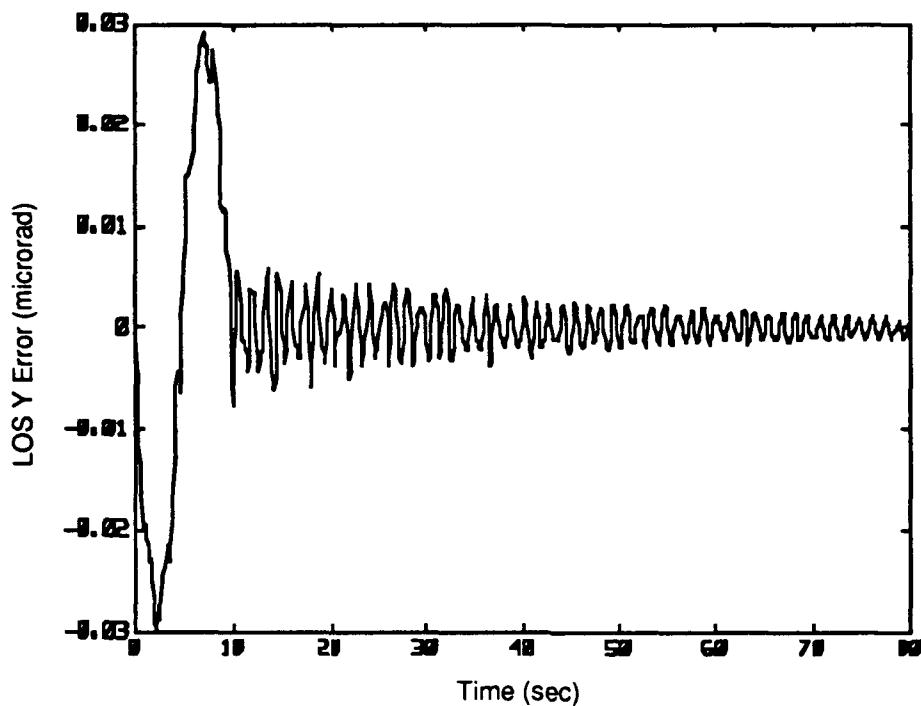
Figure 8.17 Open-Loop LOS Y Error Time Response.

Figures 8.18 and 8.19 show the respective closed-loop time responses of all the segment phasing and LOS errors to the input disturbance vector of (8.12). By comparing these figures to Figures 8.16 and 8.17, it can be seen that the maximum amplitudes of the largest closed-loop segment phasing and LOS errors are respectively more than 20 and 12 times smaller than their open-loop counterparts. The most striking aspect of the closed-loop responses, however, is the lack of slowly decaying transients observed in the open-loop setting. Note that for the closed-loop case, 10 second period sinusoidal disturbances translate into attenuated 10 second period sinusoidal outputs, indicating that the steady-state is achieved very rapidly in the closed-loop design. Once the disturbance stops acting at the 10 second mark, there is virtually no evidence of undesirable overshoot or significant transient oscillation occuring as was the case for the open-loop response. From the figures it may therefore be deduced that one previously overlooked aspect of the weighted-control H_∞ loop-shaped compensator is that it creates significant damping in the closed-loop system, which can be seen to be desirable from the deterministic closed-loop time responses of Figures 8.18 and 8.19.

160
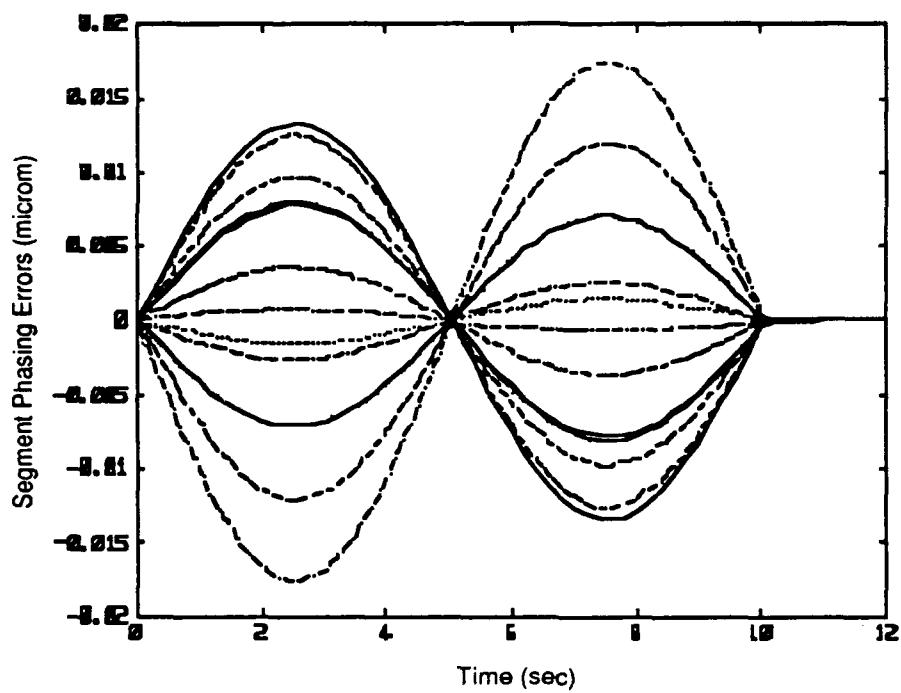
Figure 8.18 Closed-Loop Segment Phasing Error Time Responses.
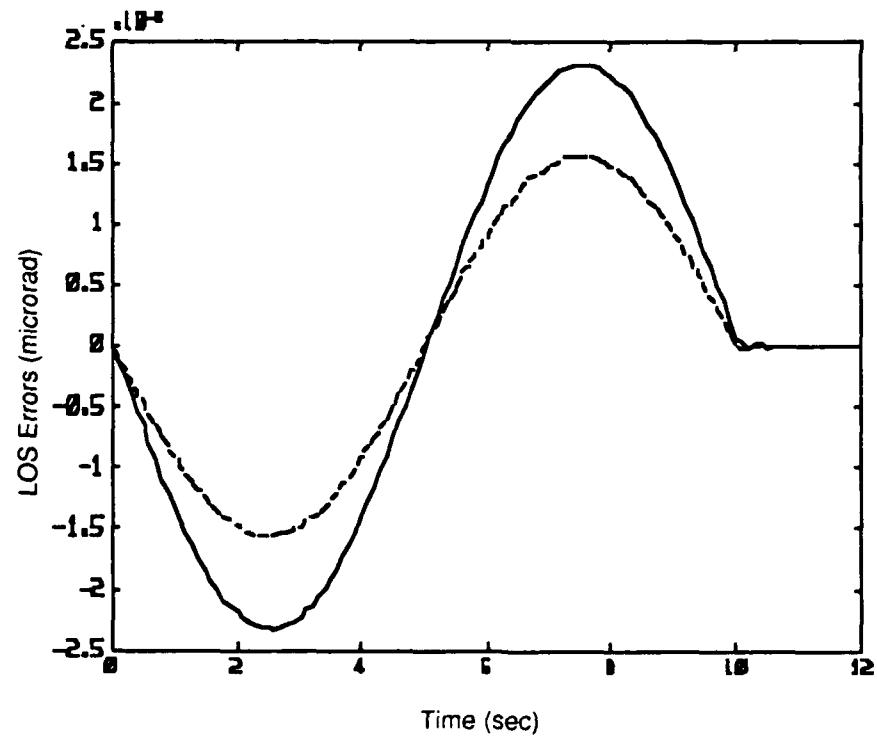
Figure 8.19 Closed-Loop LOS Error Time Responses.

161

In order to verify this deduction, consider Figure 8.20, which is a complex plane pole-plot for the weighted-control H_∞ loop-shaped compensator closed-loop system. As can be seen from the figure, several system poles still reside along the jω-axis, but now, in addition, there are several highly damped poles on the real axis, as well as a significant number at an angle of approximately 30 degrees from the jω-axis. These poles have a damping factor of approximately 0.56, which represents an over two order of magnitude increase beyond the open-loop 0.005 uniform damping factor. Thus, in addition to guaranteeing a bound on the 2-norms of the segment phasing and LOS performance variables, the weighted-control H_∞ loop-shaped compensator markedly improves the closed-loop deterministic time behavior via increased damping.
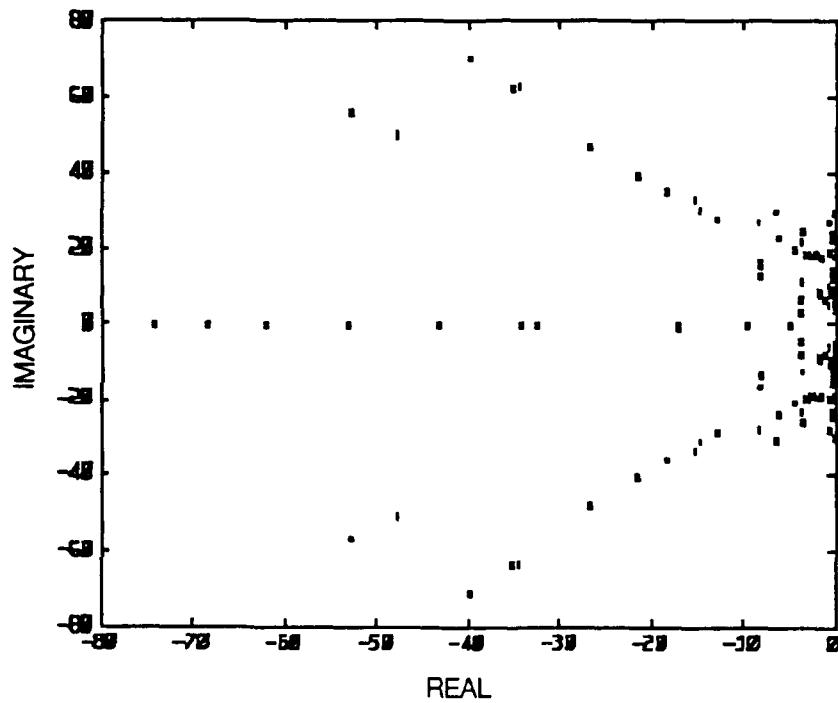
Figure 8.20 Closed-Loop Pole-Plot.

In this section, the reduced-order weighted-control H_∞ loop-shaped compensator has been validated under both stochastic and deterministic disturbance assumptions, using time domain simulation and steady-state covariance analysis. The significant benefit of feedback was demonstrated by the superiority of closed-loop system performance over open-loop performance, in both the stochastic and deterministic settings. Additionally, it was shown

162

that the weighted-control H_∞ loop-shaped compensator markedly cha. ges the complex plane locations of the effective system poles, thereby increasing system damping. It is a well-known characteristic of optimal feedback controllers that this shift in pole locations is accomplished via selective "cancellation" of non-desirable open-loop zeros with compensator poles, and subsequent replacement with desirable compensator zeros, so that the closed-loop poles migrate to the selected compensator poles under feedback. This process is called "approximate plant inversion" by some [3]. An obvious danger to such a methodology is inexact knowledge of the open-loop plant pole/zero locations. Attempts to "invert" a system's dynamics based on an inaccurate model can sometimes lead to catastrophic degradations in system stability and performance. Therefore, in order to be as complete as possible, the effects of parametric uncertainty on open-loop system natural frequencies are now addressed

8.5 Performance Robustness and Effects of Open-Loop Natural Frequency Parametric Uncertainty

As discussed in the preceding paragraph, optimal controllers alter the behavior of the open-loop plant via the mechanism of "approximate plant inversion", in which undesirable system poles and zeros are respectively cancelled with compensator zeros and poles, and the best system response achievable is then obtained via selection of any additional compensator pole/zero locations. One obvious flaw in such a design methodology is that uncertainty invariably exists in the location of the open-loop poles, due to approximations and errors in the modeling process. If the true system poles are not exactly the same as those of the design model, then the multivariable pole-zero cancellations employed by plant-inverting techniques are not likely to be completely successful, and may even lead to serious degradations in nominal system stability and performance. It is therefore of interest to the designer to somehow assess the potential impact of open-loop pole location errors prior to compensator implementation. Therefore, in this section it is demonstrated how the Small Gain Theorem may be used to assess the stability robustness of the weighted-control H_∞ loop-shaped compensator closed-loop system to five percent parametric uncertainty in the open-loop finite-element model stiffness matrix elements, corresponding to two and one-half percent parametric uncertainty in the open-loop natural frequencies. Since the Small Gain Theorem is known to be conservative, the actual effects of open-loop pole location errors on closed-loop stability for two specific perturbed natural frequency models

is then directly verified via computation of the closed-loop poles. Finally, robustness of performance of non-perturbed and perturbed models is assessed via computation of the closed-loop d to e transfer function frequency response.

As discussed in Sections 5.1 and 6.5, the Small Gain Theorem may be used to conservatively assess the stability robustness of any system containing uncertainty, as long as that uncertainty may be gain-bounded as a function of frequency. In particular, in this thesis a framework has been developed for testing the stability robustness of systems where the only uncertainty in the plant is modeled as a multiplicative error at the plant output (reference Sections 5.1 and 6.5 for details). As was previously developed, stability robustness of such an uncertain system may be guaranteed by ensuring that the infinity-norm of the closed-loop transfer about the uncertainty block, $\|T_{11}(s)\|_\infty$, is less than one, as long as the infinity-norm of the uncertainty block is unity bounded. Consider Figure 8.21, which shows the maximum singular value frequency responses of multiplicative errors, $\Delta_M(s)$, at the plant output for two perturbed natural frequency systems, and of a 4th-order transfer function which effectively bounds both the errors. As mentioned above and in Section 6.5, the multiplicative errors were obtained from the relation

$$\Delta_M(s) = (G_a(s) - G(s)) G(s)^{-1} \tag{8.13}$$

where $G_a(s)$ represents the complex valued transfer function matrix of a 108-state model with plus or minus two and one-half percent error in the open-loop natural frequencies evaluated at a given frequency, and $G(s)$ represents the complex valued transfer function matrix of the 56-state design plant model evaluated at the same frequency. As was also previously mentioned, the basis for selecting such perturbed systems is a reasonable assumption that the actual BEA system stiffness matrix elements are uniformly either five percent greater or smaller than those of the modeled system. As can be seen from Figure 8.21, the nominal design model possesses large errors at high-frequency due to model-reduction truncation of the high-frequency modes (as was previously the case for the unperturbed system), but now there is also significant error at low frequency due to the difference between modeled and "actual" open-loop natural frequencies. It can also be seen from Figure 8.21 that although there are differences between the two multiplicative error curves, they are not large, and one transfer function may therefore be used to effectively bound the multiplicative error curve for all systems with natural frequency errors of up to plus or minus two and one-half percent.

164
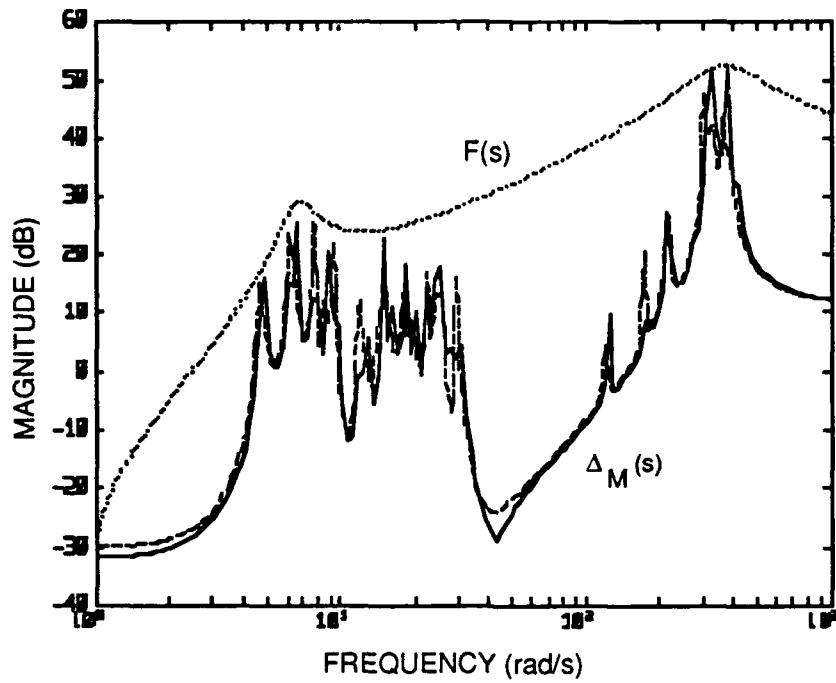
Figure 8.21 Perturbed System Plant Output Multiplicative Errors and
Bounding Transfer Function Frequency Responses. ·

Now consider Figure 8.22, which shows the closed-loop transfer maximum singular values about the delta block for the perturbed plants output multiplicative error bound of Figure 8.21. As can clearly be seen from the figure, the maximum singular values of the closed-loop transfer about the uncertainty block exceed unity (0 dB) over almost all of the frequency range of interest. Figure 8.22 therefore unequivocally indicates that the closed-loop system is not guaranteed to be robustly stable to two and one-half percent error in open-loop natural frequencies, according to the sufficient test of the Small Gain Theorem.

165

MAGNITUDE (dB)

4
3
2
1
0
-1
-2
-3
-4

10¹   10²
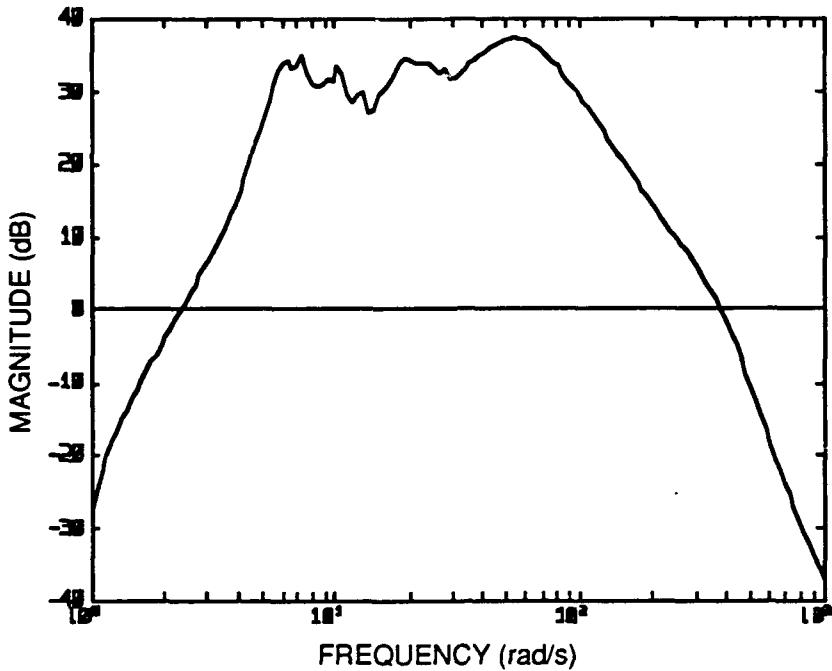
FREQUENCY (rad/s)

Figure 8.22 Closed-Loop Transfer about Δ_M (T_{11})
(Perturbed Open-Loop Natural Frequency Systems).

The Small Gain Theorem is based purely on gain considerations, however, and is known to be conservative. Therefore, the actual closed-loop systems using the two 108-state perturbed natural frequency models and the 73-state reduced-order weighted-control H_∞ loop-shaped compensator may be formed, and the closed-loop poles and d to e transfer function maximum singular value frequency responses may be computed to verify the actual effects of the parametric uncertainty. In doing this for the two perturbed open-loop models chosen, the resulting closed-loop systems are found to be stable, in spite of the indications of the stability robustness test of the Small Gain Theorem. The conservatism of the SGT is thus made apparent. Severe degradations in closed-loop performance do however result, as can be seen from Figures 8.23 and 8.24 below. Figure 8.23 shows the maximum singular value closed-loop d to e transfer for the system with five percent greater stiffness than the design model, while Figure 8.24 shows the maximum singular va'ue closed-loop d to e transfer for the system with five percent smaller stiffness. Although one might expect a stiffer system to better reject disturbances, Figure 8.23 indicates that this is not the case, and illustrates the importance of feeding the precise location of the open-loop poles and zeros to the optimal control problem. Figure 8.24 bears further testimony to this importance, as the indicated performance of the less stiff system is even worse than that of

166

the stiffer system. The difference in performance evident in the figures suggests that if uncertainty does exist in open-loop pole and zero locations, it is better to have a stiffer system, as intuition would also lead one to believe. Note that even in the presence of open-loop natural frequency parametric uncertainty, closed-loop performance specifications are met at low frequency, and the degraded higher frequency performance is, in general, still superior to that of the open-loop system.
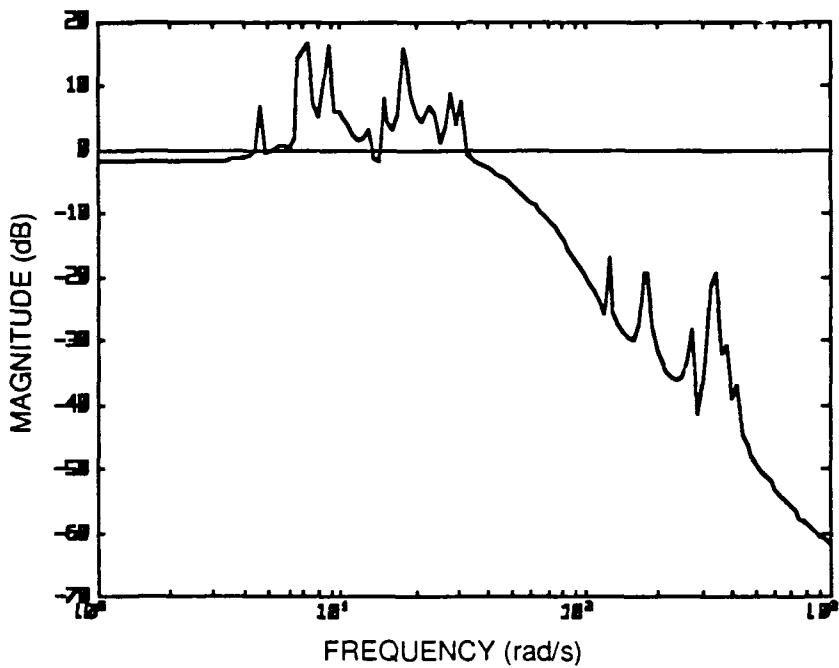
Figure 8.23 Closed-Loop Transfer from All Disturbances to All Errors (T_{22})
(5% More Stiff Open-Loop System).
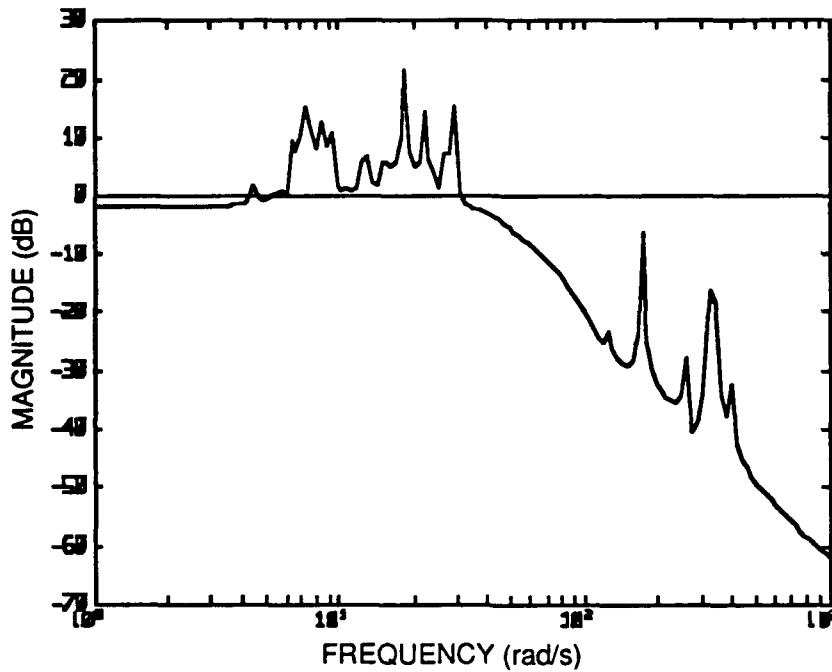
Figure 8.24 Closed-Loop Transfer from All Disturbances to All Errors (T_{22})
(5% Less Stiff Open-Loop System).

Since performance specifications are not met in the presence of two and one-half percent open-loop natural frequency parametric uncertainty, the closed-loop system does not possess robustness of performance to these types of structured parameter errors. This observation raises the question of whether or not the closed-loop system displays robustness of performance to the errors due to truncation of modes brought about by model reduction. To answer this question, consider Figure 8.25, which shows the closed-loop transfer from d to e maximum singular value frequency response for the "truth" model with no parametric uncertainty. As can be seen from the figure, the system does indeed possess robust performance for the errors due to model reduction.
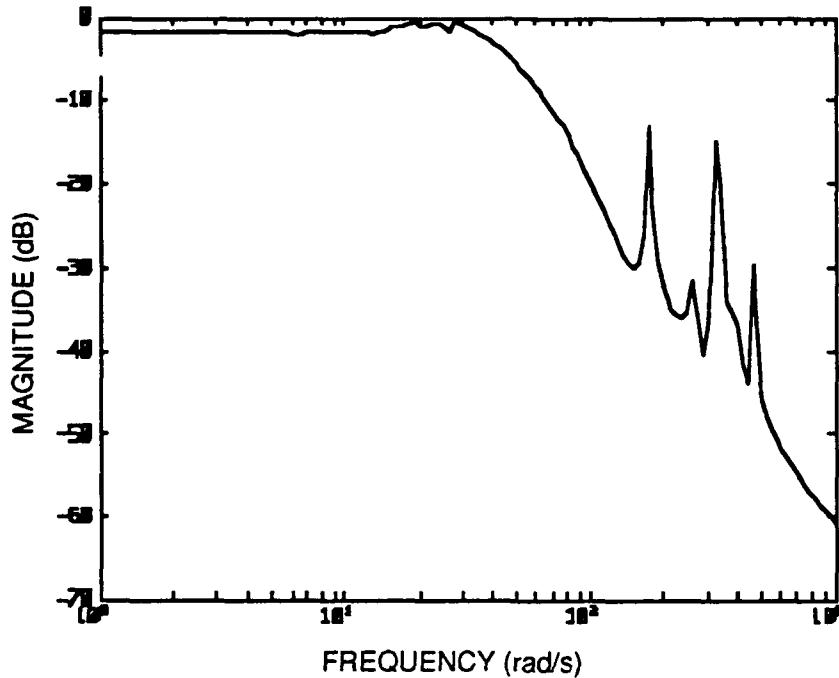
Figure 8.25 Closed-Loop Transfer from All Disturbances to All Errors(T_{22})
(108-State Truth Open-Loop System).

In this section, it has been shown that when a compensator is designed via H_∞ optimal control techniques, small levels of parametric uncertainty in open-loop system dynamics may lead to severe degradation in closed-loop system performance. This may be attributed to the common characteristic of all optimal control methodologies to attempt to "invert" the dynamics of the plant via selection of compensator poles and zeros, and it may therefore be concluded that precise knowledge of the locations of open-loop poles and zeros is crucial to the success of such design techniques. It has also been shown that the Small Gain Theorem may be applied to assess stability robustness of systems with open-loop pole parametric uncertainty, but the conservatism of the methodology should prevent one from definitely concluding that a particular closed-loop system will be unstable without independent verification. Finally, robustness of performance was demonstrated for the closed-loop system in the presence of errors due only to model reduction.

The coverage of design implementation/validation issues included in this thesis is now complete. A summary of the results presented and conclusions drawn in this thesis is therefore presented in Chapter 9, along with recommendations for further research.

169

CHAPTER 9

Conclusions

9.1 Summary

In this thesis, a comprehensive application of robust multivariable control system design techniques to a space-based laser beam expander segment phasing/jitter control example problem has been presented. In Chapter 1, an SBL system concept and relevant terminology was introduced, and a brief summary of the problem and its nature was presented. In Chapter 2, the details of the BEA segment phasing/jitter control problem were examined. A description of the physical system was given, a mathematical model was derived in an appropriate form for open-loop analysis and model reduction, and performance objectives were specified in terms of allowable RMS values (2-norms) of selected segment phasing and line-of-sight error performance variables. In Chapter 3, open-loop characteristics of the BEA model were studied. Nominal system stability, multivariable poles and transmission zeros, and singular value frequency responses were all addressed.

Chapter 4 introduced the topic of model reduction, which was performed on the high-dimension open-loop system model in order to obtain a less cumbersome model for control system design. Moore's Balance & Truncate algorithm, which allows the most uncontrollable/unobservable model states to be removed, was used to reduce the state dimension from 390 to 56, and characteristics of the reduced-order model were then presented.

Chapter 5 presented a flexible framework for robust control system design employing the Small Gain Theorem for stability robustness analysis, and either H_2 optimal, H_∞ optimal, or H_2/H_∞ loop-shaping techniques for compensator design. Satisfaction of stability robustness and performance conditions for all of these design techniques was then equated with ensuring unity bounds on the infinity-norms of two closed-loop transfer functions. Chapter 6 subsequently performed all modifications to the reduced-order system necessary in order to obtain a design plant model consistent with the control system design framework of Chapter 5. Norm-bounding of disturbance and error vectors, creation of a disturbance environment scenario, measurement noise requirements analysis, and representation of plant uncertainty due to model reduction were all addressed.

Chapter 7 provided a detailed comparison of performance characteristics and analysis of trade-offs existing between designs resulting from application of the various controller synthesis techniques of Chapter 5 to the design plant model of Chapter 6. Both unconstrained bandwidth H_2 and H_∞ designs were seen to meet nominal performance specifications, but not the stability robustness test of the Small Gain Theorem. H_2/H_∞ reduced bandwidth designs were able to meet stability robustness constraints, but resulted in unacceptable degradations in closed-loop performance. Robust H_2 loop-shaped error designs were able to meet performance specifications over certain limited frequency bands, but only H_∞ loop-shaped control designs were able to completely meet both stability robustness and nominal performance specifications. The 80th-order H_∞ loop-shaped control compensator was therefore adopted as the design of choice.

Chapter 8 surveyed several important design implementation/validation issues. A standard framework for digital implementation of continuous-time compensators was presented, along with the sampling and computation-time requirements engendered by adopting such a framework. The potentially excessive computation time required by high-order compensators motivated reduction of controller order, and the 73-state reduced-order compensator obtained was then validated via time-domain simulation and steady-state covariance analysis. Chapter 8 concluded with an examination of the effects of open-loop natural frequency parametric uncertainty, which were seen to mainly be severe degradation of closed-loop performance at higher frequencies. In contrast to the open-loop systems with natural frequency parametric uncertainty, however, the open-loop system with errors due only to model reduction was shown to possess robust performance.

9.2 Conclusions

Several conclusions may be drawn from the compensator synthesis procedure carried out in this thesis. Although little mention of it has been made to this point, of primary importance are the difficulties associated with compensator design for large-scale systems such as the SBL beam expander, and the resulting necessity of applying model reduction techniques. Due to the large sizes of the matrices involved in modeling the system, numerical problems were encountered early and often in attempts to use standard analysis and design codes, and computation times were excessive (3 hours for a single full-order system singular value response on a DecStation 3100). Model reduction was therefore employed to the greatest extent possible in all phases of the design procedure, and controller design could not likely have been accomplished without it.

The results presented in this thesis have shown that compensator design for large-scale systems using reduced-order approximations is indeed possible, and that optimal control techniques may be employed to design compensators for such systems that meet desired performance characteristics. Requirements analysis via H_∞ optimization was shown to be a useful tool in facilitating this procedure. Also, the utility (and conservatism) of the Small Gain Theorem in assessing stability robustness to truncated dynamics and parametric uncertainty was demonstrated. Finally, it was seen that although robustness of performance was not explicitly designed for, due to the relatively small significance of high frequency modes in the frequency response of the problem considered, performance robustness was incidentally obtained.

One of the most striking results presented in this thesis has to do with the superiority of performance exhibited by the loop-shaped designs, which employ frequency-dependent weights and scalings, as compared to the "brute-force" optimal solution methods which use the plant model as is. Although loop-shaping techniques require some skill and intuition to apply and result in additional compensator complexity, the additional degrees of freedom afforded by such techniques were shown to yield significantly better results than solution of the H_2/H_∞ Riccati equation using only the nominal system model, and the utility of the loop-shaping methodology was therefore demonstrated.

A final conclusion of importance was demonstrated in Section 8.5, and has to do with realistic expectations of compensator performance in a practical setting. It was shown in Section 8.5 that even small errors in knowledge of open-loop system poles can result in severe performance degradations of closed-loop systems incorporating compensators generated via optimal control methodologies. Therefore, although the singular value plots and linear simulations performed in this thesis validate the ability of the design to meet performance objectives, one should not expect such perfect performance in the real world.

9.3 Recommendations for Further Research

The main shortcoming of the design procedure carried out in this thesis is that, due to the need to limit model dimension, plant uncertainties were limited to the known error caused by truncation of generally high-frequency dynamics in the model reduction process, and later to open-loop natural frequency parametric uncertainty. In reality, other sources of plant uncertainty such as actuator errors and time delays exist, and a more realistic design approach should include some means of addressing these issues. Although the Small Gain Theorem approach presented in this thesis is applicable to such issues, it was not applied due to the complexity of the system already being considered. Additionally, the Small Gain Theorem is quite conservative, and therefore may not be the best tool to use in the final stages of design validation. Some type of robustness and performance analyses based on these considerations should be carried out, however, in order to obtain a more realistic picture of compensator performance. Doyle's structured singular value, otherwise known as μ [23], may provide one such analysis technique that does not possess the conservatism inherent in the Small Gain Theorem. For real parameter variations, however, (such as the stiffness uncertainties discussed in Chapter 8) the μ-analysis results may also prove to be quite conservative.

Another issue to be addressed is how to actually design for performance robustness, instead of simply attempting to verify it at the end of the design validation procedure. Similarly, methods of directly incorporating stability robustness constraints into the optimal control problem for large-scale systems would be useful. Again, methods based on the structured singular value may provide the best avenue for pursuit of these problems.

In Chapter 8, it was seen how compensator order increases computation time and may therefore drive the achievable sampling period in digital implementation of controllers.

Although model reduction techniques were used in this thesis to reduce the order of the selected compensator to 73 states, this is still a very high-order controller, and could pose significant implementation problems. Therefore, decentralized control techniques which break up the segment phasing and jitter control functions into several localized tasks, thereby reducing individual compensator order, should be investigated.

The final issue to be resolved, which was mentioned in Chapter 1, but has been somewhat glossed over since then, is that the segment phasing and jitter control functions are only two components of the overall beam control problem. The wavefront control problem, with all of its complexities and ramifications, remains to be addressed. The deformation of the primary mirror inherent in most wavefront control schemes envisioned would be sure to have some, possibly quite significant effects on the other aspects of the beam control problem considered in this thesis. This third and most difficult control function must therefore be addressed before it can be said that a truly satisfactory solution to the beam control problem has been obtained.

References

[1] Sanders, G., "Robust Multivariable Control Design for the Primary Mirror Segment Phasing of a Space Based Laser," Master's Thesis, MIT, 1986.

[2] Dowdle, J. and Negro, J., "Baseline Space-Based Laser Concepts for Integrated Control," CSDL Report Number CSDL-R-1878, the Charles Stark Draper Laboratory, June 1986.

[3] Athans, M., " Course Notes in Multivariable Control Systems", MIT, Spring 1990.

[4] Hardy, J., "Active Optics: A New Technology for the Control of Light," *Proc. IEEE*, Vol. 66, No. 6, pp. 4-15, June 1978.

[5] O'Meara, T., "Stability of an N-loop Ensemble-Reference Phase Control System," *J. Opt. Soc. Amer.*, Vol. 67, No. 3, pp. 315-318, March 1977.

[6] Flueckiger, K., Dowdle, J., and Henderson, T., "A Control System Design Methodology for Large-Scale Interconnected Systems," Proceedings of the 1990 American Control Conference, San Diego, CA, pp. 428-434.

[7] Maciejowski, J.M., *Multivariable Feedback Design*, Addison-Wesley, 1989.

[8] Born, M., and Wolf, E., *Principles of Optics*, Pergamon Press, 1980.

[9] Kwakernaak, H., and Sivan, R., *Linear Optimal Control Systems*, Wiley-Interscience, 1972.

[10] Desoer, C.A., *Notes for a Second Course on Linear Systems*, D.Van Nostrand Co., 1970.

[11] Laub, A., and Little, J., *Control System Toolbox User's Guide for use with Matlab,*, The Mathworks, 1986.

[12] Boyd, S., and Desoer, C.A., "Subharmonic Functions and Performance Bounds on Linear Time-Invariant Feedback Systems," UCB/ERL M84/51 Tech. Report, Univ. of California, Berkely, CA, June 1984.

[13] Freudenberg, J., and Looze, D., *Frequency Domain Properties of Scalar and Multivariable Feedback Systems*, Springer-Verlag, 1988.

[14] Kailath, T., *Linear Systems*, Prentice-Hall, 1980.

[15] Moore, B.C., "Principle Component Analysis in Linear Systems: Controllability, Observability and Model Reduction," *IEEE Trans. on Auto. Control*, Vol. AC-26, pp. 17-32, 1981.

[16] Glover, K.. "All Optimal Hankel-Norm Approximations of Linear Multivariable Systems and Their Error Bounds," *Int. J. of Control*, Vol. 39, No. 6, pp. 1115-1193.

[17] Safonov, M. and Chiang, R., "A Schur Method for Balanced Model Reduction," Proceedings 1988 *American Control Conference*, pp. 1036-40.

[18] Safonov, M. and Chiang, R., "Model Reduction for Robust Control," Proceedings 1988 *American Control Conference,* pp. 1685-90.

[19] Meyer, D., "A Fractional Approach to Model Reduction," Proceedings 1988 *American Control Conference*, pp. 1041-47.

[20] Doyle, J., Glover, K., Khargonekar, P., and Francis, B., "State-Space Solutions to Standard H_2 and H_∞ Control Problems," *IEEE Transactions on Automatic Control*, vol. AC-34, no. 8, pp. 831-847, 1989.

[21] Franklin, G., Powell, J., and Workman, M., *Digital Control of Dynamic Systems*, Addison-Wesley, 1990.

[22] Gelb, A., *Applied Optimal Estimation*, MIT Press, 1974.

[23] Doyle, J., "Structured Uncertainty in Control System Design," *Proceedings of the IEEE Conference on Decision and Control*, pp. 260-265, December 1985.